Ultrafast Nonlinear Spectroscopy of Red Fluorescent Proteins

by

Patrick Eugene Konold

B.S. University of Minnesota, 2008

A thesis submitted to the

Faculty of the Graduate School of the

University of Colorado in partial fulfillment

of the requirement for the degree of

Doctor of Philosophy

Department of Chemistry and Biochemistry

2015

This thesis entitled:

Ultrafast Nonlinear Spectroscopy of Red Fluorescent Proteins

written by Patrick Eugene Konold

has been approved for the Department of Chemistry and Biochemistry

_____

Ralph Jimenez

_____

Steven Cundiff

Date_____

The final copy of this thesis has been examined by the signatories, and we find that both the content and the form meet acceptable presentation standards of scholarly work in the above mentioned discipline

Konold, Patrick Eugene (Ph.D., Physical Chemistry, Department of Chemistry and Biochemistry)

Ultrafast Nonlinear Spectroscopy of Red Fluorescent Proteins

Thesis directed by Professor Ralph Jimenez

Red-emitting homologues (RFPs) of the native Green Fluorescent Protein (GFP) with emission wavelengths beyond 650 nm are desirable probes for *in vivo* imaging experiments. They offer the potential for deeper tissue penetration and lower background scatter given a cleaner spectral window. However, bioimaging applications are hindered by poor photophysics (*e.g.* low fluorescence quantum yield, high photobleaching), which limits experimental resolution and represents a significant obstacle towards utilization for low copy-number, long-duration imaging applications. In this thesis, a variety of femtosecond nonlinear electronic spectroscopies were employed jointly with site-directed mutagenesis to investigate the photophysical properties of RFPs. In one study, the molecular mechanism of red emission was pursued in two notable RFPs, mPlum and TagRFP675. Solvation dynamics observed with time-resolved transient grating spectroscopy were interpreted with the aid of molecular dynamics simulations to indicate that their red-emission is correlated with the ability of specific chromophore-sidechain hydrogen-bonding interactions to interconvert between direct and water-mediated states. In a second set of studies, two-dimensional double quantum coherence spectroscopy was used to probe the electronic transitions of mPlum. It was discovered that it displayed a response distinctly different from an organic dye in bulk solvent. Modeling indicate of these spectra indicate the spectral features may be attributed to the existence of multiple high-lying (n>1) excited states. The results

provide new insight into the electronic structure of these widely used fluorescent probes.

Dedication

I dedicate this thesis to my family and friends who inspired me to think big and realize my full potential no matter the odds

Acknowledgements

Several people were instrumental to both my personal and professional enrichment throughout this journey. I am very grateful to all I have encountered during my time at CU and in the greater Boulder area.

First, I must thank my advisor, Professor Ralph Jimenez, for helping me embrace the discipline of biophysics and convincing me that proteins are not all that scary. Orchestrating interdisciplinary research is no easy task and our success is a testament to his qualification as both a scientist and a mentor. Moreover, his high expectations have helped expedite my scientific development and acquire the problem-solving skills and confidence necessary to foster success in my looming professional career.

It's very safe to say I would not have pursued a graduate degree without inspiration from Professor Aaron Massari at the University of Minnesota. I appreciate his willingness to lend laboratory *carte blanche* to an inexperienced, yet relentlessly curious and ambitious, chemistry student. This opportunity laid the foundation for my current academic success and I am eternally thankful.

I must also recognize present and past members of the Jimenez group who were a great help over these years. Thanks to Jennifer Lubbeck for recruiting me to the group. Hairong Ma for keeping me busy through the first broken laser. Linda Schwall and Pia Friis for doing a whole lot of pipetting/incubating/centrifuging in the preparation of countless protein samples allowing me to focus on development

of spectroscopic experimentation, and also for introducing me to the basics of molecular biology. Kevin Dean for useful scientific discussions and being an outlet when things weren't going so smooth.

JILA is a wonderful environment to do scientific research and, in general, a great place to work. I especially recognize the support staff who I've solicited uninvited countless times over these past years. A special thanks is necessary to Hans Green, Todd Asnicar, and Kim Hagen (instrument shop), JR Raith and Jim McKown (computing), Terry Brown (electronics), and Brian Lynch (purchasing). Their eagerness to lend assistance (at almost any hour) demonstrates a true passion for their work and is a critical advantage of conducting research here at JILA.

Several scientific collaborators were instrumental in the realization of this project. Thanks to Cundiff group members Alan Bristow and Galan Moody for helping troubleshoot the sometimes-ornery JILA MONSTR. Prem Chapagain and Bernard Gerstman for carrying out MD simulations that greatly helped with the interpretation of our experimental results. KM group members Dan Adams and Matt Seaberg for assistance with our brief foray into adaptive pulse shaping.

Finally, I must acknowledge nonscientific friends and acquaintances that were instrumental in keeping my mind fresh throughout this effort and are perhaps most responsible my academic success to date. For the record guys, I do not operate a laser light show. I owe a large debt of gratitude to my friends Mike (and Jenna) Belaen and David Wambeke dating back to earlier times in Minneota. Our achievements are empirical proof that, with a proper mindset, anything is possible.

Sam, Tiff, and Alena Kasanicky for offering the epitome of friendship. Thank you to my golf companions. You know who you are, and you probably owe me money. Thanks to the entire Murphy's/Snugbutter soccer team for introducing me to a new game and giving me a chance to run around in the fresh air in between moments of scientific rigor.

Table of Contents

List of Tables

List of Figures

Figure

Chapter I

Introduction

1.1 Spectral properties of Fluorescent Proteins

Fluorescent proteins (FPs), originally derived from marine organisms, have revolutionized cellular imaging experiments and become an invaluable tool for molecular biology research[1]. Manipulation of the progenitor Green Fluorescent Protein (GFP) from the jellyfish *Aequorea victoria* have led to creation of monomeric variants with tunable excitation and emission and serve as noninvasive, genetically targetable fluorescent probes of subcellular function[2]. To better facilitate these advanced applications, next-generation FPs with enhanced photophysical properties are highly desirable and offer the opportunity to bolster a new class of nanoscopic imaging technologies. These improvements include far-red emitting variants with emission wavelengths beyond 650 nm, improved chromophore maturation, increased brightness, reduced photobleaching, and efficient photomodulatability to serve advanced applications of superresolution nanoscopy[3-6]. Such technology has effectively broken the diffraction limit barrier and has the potential to capture biological activity in real time with near molecular-limited precision[7]. Ultrafast spectroscopy has been utilized to explore the mechanisms of excited-state proton transfer in GFP[8]. However, no thorough investigation of red fluorescent protein (RFP) photophysics has been reported to date.

Development of RFPs has proceeded along two primary lineages. DsRed was isolated from the mushroom coral *Discosoma* and led to the creation of a series of

species with variable emission wavelengths spanning the visible spectral region known as the mFruits[9-11]. Another source of development was eqFP578, originally extracted from the sea anemone *Entacmaea quadricolor*, spawned the development of the monomeric derivatives TagRFP and mKate[12-13]. To date, the major strategy for RFP improvement has relied on directed evolution of these parent species typically guided by the standard methods of structural biology and protein engineering[14-15]. The recent invention of nanoscopic imaging applications has prompted the need for more versatile photoactivatible RFPs with high fluorescence quantum yield and photostability. Simultaneous optimization of these photophysical parameters would represent a transformative advancement in RFP development.

The structural architecture of a FP is an 11-stranded β-barrel as depicted in a rendering of the crystal structure in Figure 1.1. The fluorescent chromophore is embedded deeply within this framework and is presumed largely isolated from the surrounding solvent bath. Although, defects within the barrel arising throughout the development of monomer analogues of the native oligomeric species are suspected as entrance pathways for molecular oxygen that is thought to hinder their photostability[16].

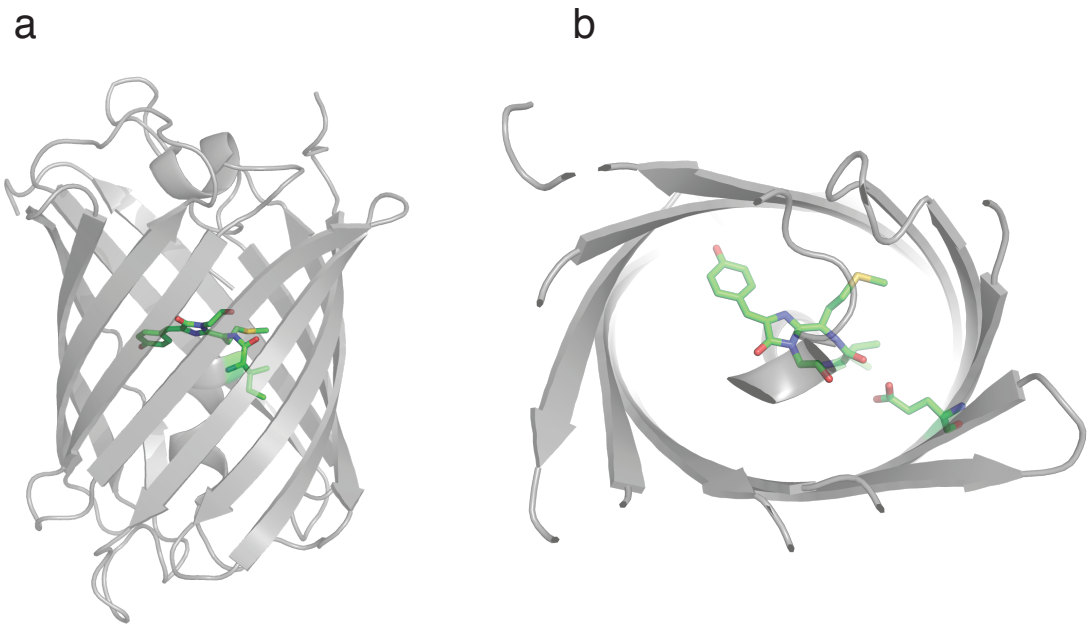

Figure 1.1. Representative monomeric fluorescent protein structure with (a) side and (b) top perspectives. The fluorescent chromophore (green) is embedded within an 11-stranded β-barrel.

The fluorescent *p*-hydroxybenzylideneimidazolinone chromophore is formed autocatalytically in the presence of molecular oxygen with residues 65-67 (S-W-G)[17]. The conjugated system of GFP spans two ring moieties, phenoxy and imidazolinone as illustrated in Figure 1.2. Upon electronic excitation, electron density shifts from the phenoxy ring towards the imidazolinone[18]. A common strategy in the development of red-emitting species involves extending the conjugated network by chemically integrating neighboring sidechains through post-translational modification. A classic example of this occurs in the RFP DsRed, where an N-acylimine forms autocatalytically adjacent to the imidazolinone ring and accounts for its red-shift excitation and emission relative to GFP[19]. The "DsRed-like" chromophore and subsequent variants have provided the most fruitful template for RFP development to date.

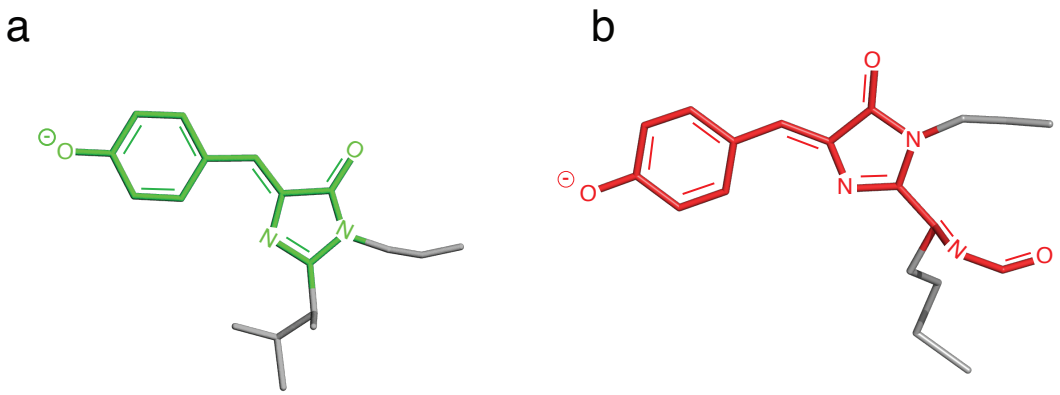

Figure 1.2. Chemical structure of the chromophore from the (a) GFP and (b) DsRed fluorescent proteins. The conjugated system is highlighted in each case.

The rich photophysics of GFP has attracted much attention in the past decade. It was initially discovered that the 4'- hydroxybenzylidene-2,3-dimethyl-imidazolinone (HDBI) chromophore shows remarkably different spectral properties in solution versus embedded within the native protective β-barrel structure. Most notably, the 1000-fold higher fluorescence efficiency (QY=0.8, lifetime=3.3 ns) in GFP versus in solution suggests that the surrounding protein matrix must play a pivotal role in preventing nonradiative deactivation of the excited chromophore[20-21]. GFP contains two absorption bands at 398 and 478 nm and a single emission peak at 510 nm[17]. The two absorption peaks are attributed to the neutral and anionic protonation states of the chromophore. Time-resolved fluorescence experiments by Chattoraj and coworkers first implicated Excited State Proton Transfer (ESPT) as the underlying cause of GFPs unique emission[8]. The precise structural fluctuations mediating these transfer events has been the subject of several time-resolved

optical and vibrational studies and has been thoroughly reviewed[22]. These investigations collectively point towards ESPT occurring through an intricate hydrogen bond network involving S205, E222, and embedded water molecules. Recently, Mathies and coworkers identified a key wagging motion responsible for modulation of ESPT in the neutral chromophore[23]. Similar ESPT pathways have been uncovered in other FPs[24-25]. It is speculated that these unique spectral properties are owed to preorganized chromophore-bath interactions with the surrounding protein environment.

More complex phototransformations occur in several other FP systems including on/off photoswitching, photoactivation, and photoconversion[25-27]. This occurs in GFP following prolonged excitation at 400 nm where gradual accumulation of a photoproduct with 80 nm redshifted absorption is thought due to irreversible oxidation of CO_2 from adjacent E222[28]. Similar photoactivity is observed in other proteins. For instance, rhodopsin and Photoactive Yellow Protein (PYP) are known to undergo photoinduced isomerization and ultrafast spectroscopy has been used extensively to unravel their respective photocycles[29-32]. Perhaps, the most widely studied photoswitchable FP is Dronpa, derived from the coral *Pectiniidae*, which exhibits distinct cis and trans conformations, in the light and dark states identified through structural characterization[33-36]. It was speculated that Dronpa underwent ESPT similar to GFP upon its discovery[36]. Optical pump-vibrational probe experiments by Warren *et al*. indicated a 9 ps isomerization time constant and upon vibrational analysis, imply proton transfer is thermally driven in the ground state. Moreover, they identify a weakening hydrogen bond between R66

and the chromophore carbonyl that may initiate the ultimate structural rearrangements leading to photoisomerization[37]. However, a broader characterization of these dynamics is unclear. Another study involving Dronpa and single point mutants displayed unique viscosity dependent photochromism not previously observed in FPs[38]. They hypothesized that a mechanical coupling from the protein exterior regulates flexibility near the buried chromophore. It also highlights the role of environmental dynamics in the apparent tradeoff between fluorescence quantum yield and photoswitchability[39]. The advent of superresolution nanoscopic imaging methods such as photoactivated localization microscopy (PALM) and stochastic reconstruction microscopy (STORM) has motivated the need for more robust red-emitting photoactivatible FPs[4, 7, 40-41]. Photoactivatible analogues of mCherry and TagRFP675 have been devised to advance the utility of these powerful techniques[42-43].

Alternatively, specific interactions between the chromophore and local sidechains are thought to influence FP spectral properties. mPlum was developed through iterative hypersomatic mutation of mRFP, from the progenitor DsRed, to achieve a Stokes shift of 59 nm and represents one of the farthest red emitting monomeric FPs discovered to date[44]. A fluorescence upconversion study by Abbyad *et al.* identified a significant dynamic Stokes shift in mPlum that was distinct from mRaspberry and mRFP which demonstrated negligible solvation over a nanosecond time window[45]. They, along with a later crystallographic study, attributed the extended Stokes shift of mPlum to a specific direct hydrogen bond interaction between the E16 sidechain and N-acylimine oxygen of I65[46]. It is thought that these

interactions facilitate stabilization of the excited state by a combination of indirect modulation of hydrogen bonds at other positions across the chromophore as well as acting to restrict its motion to maintain coplanarity throughout multiple rings composing the conjugated system. Hydrogen bond networks have been identified in the crystal structures of other RFPs including mNeptune, mRouge, eqFP650, eqFP670, mCherry, TagRFP675, and mRojoA and may play a critical role in tuning the emission (absorption) wavelength through excited (ground) state stabilization[11-12, 47-50]. Moreover, nonradiative deactivation of the excited population resulting from enhanced flexibility about the extended conjugated system might explain their comparably low quantum yields relative to bluer-emitting species.

1.2 Nonlinear Femtosecond Spectroscopy

Evolution of Time-Resolved Experimentation

This section will briefly survey the evolution of time-resolved methods as they developed coincident with advances in detection and light source technology. The seminal accounts of time-resolved spectroscopy centered on nonreactive solvation dynamics of simple organic dyes in solution. Pioneering works of Bakshiev and Ware utilized fluorescence upconversion spectroscopy with streak cameras to decipher nanosecond responses of solvated dyes[51-53]. This work spawned an entire field of research into addressing the molecular movements about an excited optical probe[54].

These methods were also applied to biological systems where it was discovered that proteins demonstrated a response unique from a probe in bulk

solvent[55-57]. Early experiments revealed relaxation across a broader time range compared to dyes in simple solvents[58]. The protein response was also found to be highly nonexponential, characteristic of inherent heterogeneity that was attributed to natural multiplicity of conformational substates. These observations are consistent with the energy landscape picture, the predominant physical model that connects protein dynamics to their function[59-60].

The stage was set to connect these phenomena with protein function itself. However, with particular regard to a complex energy landscape, probing specific aspects of required novel strategies to improve experimental clarity. Methods including photoinitation *via* flash photolysis, fluorescence energy transfer or excited state quenching to measure spatial proximity, excited state proton transfer, and incorporation of exogenous probes were used to better visualize a particular reaction[61-64]. These preliminary investigations spawned investigation of more complex ideas such as conformational heterogeneity, allostery, and further mitigating the effect of ensemble averaging, which motivated the development of more sophisticated experimentation[65-67].

Modern biophysical spectroscopic applications have revealed a broad range of photochemical reactions. A few examples include understanding the photoisomerization in the photoreceptor rhodopsin that constitute the primary steps in human vision, exciton transfer dynamics in photosynthetic light-harvesting complexes, protein folding dynamics, DNA damage repair mechanisms, and redox chemistry of several enzymes[32, 68-73]. Other efforts have focused on more

fundamental facets governing protein motions in canonical systems (*e.g.* CO-ligand dissociation dynamics in myoglobin) to help develop a unified model of protein structure-function relationships[74-75]. However, while the field has greatly evolved since the infancy of spectroscopic analysis, modern information-rich techniques offer insight into a host of new biophysical dilemmas including investigation of correlated motions and long-range allosteric interactions on timescales previously inaccessible to earlier methods.

The invention of ultrashort light sources has accelerated the evolution of time-resolved spectroscopy[76-77]. In particular, modern femtosecond lasers produce pulse durations on the order of molecular vibrations and enable investigation of the fastest motions in condensed phase systems. Such methodology is well suited to unravel a wide spectrum of protein motions by depositing energy instantaneously and in discrete quantities leaving the excited probe out of equilibrium with the surrounding environment. The time dependent response an excited probe is most generally represented as a time correlation function of the electronic energy gap

$$C(t) \propto \left\langle \delta\omega_{10}(t)\delta\omega_{10}(0) \right\rangle \tag{1.1}$$

where $\delta\omega_{10}$ is the energy gap of a ground to first excited-state electronic transition. Monitoring this quantity over timescales characteristic of molecular relaxation and subsequent Fourier transformation yields a vibrational spectral density ($\rho(\omega)$) encompassing the spectrum of motions participating in system-bath relaxation[78]

$$\lambda = \frac{1}{\pi}\int_0^\infty \omega\rho(\omega)d\omega \tag{1.2}$$

where λ is the total nuclear reorganization energy. This is perhaps the most critical variable accessed by transient spectroscopic experimentation. Femtosecond spectroscopic techniques have evolved to encompass spectral regions from the mid-infrared to x-rays[79-83]. These experiments yield system-bath coupling over a wide time range with varying sensitivity. Their resolving power is owed to both experimental sophistication and the nature of the spectroscopic probe. The practical distinctions between femtosecond and conventional spectroscopy can be viewed from the perspective of this sensitivity, which varies widely in both time and length scales. A discussion of the theoretical underpinnings of nonlinear spectroscopy will now follow.

Response Function Formalism

As referenced by name, nonlinear spectroscopic methods exploit light-matter interactions beyond a linear response. Light-matter interactions are often characterized by an induced polarization, expressed below as a Taylor Series expansion with respect to the electric field[78].

$$\overline{P}(t) = P^{(0)} + P^{(1)} + P^{(2)} + P^{(3)} + \cdots \tag{1.3}$$

or

$$P = \chi^{(1)}E + \chi^{(2)}EE + \chi^{(3)}EEE + \ldots \tag{1.4}$$

Here, $\chi^{(n)}$ represents the nth order nonlinear susceptibility tensor, E is the incident electric field, and P is the induced polarization. The susceptibility tensor arises from symmetry considerations within the nonlinear media and serves as a useful selection rule for practical application of various nonlinear techniques. For example,

$\chi^{(2)}$ processes such as Second Harmonic Generation (SHG) and Sum Frequency Generation (SFG) are possible only in noncentrosymmetric media lacking an inversion center[84]. The experiments conducted in this project utilize femtosecond light sources with sufficient peak intensities to access the third order response of various biological probes.

Time-dependent quantum mechanics is required to adequately describe light-matter interactions and their associated dynamic evolution in the condensed phase. This characterization relies on the density matrix operator, ρ, used to treat systems of statistically mixed states[85].

$$\rho_{nm} = \langle n|\rho|n\rangle = \overline{|a_n|^2} \tag{1.5}$$

$$\rho_{nm} = \langle n|\rho|m\rangle = \overline{a_n a_m^*} \tag{1.6}$$

Diagonal terms represent population states, while off-diagonal terms are coherence between two states, leading to population relaxation and dephasing (decoherence) respectively. The time evolution of these Eigenstates follows from the quantum Liouville equation

$$\frac{\partial \rho}{\partial t} = \frac{-i}{\hbar}[H, \rho] \tag{1.7}$$

$$H = H_0 + V(t) \tag{1.8}$$

Here, H is the total molecular Hamiltonian, H_0 is the unperturbed Hamiltonian and $V(t)$ is the perturbation describing the light-matter interaction. If considering only electric-dipole transitions the final term becomes

$$V(t) = -\mu \cdot \vec{E} \tag{1.9}$$

where μ is the electronic dipole moment and *E* is the incident electric field. Nonlinear polarizations are most easily treated as higher order perturbations of the density matrix. The time dependent perturbed density matrix can be evaluated by inserting into Equation 1.7

$$\rho^{(n)}(t) = \left(-\frac{i}{\hbar}\right)^2 \int_{-\infty}^{t} dt_n \int_{-\infty}^{t} dt_{n-1} \cdots \int_{-\infty}^{t} dt_t \left[V(t_n), \left[V(t_{n-1}), \left[\ldots, \left[V(t_1), \rho_{eq}\right]\ldots\right]\right]\right] \tag{1.10}$$

The total nonlinear polarization is generally expressed as

$$P^{(n)}(t) = \left\langle \mu \rho^{(n)}(t) \right\rangle \tag{1.11}$$

After organizing terms, this leads to a solution for the polarization separated among several unique response functions.

$$P^{(n)}(t) = \int_0^\infty d\tau_n \cdots \int_0^\infty d\tau_1 R^{(n)}(\tau_1, \tau_2, \ldots \tau_n) E_1(t - \tau_n - \cdots - \tau_1) \cdots E_n(t - \tau_n) \tag{1.12}$$

Here, $R^{(n)}$ is the n^{th} order nonlinear response function

$$\begin{aligned} R^{(n)}(\tau_1, \tau_2, \ldots \tau_n) &= \left(\frac{i}{\hbar}\right)^n \theta(\tau_1)\theta(\tau_2)\ldots\theta(\tau_n) \times \\ &Tr\left\{\left[\left[\ldots\left[\mu(\tau_n + \tau_{n-1} + \ldots\tau_1), \mu(\tau_{n-1} + \tau_n + \ldots\tau_1)\right], \ldots\right]\mu(0)\right]\rho_{eq}\right\} \end{aligned} \tag{1.13}$$

A total of 2^n terms are possible stemming from multiple interactions with the *bra* and *ket* side of the density matrix. However, after accounting for all possible interactions, a total of 48 terms exist for a two-level third order response.

A few notable experimental tools are utilized to simplify the number of unique pathways. First, phase-matching enables spatial isolation of specific

nonlinear responses. Early applications of NMR spectroscopy were carried out in a collinear geometry, which necessitated separation of excitation pulses with the emitted signal field. Conventional nonlinear optical experiments typically utilize a noncollinear excitation geometry[86]. The most commonly used is the BOXCARs geometry, stemming from Coherent Antistokes Raman Spectroscopy (CARS), where the excitation beams are incident on the corners of a square. This configuration enables spatial isolation of the emitted third order polarization and ideal phase-matching efficiency considering the symmetric arrangement of the beams. Second, reordering the relative arrival time of excitation pulses at the sample position within the BOXCARs geometry enables selective sampling of different nonlinear responses without physical realignment of excitation beams. Finally, diagrammatic methods are a useful tool for organizing and interpreting nonlinear response functions[78]. In particular, double-sided Feynman diagrams describe transitions within the density matrix with a specific time ordering and phase-matching. A brief primer of this method is given in Figure 1.3.

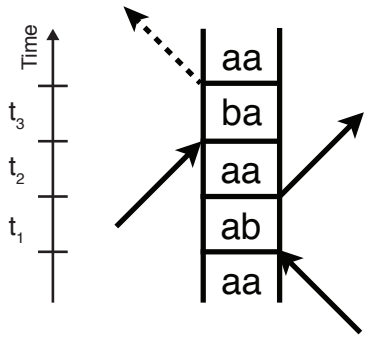

Anatomy of a Feynman Diagram

•Vertical lines represent time evolutation of bra and ket sides of density matrix

•Time increases from bottom up

•Light-matter interactions are indicated by solid arrows

•Inward and outward-going arrows represent photon absorption and emission respectively

•Emitted signal is signified by a dashed arrow

•The system must begin and end in a population state

Figure 1.3. Guidelines for interpreting double-sided Feynman diagrams used to described nonlinear light-matter interactions.

The diagrams in Figure 1.4 describe the most commonly encountered pathways for electronic spectroscopy of three-level molecular systems.

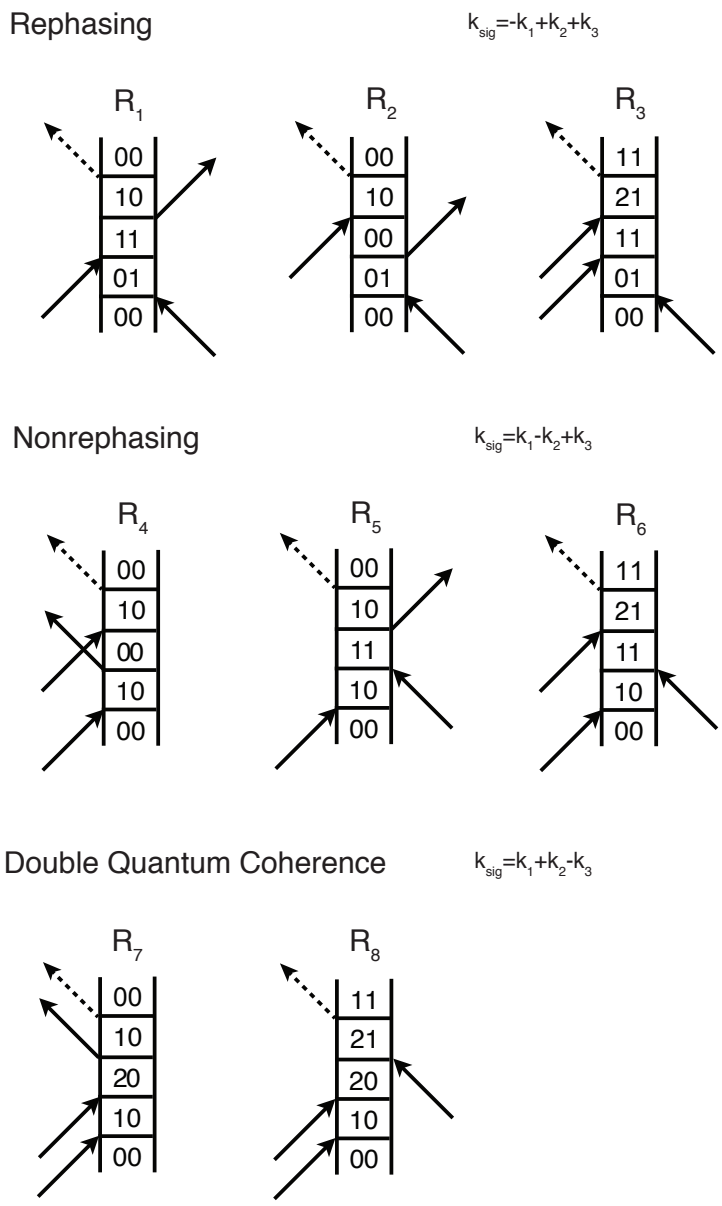

Figure 1.4. Third order nonlinear optical responses for a three-level system. These can be categorized in terms of phase-matching conditions as rephasing, nonrephasing, or double quantum coherence contributions.

Bath Models

The countless permutations of sidechain flexibility, conformational heterogeneity, hydrogen bonding, and innumerable tertiary interactions in biological systems form the complex energetic landscape introduced above.

Unraveling these seemingly innumerable variables represents a central challenge for deciphering biophysical functional mechanisms. In the context of electronic spectroscopy, it explains the typically congested absorption spectra of biophysical probes that complicate physical interpretation. Electronic transition frequencies are modulated by coupling with nuclear degrees of freedom of the chromophore itself and that of the surrounding bath. These interactions are too complex for a complete analytical treatment and thus, require some degree of approximation to accurately predict experimental data. This section will describe the general foundations concerning system-bath interactions and discuss the prominent bath models utilized in theoretical treatment of electronic absorption lineshapes.

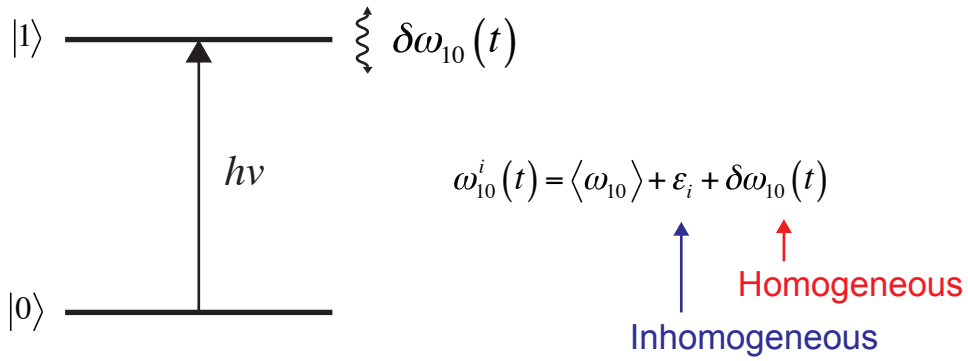

Figure 1.5. The time evolution of an electronic transition frequency in the condensed phase can be dissected into separate homogeneous and inhomogeneous components.

The electronic absorption lineshape ($\sigma(\omega)$) can be generally expressed as a Fourier transform of the complex lineshape function g(t) containing all system-bath interaction information.

$$\sigma(\omega) = \frac{1}{2\pi}\int_{-\infty}^{\infty} dt e^{-i\omega t} e^{i\omega_{10}t - g(t)} \tag{1.14}$$

In its simplest form, the lineshape function is treated as linear damping term (Γ), known as the Bloch limit, and is characterized by a Lorentzian absorption lineshape[87]. This model assumes an equal (homogeneous) treatment for all members of the ensemble. In the opposite limit, g(t) is assumed to be a quadratic term (Δ^2) and leads to a Gaussian absorption lineshape. This model is frequently used to represent cases of large inhomogeneous broadening where the system exists of independent absorbers having a statistically normal distribution of transition frequencies within the Central Limit Theorem.

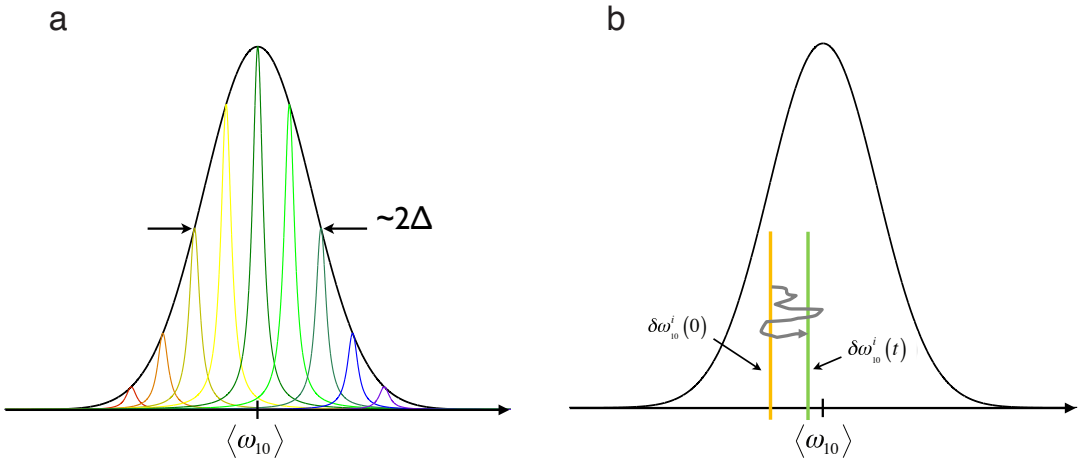

Figure 1.6. (a) Inhomogeneous Gaussian absorption lineshape with underlying Lorentzian subensembles. (b) Time dependent transition frequency of a single excited oscillator.

A stochastic model, originally introduced by Kubo *et al.*, incorporates continuous interpolation between fast and slow components of bath fluctuation[88]. This handling was sufficient for description of resonance Raman and fluorescence processes, but is inadequate in cases involving large changes in electron density or

solvent/solute reorganization along a particular reaction coordinate[89]. A stochastic bath is adequate for probing general aspects of absorption features, however, a more complete model is necessary to obtain accurate absorptive lineshapes and their transient behavior as is typically sought by nonlinear spectroscopy. The current standard theoretical treatment is the multimode Brownian oscillator[78]. This model assumes the solute is subject to a quantum mechanical bath subject to Langevin-like friction. It converges to the stochastic results within classical limits, but with proper inclusion of Stokes shift and non-Markovian dynamics. Its characteristic lineshape function at high temperature is generalized as

$$g(t) = \sum_j \left[i\lambda_j \int_0^t dt_1 M_j(t_1) + \left\langle \Delta_j^2 \right\rangle \int_0^t dt_1 \int_0^{t_1} dt_2 M_j(t_2) \right] + \frac{\Delta_{in}^2 t^2}{2} \qquad (1.15)$$

where the total reorganization energy, λ_j, is partitioned among all participating solvent modes with weighting Δ_j.

1.3 Survey of Nonlinear Optical Methods

Regardless of the precise bath treatment, electronic lineshapes of biomolecules are often broad and featureless enhancing the difficulty of interpreting underlying structure or dynamics. Extracting this information is facilitated by the experiments described in this section. A survey of experimental methods employed in this thesis is given below. Precise data collection procedures will be presented in a later chapter.

Transient Absorption Spectroscopy

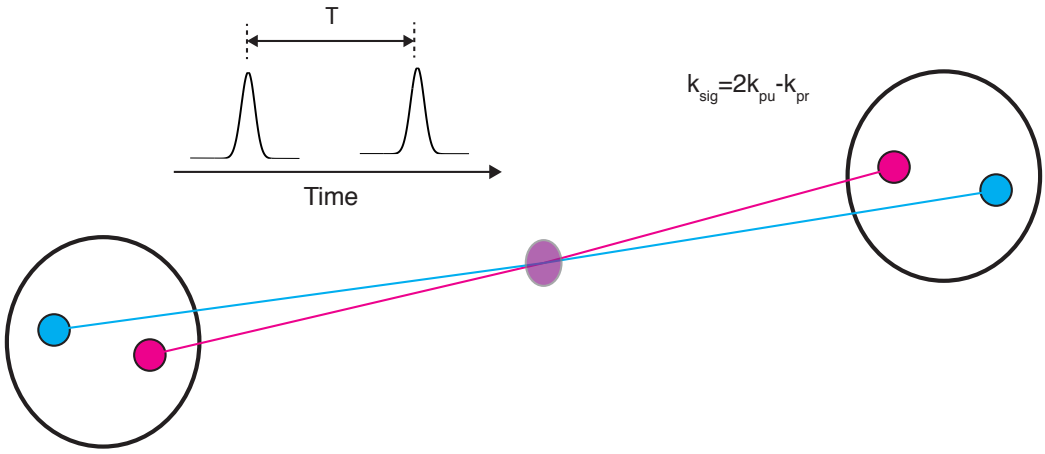

Figure 1.7. Beam geometry and pulse sequence for a transient absorption spectroscopy experiment.

Transient absorption (TA) spectroscopy is conducted by measuring differential intensity of the probe field with and without exposure of a preceding pump field. It is treated as a 3rd order interaction with a $\mathbf{2k_{pu}\text{-}k_{pr}}$ phase matching condition. The detected signal intensity can be expressed as[90]

$$\Delta I(T) = \frac{nc}{4\pi}\left\{\left|E_{pr}' E_{sig}(T)\right|^2 - \left|E_{pr}'\right|^2\right\} \tag{1.16}$$

where n is the refractive index, c is the speed of light, and E_{pr} and E_{sig} are the probe and nonlinear signal fields respectively. *In situ* removal of E_{pr} by chopping the pump beam leaves only the cross term and following substitution for E_{sig} yields

$$\Delta I(T) = 2\omega_{sig} l \,\mathrm{Im}\left[E_{pr}' P^{(3)}(T)\right] \tag{1.17}$$

where $\mathrm{Im}(P^{(3)})$ represents the imaginary (absorptive) part of the 3rd order polarization. Given this relationship, the TA response is sensitive to both ground and excited state dynamics. Measurements are commonly spectrally-resolved to

provide simultaneous dynamic information across a wide spectral window. Since TA is not inherently background-free, sophisticated detection schemes such as lock-in amplification have helped to improve experimental sensitivity.

Transient Grating Spectroscopy

A three-pulse analogue of the transient absorption technique is transient grating (TG) spectroscopy. The temporal overlap of $\mathbf{k_1}$ and $\mathbf{k_2}$ (τ=0) imprints a spatial interference on the irradiated sample volume leading to a periodic area of high and low intensity. This is commonly described as a population grating and its time evolution is sensitive to excited state lifetime, spectral diffusion, and solvation dynamics[91-92]. The TG signal contains both ground and excited state components stemming described by the response functions below. Like TA spectroscopy, spectrally-resolved detection enables quantification of solvation dynamics. However, TG spectroscopy is less-frequently used likely due to the need for a third excitation beam.

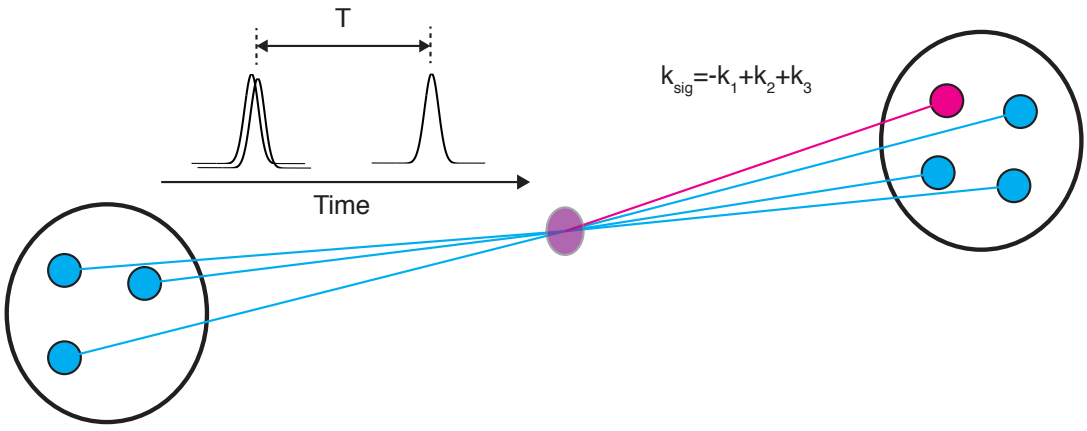

Figure 1.8. Beam geometry and pulse sequence for a typical transient grating spectroscopy experiment.

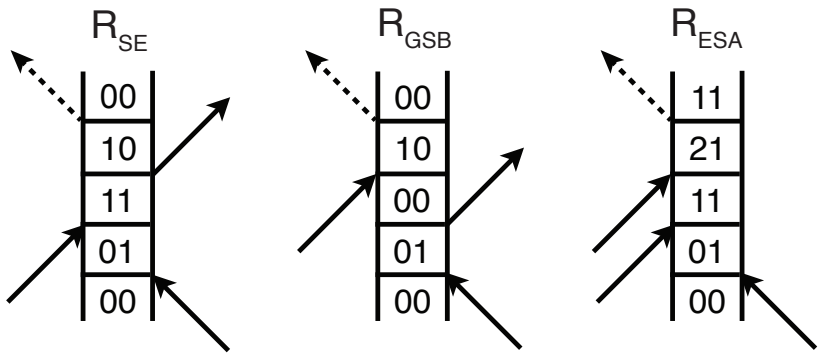

Figure 1.9. Third order light-matter interactions for a transient grating experiment of a three-level system.

Photon Echo Spectroscopy

As indicated above, the ensemble average is only partially subverted with femtosecond time resolution. The highly coupled structural arrangement of biomolecules yields complex absorption spectra with several overlapping features. Moreover, these features may be highly separable in the time domain rendering them indecipherable by conventional methods. These divisions in time are known as the homogeneous (fast) and inhomogeneous (slow) limits and can be described by their respective linewidths as illustrated in Figure 1.6.

Photon echo techniques exploit the inherent inhomogeneity of chemical resonances in the condensed phase and their molecular dephasing and rephasing processes. These methods were first applied to NMR spectroscopy following the discovery of spin echoes and are the subject of several extensive reviews[93]. NMR correlation spectroscopy is used extensively in the pursuit of protein structure and measurement of slow (μs-ms) dynamics[94-95]. Modern ultrafast lasers have led to analogues applied at infrared, visible, ultraviolet wavelengths[96-98]. These

experiments enable a similar examination of buried vibrational and electronic probes in biological systems, albeit at different time and length scales.

Photon echo spectroscopy relies on the spontaneous collective rephasing of independent dipoles[99]. This phenomenon is considered the optical analogue of a spin echo famously introduced by Hahn[93, 100]. In a molecular context, optical photon echoes represent the collective dephasing and subsequent rephasing of independent dipoles. In a condensed phase system, the dephasing/rephasing process is driven by coherent electronic excitation with an ultrashort light source combined with the intrinsic heterogeneity of transition frequencies as described above.

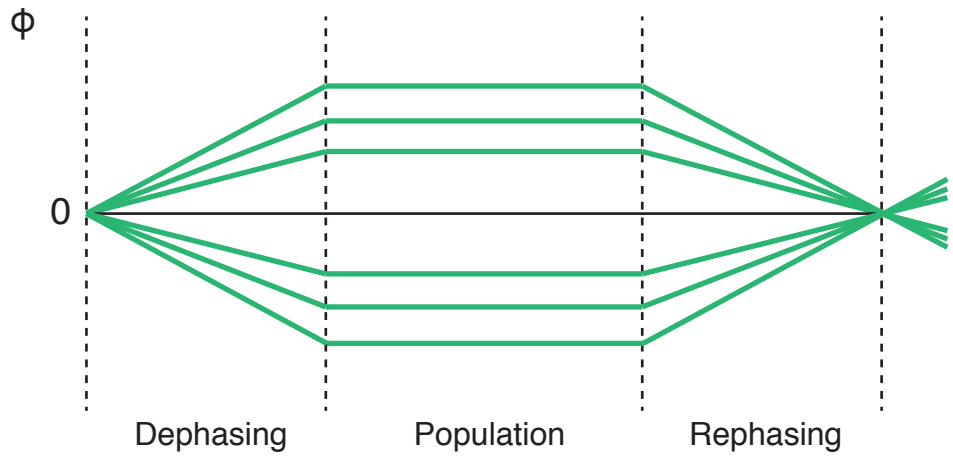

Figure 1.10. Evolution of the collective phase of the excited volume throughout a photon echo spectroscopy experiment.

The evolution of the collective phase upon coherent excitation of the excited volume is illustrated in Figure 1.10 and can be expressed as

$$\phi_i(t) \propto e^{i\omega_{10}^i t} \tag{1.18}$$

Here, the extent of sample dephasing or rephasing is modulated by intrinsic heterogeneity together with spectral diffusion occurring throughout the population time interval[100]. As such, dynamic information is preserved over a time interval spanning femtoseconds to several seconds unobscured by sample heterogeneity. This criterion renders photon echo spectroscopy intrinsically more powerful than the TA and TG methods described above.

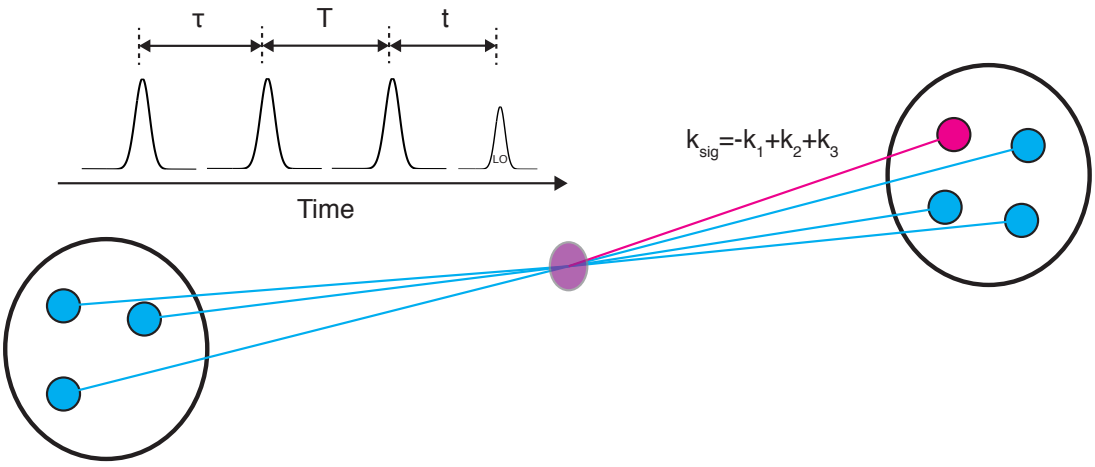

Figure 1.11. Beam geometry and pulse sequence for a heterodyne-detected stimulated photon echo spectroscopy experiment.

Figure 1.11 illustrates the BOXCARs beam geometry and pulse sequence used to generate a photon echo signal. Scanning through the τ dimension yields an approximate Gaussian distribution of signal intensity and its peak position in time is known as the "peak shift". This value plotted over a series of popuation times is proportional to the energy gap time correlation function and forms the basis of Three Pulse Photon Echo Peak Shift (3PEPS) spectroscopy. Moreover, asymptotic peak shift values also relate to the homogeneous (Γ) and inhomogeneous (Δ_{in})

linewidths expressed below in the limit of a two level system coupled to a harmonic bath with impulsive excitation[101].

$$\tau^{*}\left(T=0\right)\approx\left(\Gamma\pi\right)^{-1} \tag{1.19}$$

$$\tau^{*}\left(T\rightarrow\infty\right)\approx\Delta_{in}^{2}\left(\Gamma+\Delta_{in}^{2}\right)^{-1} \tag{1.20}$$

Multidimensional Spectroscopy

Photon echo phenomena can also be extended with a second frequency dimension where a resonance is spread across multiple axes. This treatment yields a transient correlation map of excitation and emission frequencies about a fixed population time and captures spectral diffusion, coherent dynamics, and energy transfer events within the ensemble. Generally known as multidimensional spectroscopy, this strategy has been applied to nuclear spin, vibrational and electronic transitions and is especially valuable in congested spectral regions typical of condensed phase systems[102-105]. However, the execution of proper spectral interferometry complicates multidimensional techniques. This becomes exceedingly challenging when fluctuations of the surrounding environment cause appreciable phase drifts at optical frequencies. Several strategies involving both passive and active phase stabilization have been proposed[106-109].

A general description of typical multidimensional spectra reveals its resolving power. First, Fourier transformation with respect to the τ and t time delays yields a two-dimensional frequency plot correlating excitation (initial) and emission (final) frequencies of a given oscillator[110-111]. Next, data are collected for a series of population times enabling investigation of transient spectral dynamics.

The figure below illustrates expected spectral features for a condensed phase response. Elongation along the diagonal at early T indicates non-Markovian behavior consistent with an inhomogeneously broadened transition[112]. While at long population time, the spectrum appears more symmetric as the system eventually samples its entire frequency space.

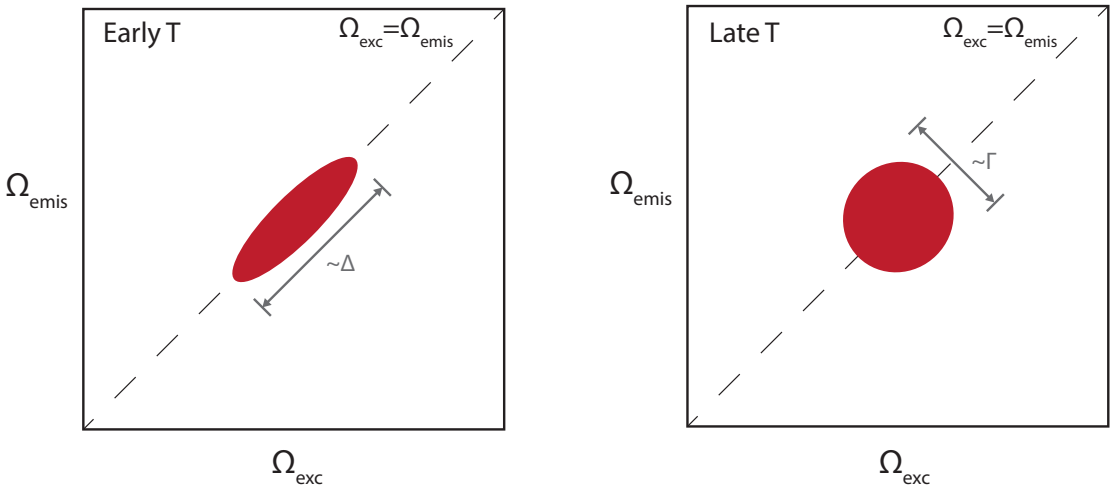

Figure 1.12. Expected two-dimensional spectral evolution of a two-level electronic system in the condensed phase. (a) Inhomogeneous broadening is manifest at early population time as elongation along the diagonal. (b) A symmetric peak is predicted at population times beyond the characteristic bath correlation time.

The case of population exchange is presented in Figure 1.13. At early population time, two peaks on the diagonal appear representing contributions from either state with unique transition energies. At later population time, cross peaks above and below the diagonal appear representing population transfer from the high-to-low and low-to-high energy states respectively. This situation is relevant for systems having closely spaced electronic modes such as exciton migration in

photosynthetic light harvesting complexes and isomerization events in biological systems[69, 113].

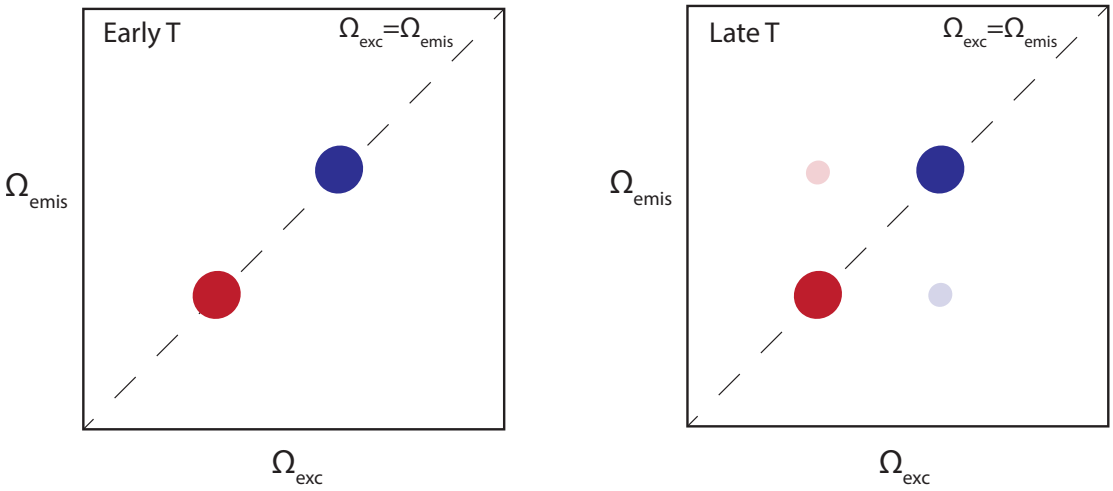

Figure 1.13. Expected two-dimensional spectral evolution for the case of electronic population transfer. (a) Two peaks fall along the diagonal at early times representing the independent transitions of each mode. (b) Cross peaks appear at later population times that signify population transfer between the low and high energy modes.

1.4 Thesis Objectives

The above accounts lay the foundation for investigation of RFP photophysical properties with femtosecond nonlinear spectroscopy. Previous exploration of these phenomena has been largely restricted to the standard methods of structural biology, which are incapable of resolving the complete range of molecular motions thought responsible for their complex behavior. Time-resolved electronic spectroscopy is uniquely suited to quantify the timescales of local chromophore-sidechain interactions. However, few previous accounts have addressed the dynamic behavior of RFPs including the molecular origin of their red emission. This

thesis aims to make these connections and help establish nonlinear femtosecond spectroscopy as a versatile tool for biophysical research. Specific objectives include investigating the hydrogen bond network in mPlum, one of the farthest known red-emitting RFPs. Transient grating spectroscopy is used to probe specific chromophore-sidechain interactions thought responsible for its extended Stokes shift. These results, corroborated with MD simulations, reveal hydrogen bond interconversion unique to the reddest-emitting members among a panel of strategic point mutants. The principles acquired in this study were next applied to investigate a similar hydrogen bond network in TagRFP675, the farthest red-emitting RFP discovered to date. Finally, multidimensional spectroscopy was employed to characterize the excited state electronic structure of mPlum. This information is potentially useful for understanding the dark state conversion processes that hinder full utilization of RFPs in advanced imaging applications.

Chapter II

Experimental Methods

2.1 Description of Light Source

The physical interpretations of this thesis were derived from measurement of molecular dynamics extracted from nonlinear spectroscopic experimentation. From a macroscopic perspective, these dynamics are conveniently treated as a time correlation function of the electronic energy gap-a common model to describe a third-order response[78]. To facilitate these measurements, a light source capable of generating femtosecond laser pulses resonant with an electronic transition of interest with sufficient bandwidth and intensity is required. The sections that follow describe hardware and device development to facilitate this experimentation. First, the light source used to carry out spectroscopic experimentation will be described. Next, aspects of pulse dispersion compensation including attempts at adaptive pulse shaping are presented. Finally, specific details concerning experimental data acquisition procedures and the preparation of biological samples will be discussed.

A single light source was used for all time-resolved experimentation. This consisted of a Noncollinear Optical Parametric Amplifier (NOPA) pumped by a Ti:Sapphire regenerative amplifier diagrammed below in Figure 2.1. Generation of ultrashort laser pulses takes places in multiple steps and the individual elements are outlined below.

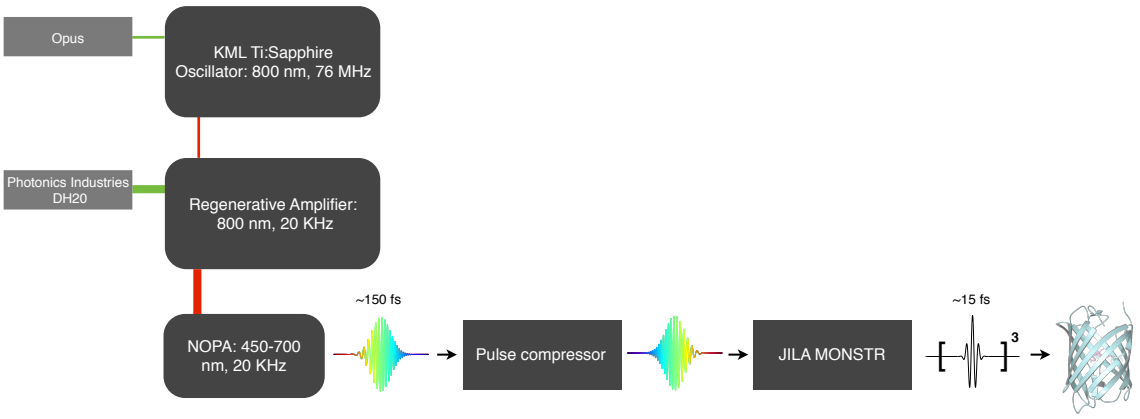

Figure 2.1. Outline of the light source used for time-resolved experimentation beginning with generation of ultrafast laser pulses at visible wavelengths and ending compressed to their shortest duration at the sample position.

Commercial Amplifier System

The principal light source is a commercial Ti:Sapphire amplifier system manufactured by KM Labs (Wyvern-20). This system outputs an 800 nm pulse train with tunable repetition rate (10-100 kHz) and a compressed duration of ~50 fs. Modern state-of-the-art turnkey amplifiers exploit a few prevalent technologies that have accelerated the development of ultrafast spectroscopies in recent years.

Solid State Gain Media

Titanium-doped sapphire (Ti:sapphire) has effectively supplanted laser dyes as the standard gain medium used in femtosecond amplifier systems. Its utility is owed to several favorable properties, namely, a large gain bandwidth of 700-1100 nm permitting tunable ultrashort pulse generation and high thermal conductivity and energy storage density (~1 J/cm^2)[114-115]. Such conditions are a great improvement over the tedious operation of dye lasers requiring continual maintenance of hazardous substances with inferior performance.

Passive Modelocking

Modelocking requires the matching of phase for several longitudinal modes within a laser cavity[116]. The result is a pulse train with frequency modulated by the cavity length and duration inversely dependent on the number of locked longitudinal modes. Several modelocking schemes have been devised and are categorized as either *active* or *passive*. The former involves introduction of electro- or acousto-optic modulation to achieve periodic intracavity loss, but are generally limited to picosecond pulse durations given their instrinsically slow response and typically require complex electronic hardware. *Passive* locking strategies typically rely on a static optical component, such as an intracavity saturable absorber (*e.g.* SESAM) to achieve momentary and predictable resonator loss[117]. A much more rapid modulation is possible compared to *active* modelocking enabling femtosecond pulse durations making it suitable for ultrashort light sources.

Chirped Pulse Amplification

Most modern ultrafast nonlinear spectroscopic applications require pulse energies beyond that possible with CW pumped amplifier systems at medium repetition rates (10-100 kHz)[118]. As such, current state-of-the-art systems rely on pulsed sources to seed the amplification stage. Chirped Pulse Amplification (CPA) has been adopted as a principal strategy to achieve much higher pulse energies while circumventing the natural physical limits of gain media when exposed to the high peak powers of ultrafast seed pulses[119]. This strategy has led to an order of magnitude increase in pulse energies and is typical of modern ultrafast light sources.

In this system, a reflective grism pair as illustrated in Figure 2.2 induces temporal chirp on the amplifier seed beam. Grisms combine the dispersive properties of both gratings and prisms and provide an efficient means of introducing seed dispersion in broadband systems[120]. A grism provides a few advantages over the standard grating stretcher method. First, its design is premised on the nearly constant GVD/TOD ratio in most materials and introduces negative GVD and TOD as a function of their separation. As such, grism systems represent an example of Down-Chirped Pulse Amplification (DCPA) and compression is achieved by simply transmitting the amplified beam through material of the proper GVD/TOD ratio[121]. This avoids the cumbersome task of using a combination of prisms and gratings to carry out final pulse compression, which suffer from low-throughput and require tedious alignment. Finally, a grism stretcher avoids the well-known limitations multi-pass grating stretchers, e.g. alignment challenges and low throughput. The only adjustable parameters in our system are the separation, *d*, and incidence angle controlled by a micrometer rotation stage.

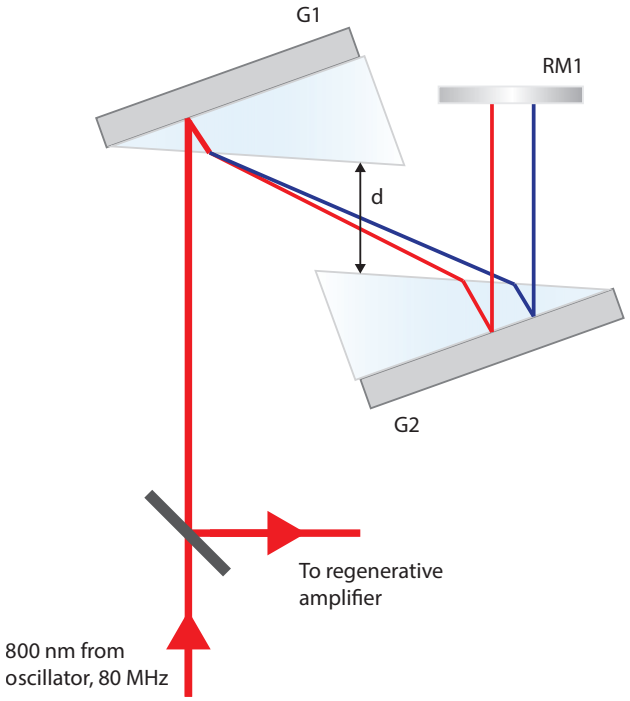

Figure 2.2. Grism pair stretcher used to chirp oscillator output seeding Wyvern-20 regenerative amplifier.

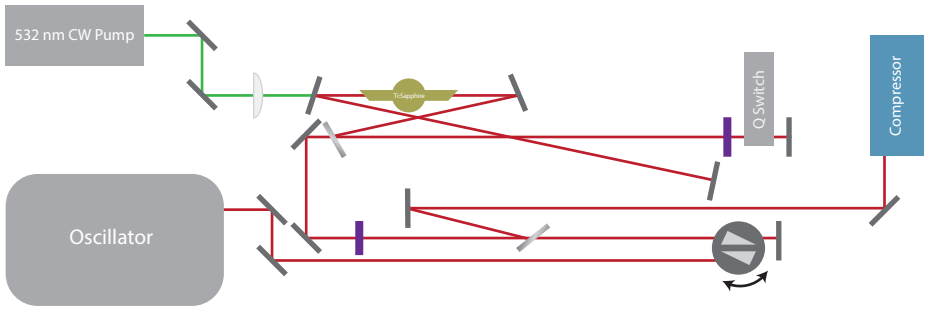

Figure 2.3. Beam diagram of the KM Labs Wyvern-20 regenerative amplifier light source.

Effective time-resolved spectroscopic experimentation demands both precise time resolution as well as a tunable light source capable of exploring a wide range of electronic transitions. Optical Parametric Amplification (OPA) represents the most reliable method to produce ultrashort optical pulses satisfying these conditions.

This phenomenon is a $\chi^{(2)}$ process that occurs in nonlinear media lacking inversion symmetry. Most commonly, β-barium borate (BBO) is used due to its high damage threshold, low group velocity dispersion, and broad transparency range[122-123]. In this process, a high frequency, high intensity beam (pump) amplifies a lower frequency, lower intensity beam (signal) while generating another beam (idler) with photon energy satisfying energy conservation.

$$\hbar\omega_p = \hbar\omega_s + \hbar\omega_i \tag{2.1}$$

It must also fulfill momentum conservation imposed by a strict phase-matching condition.

$$\hbar k_p = \hbar k_s + \hbar k_i \tag{2.2}$$

Here, **k** represents the wave vectors of participating beams. Exploiting these conditions, mixing pump and signal beams at a finite angle can amplify extremely wide bandwidths (100s of nm) across the visible spectral region. This method is known as Noncollinear Optical Parametric Amplification (NOPA). With proper selection of crystal angle, crossing angle, and dispersion, output in the visible with bandwidths of 100s of nm corresponding to pulse widths of a few femtoseconds with energies of several μJ are possible[124].

The NOPA used in this project was designed with primary consideration for output tunable between 550-650 nm with variable bandwidth. A diagram of the beam path is presented in Figure 2.4 and a brief outline of its operation now follows. First, a 5% fraction of the compressed amplifier output is split off, reflected off a controllable delay stage, and focused into a sapphire window (2 mm thickness) to

generate a white light continuum (signal). The continuum is collimated, routed to, and eventually refocused into the second BBO crystal. The stronger 800 nm fraction is then focused into a BBO crystal (2 mm thickness, 29.2°) to generate the 400 nm pump beam. This was then routed and focused into BBO2. When the pump and continuum beams have sufficient spatial and temporal overlap, the NOPA beam emits in the proper phase matching direction along $\mathbf{k_{WL}}$. The output is collimated with CM2 and routed to the compressor with flat silver mirrors.

We relied on a few parameters to achieve tunable NOPA output. First, center wavelength depends sharply on the temporal overlap between the pump and continuum beams. Appreciable output typically ranges from 450-700 nm in the present configuration. Varying the bandwidth is possible by tweaking the dispersion of the continuum beam. We introduced deliberate chirp with a flat window, W1, composed of either fused silica or BK7 with variable thickness (1-6 mm). This configuration enabled a bandwidth tunable from 10 to >100 nm dependent on selection of material and thickness. The output also generally becomes more irregularly shaped with increasing bandwidth.

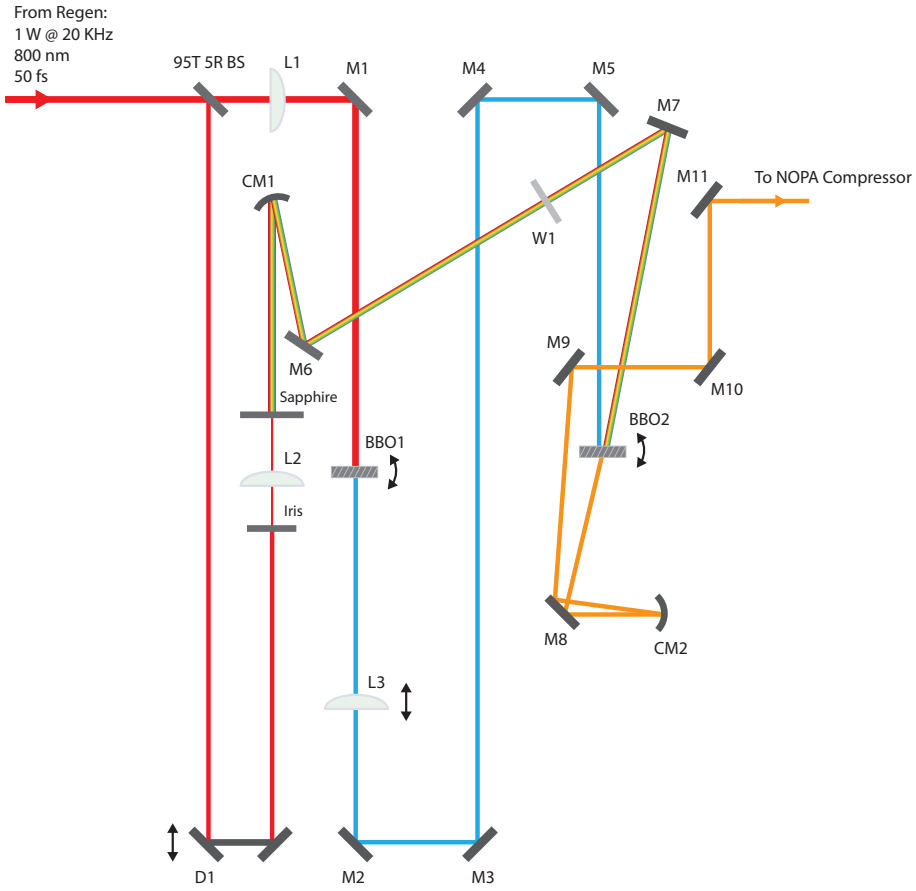

Figure 2.4. NOPA beam diagram used to generate tunable broadband femtosecond light at visible wavelengths.

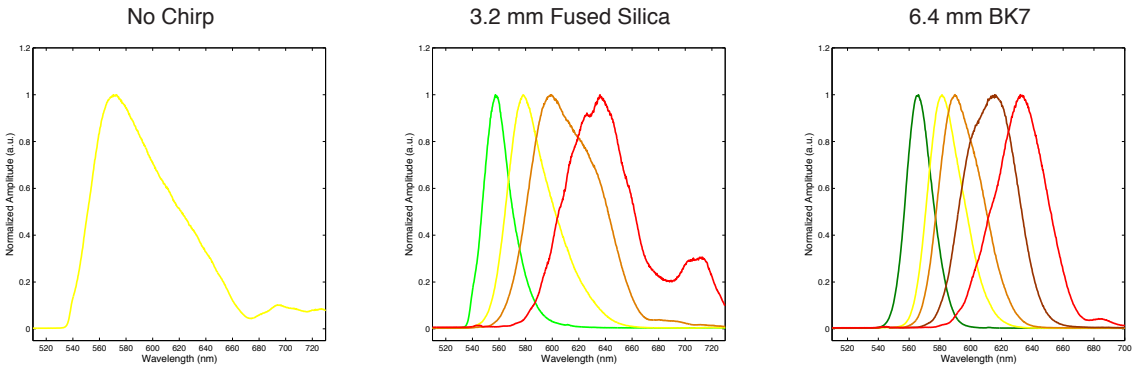

Figure 2.5. Typical NOPA spectral output with various white light chirp as a function of pump-seed delay.

2.2 Ultrafast Pulse Compression

Control of temporal pulse envelope is an important consideration for our time-resolved experimentation. This is easily conceived for a simple transient absorption experiment, where experimental time resolution is limited by the pulse duration of the probe beam. For multidimensional experimentation, however, these pulse overlap effects are manifest in less predictable ways and must be mitigated to enable proper interpretation. This section briefly details the fundamentals of material-induced dispersion and the pulse compression strategies utilized throughout this experimentation.

A wavelength dependent refractive index has a significant influence on broadband pulses necessary for ultrafast spectroscopy. This effect is commonly expressed as a Taylor Series expansion of the spectral phase as a function of frequency.

$$\varphi(\omega) = \varphi_0 + \varphi_1[\omega - \omega_0] + \frac{\varphi_2[\omega - \omega_0]^2}{2!} + \ldots \quad (2.3)$$

The second order term is frequency dependent and represents the Group Velocity Dispersion (GVD) or its analogue Group Delay Dispersion (GDD), an intensive quantity encompassing the material transmission length. The cubic and quartic terms also contribute for large bandwidths and hinder compression to very short pulse durations as well as potentially distort spectroscopic results[125].

Several strategies exist to compensate material dispersion in ultrafast experiments. The central principle of each relies on generating negative dispersion

equal and opposite that accumulated through transmissive optical components leading to the sample position.

Prism Pairs

A commonly employed method of dispersion compensation exploits angular dispersion induced by prisms or diffraction gratings[126-127]. For example, a typical compressor contains a pair of Brewster angle cut prisms arranged as depicted in Figure 2.6.

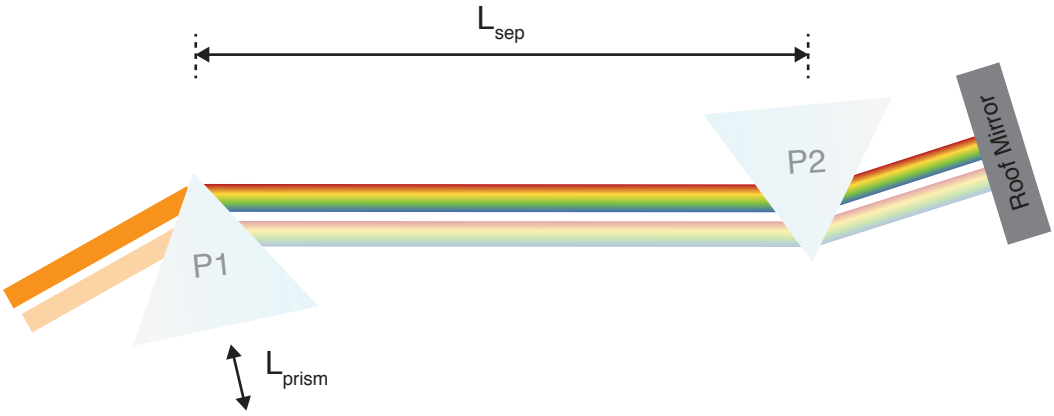

Figure 2.6. Prism pair compressor beam path used to compress NOPA output. The GDD accumulated throughout this excursion can be partitioned into contributions from the prism separation (L_{sep}) and transmission through prism material.

$$\left.\frac{d^2\varphi}{d\omega^2}\right|_{\omega_0} \approx -4L_{sep}\frac{\lambda_0^3}{2\pi c^2}\left(\left.\frac{dn}{d\lambda}\right|_{\lambda_0}\right)^2 + L_{prism}\frac{\lambda_0^3}{2\pi c^2}\left.\frac{d^2n}{d\lambda^2}\right|_{\lambda_0} \qquad (2.4)$$

The sign of the second term in Equation 2.4 is positive in the visible spectral region. Hence, precise insertion of prism material (L_{prism}) together with adjusting prism separation provides a means of tuning pulse compression. The expression above

treats only the quadratic phase. However, to generate the shortest possible pulse, one must also consider higher order terms. Since prisms and gratings have opposite relative signs of cubic phase, a common strategy is to employ them in tandem[127]. Although, this method is hindered by the low diffraction efficiency of common reflection gratings and tedious alignment required to achieve optimal compression.

Chirped Mirrors

Recent advances in thin film coating technology have accelerated the evolution of dispersion compensating mirrors[128]. Such devices are beneficial since they offer simultaneous correction of GDD and higher order dispersion with very high reflectivity. In this thesis, a chirped mirror pair (Venteon DCM10) was used, which provided -100 fs^2 GDD per bounce with TOD optimized for fused silica-type glasses. The spectral dispersion curve for each mirror is presented in Figure 2.7.

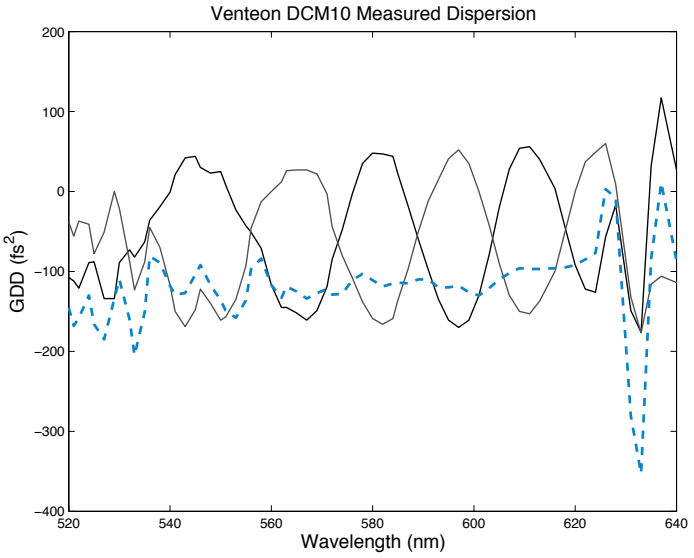

Figure 2.7. Dispersion curves for Venteon DCM10 chirped mirror pair. The black and grey curves reflect the measured GDD of the individual mirrors and the dotted blue curve represents the combined dispersion.

To achieve compensation for all optical elements before the sample position, several bounces are required separated vertically in a double-pass fashion as illustrated in Figure 2.8.

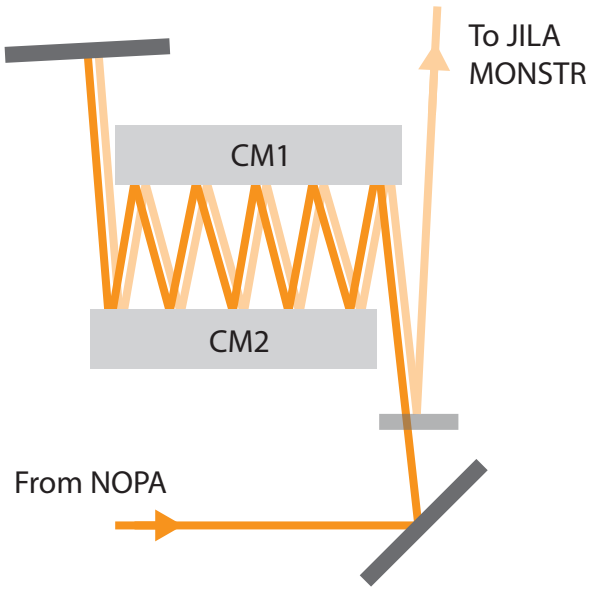

Figure 2.8. Beam path diagram for double-pass alignment of the chirped mirror pair. The reverse pass (lighter shade) is vertically separated with a roof mirror, picked off with a flat silver mirror, and sent towards the JILA MONSTR input.

The compressed NOPA output was characterized with Frequency Resolved Optical Gating (FROG). Such methods allow for extraction of pulse intensity and phase[129]. This information not only verifies proper compression, but also can be used to account for experimental artifacts in model calculations. Transient Grating FROG (TG FROG) is the most convenient diagnostic at the sample position given the BOXCAR phase-matching geometry. However, the Second Harmonic Generation analogue (SHG FROG) was also used (Mesa Photonics videoFROG) as a comparative measurement. The qualitative difference between these techniques is that TG FROG is $\chi^{(3)}$ and can distinguish the sign of pulse chirp, whereas SHG FROG is time

ambiguous[129-130]. Representative TG FROG data for the compressed NOPA output is displayed in Figure 2.9.

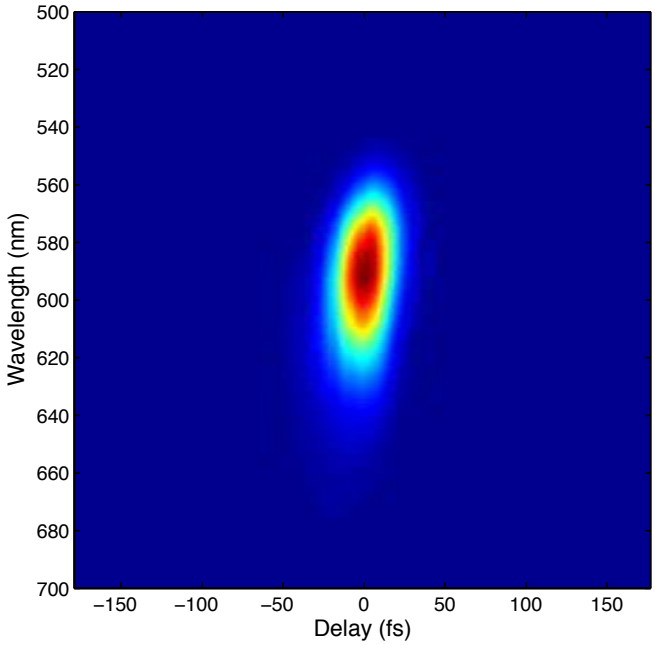

Figure 2.9. TG FROG measured from the nonresonant signal of neat benzene collected at sample position. Compression was carried out with multiple bounces off a chirped mirror pair.

Adaptive Pulse Shaping

Adaptive pulse shaping is another means of pulse dispersion compensation. Successful pulse compression has been demonstrated across a wide spectral region with several different technologies[131-134]. Moreover, this approach has been utilized to facilitate multidimensional spectroscopies in the IR and visible regimes[108, 135-137]. For optical wavelengths, typical strategies involve a 4*f* configuration where the incident light is dispersed horizontally with gratings or prisms and dispersion induced with an acousto-optic modulator (AOM) or spatial-light modulator (SLM). Common pitfalls for each include limited dynamic range, low throughput, and

inadequate spectral resolution. The effect on spectroscopic data have also been addressed[138].

Adaptive pulse shaping was carried out with a linear 12288 pixel Liquid Crystal on Silicon (LCoS) SLM acquired from Boulder Nonlinear Systems. The incident light was dispersed with a reflective holographic plane diffractive grating [333 grv/mm, Richardson #33009FL01-321R] as depicted in Figure 2.10.

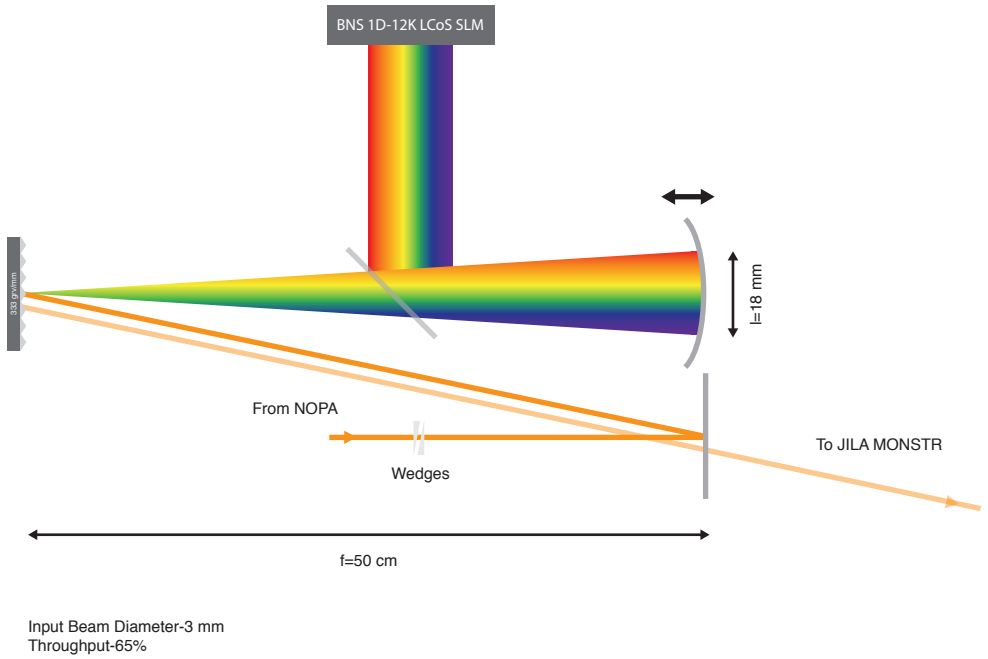

Figure 2.10. Beam diagram of the LCoS adaptive pulse shaper.

A beam diagram for the adaptive pulse-shaping device is presented in Figure 2.10. In short, the uncompressed visible pulse train exiting the NOPA light source is aligned into the diffraction grating at near the blaze angle (Θ=5.7°) to ensure most efficient reflection. The 1st order component is collimated in the horizontal dimension with a concave silver mirror (50 cm focal length, 2" diameter), incident slightly above its center axis. This mirror is tilted downward slightly to enable

pickoff with a flat rectangular silver turning mirror. The SLM is positioned for normal incidence at the focal plane. The SLM contains high reflectance dielectric coating optimized for visible wavelengths. Subsequent retroreflection follows a parallel path offset vertically to allow for transmission above the input mirror. Total throughput is roughly 65%, comparable or exceeding values reported for similar instruments[131]. A higher throughput of >80% can be achieved by substituting prisms as the dispersive element.

The optimization itself is guided by a reference signal monitored *in situ* and sensitive to the pulse duration. A common strategy exploits the nonlinearity of Second Harmonic Generation (SHG) on the shaper output. A general limitation of this approach is the finite phase-matching bandwidth of typical doubling crystals. An alternative strategy relies on the two-photon response of a photodiode, which provides a spectrally neutral diagnostic for adaptive compression optimization. Moreover, their broad spectral response provides a more cost-effective method compared to implementation of thin BBO crystals. In this effort, a silicon carbide photodiode (JEC-0.1s, EOC Inc) was employed without the protective glass cover to avoid additional dispersion. This signal was sent through a transimpedance amplifier and sampled with a NationaI Instruments DAQ board (BNC-2090A). This configuration provided a stable ~DC measurement of pulse compression independent of laser shot noise. A signal enhancement of approximately 3-fold was observed for a typical compression optimization run.

Pulse compression was carried out with two separate optimization algorithms. The first is a standard Genetic Algorithm (GA) following random polynomial generation as is typical in other reports. Convergence with this method was prohibitively slow and unreliable for efficient implementation. More consistent results were realized with a Freezing Algorithm (FA) where optimization proceeds through modulation of discrete pixel groups in a stepwise iterative fashion. This method is outlined in the flow chart below.

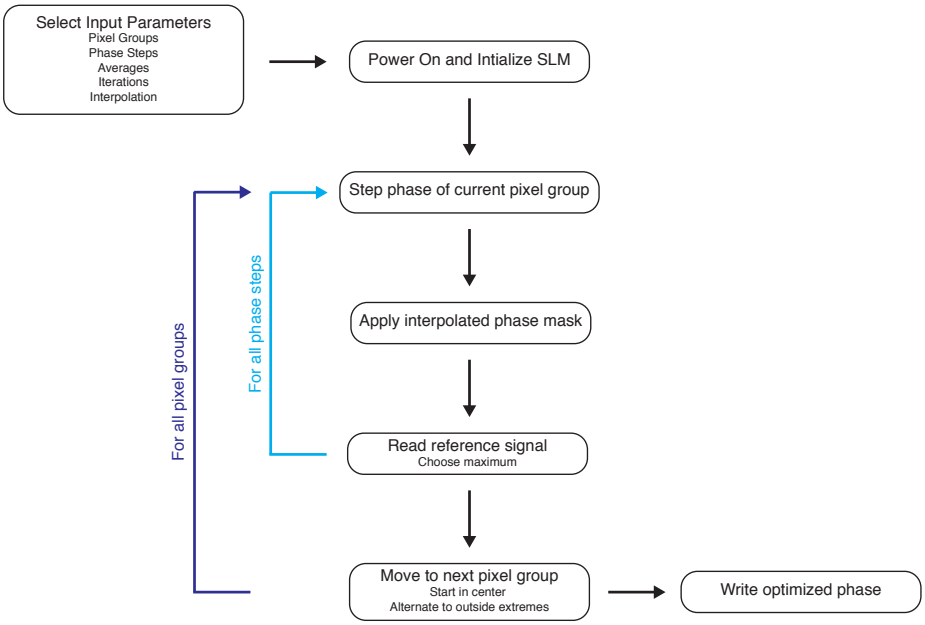

Figure 2.11. Freezing algorithm utilized for adaptive pulse compression.

For a typical FA optimization, best results were realized with the following input parameters:

Pixel Groups	30
Phase Steps per Group	10
Averages per step	3
Number of Iterations	3

Interpolation	Cubic
Starting Phase	Flat

Spectral resolution is an important quantity to consider when evaluating the limits of a given pulse shaping application. Simultaneous and independent control of both phase and amplitude is a powerful advantage for maximum utilization in spectroscopic experimentation. The latter is achieved only in the limit where a single frequency unit is subject to sufficient pixel coverage enabling application of diffractive patterns on top of the continuous dispersive mask. This relationship is generally described by the following relationship[134]

$$M(x) = \exp\left[i\Delta(x)\sin\left(\frac{2\pi x}{\Lambda}\right) + i\Phi(x) \right] \qquad (2.5)$$

Amplitude shaping is possible when the grating period (Λ) is small relative to the frequency of the light. Spectral resolution varied slightly with bandwidth in this project. An approximate value assuming a typical light spectrum (600/50 nm FWHM) is 0.008 nm per pixel for this device. This resolution should greatly exceed the limit required for independent amplitude and phase control.

SLM control was conducted with various Matlab scripts utilizing library functions (12kPCIe16Board.dll) provided by the manufacturer. Credit is given to Kapteyn-Murnane lab members Matt Seaberg, Elisabeth Shanblatt, Ming Chang, and Daniel Adams for preliminary development of this control software. Primary functions act to initialize, uninitialize, and apply an arbitrary phase mask. The following functions were used to conduct an optimization with the freezing algorithm:

FreezingGUI2.m

FreezingFcn2.m

FreezingFitness2.m

Representative pulse shaping results will now follow. The input light used in this experiment was centered at 620/55 nm FWHM and precompressed with a prism compressor yielding a pulse with mostly residual TOD. Similar results were realized without precompression, although in general, convergence consistency seemed to scale inversely with starting pulse duration. Initial optimizations began with a flat phase. Subsequent iterations were seeded with the most consistent solution. However, little improvement was observed using this strategy. The phase solution for compression of the NOPA output is shown in Figure 2.12.

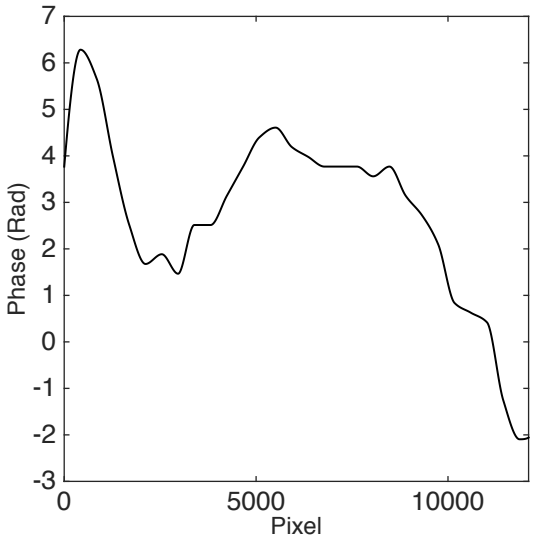

Figure 2.12. Phase obtained upon optimization with freezing algorithm with 30 pixel groups.

The compressed light was characterized with TG FROG. These results are presented in the Figures below. A shorter pulse duration is evident examining the FROG data upon optimization. Compensation of the TOD shoulder was also clear on the

positive time side in the TG FROG. However, there is interference observed within the spectral envelope that warrants additional discussion.

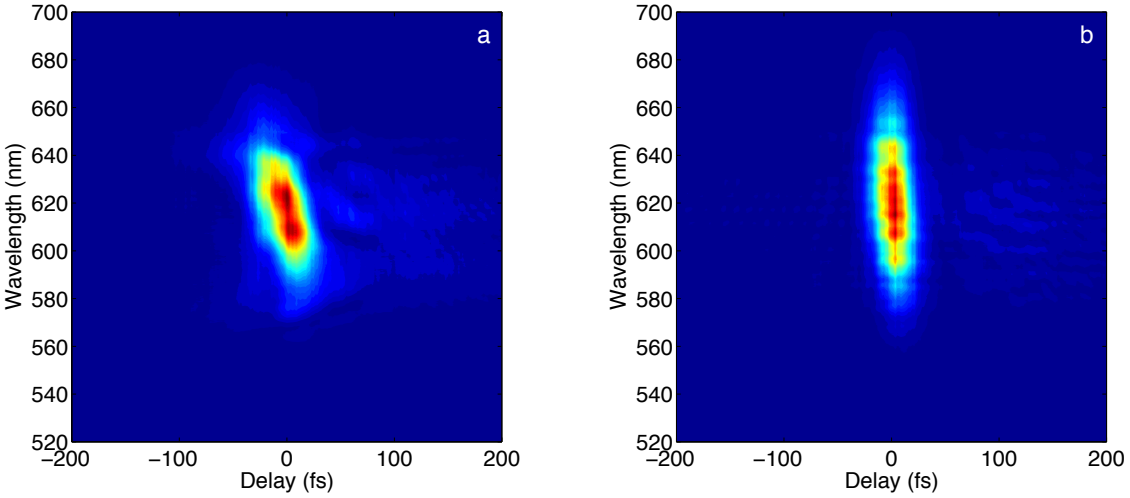

Figure 2.13. TG FROG before (a) and after (b) optimization with freezing algorithm.

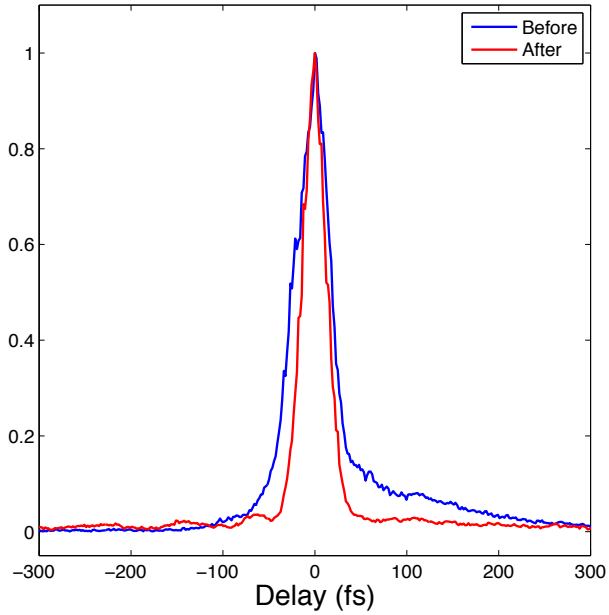

Figure 2.14. Integrated TG FROG signal before (blue) and after (red) optimization.

Since third order methods are intrinsically time unambiguous, the TG FROG results demonstrate the compensation of third order chirp. In particular, the shoulder observed in integrated FROG spectrum, is evidence of this effect. There

still remains, however, a small observable shoulder at small positive delays upon optimization. In the end, the pulse duration, assuming a Gaussian envelope, was reduced from 26.7 to 16.8 fs. The SHG FROG results were in agreement and the extracted spectral phase reveals apparent residual high order dispersion following adaptive optimization. Unfortunately, a similar quantification of spectral phase from TG FROG is not possible within a homodyne detection scheme. Future efforts will concentrate on improving this measurement.

TG scans were performed on nile blue in acetonitrile to explore the effect of pulse compression on an electronically resonant sample and to compare with previous experimental results. The data agrees with previous measurements compressed with a prism pair, however, anomalous spectral distortions are observed within the pulse overlap region at sub-picosecond delays.

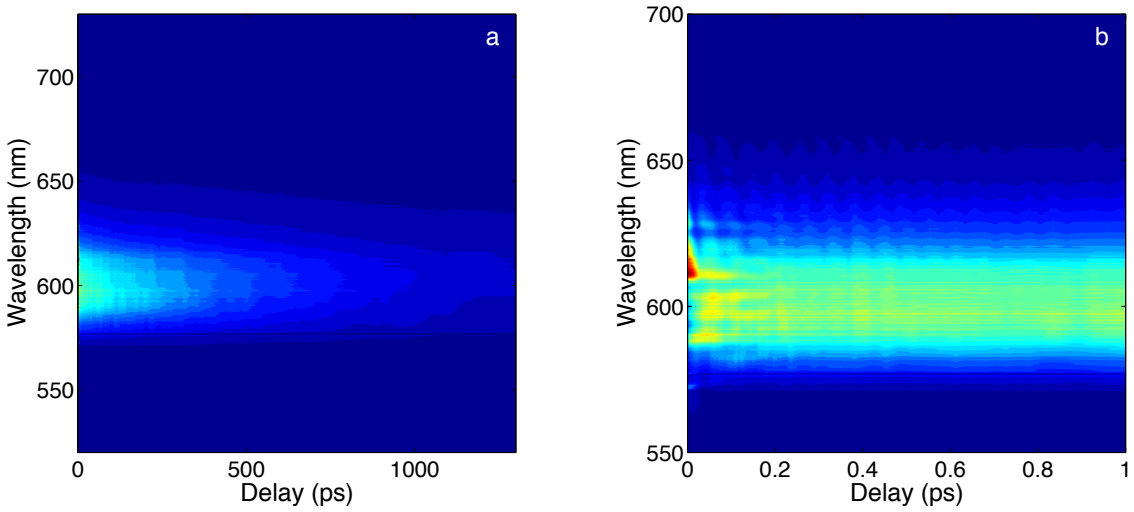

Figure 2.15. Nile Blue in acetonitrile TG spectrum following compression with freezing algorithm at late (a) and early (b) delays.

This contrast is even greater when compared to data collected with the SLM off (Figure 2.16) where obvious spectral distortions are observed. This complex

interference pattern in frequency suggests an equally distorted temporal profile as shown in Figure 2.17.

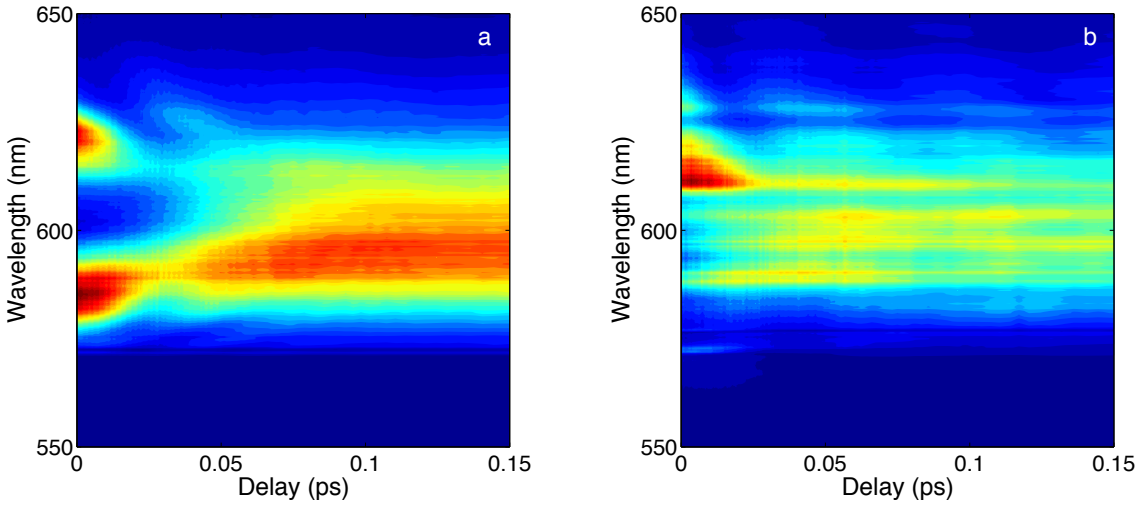

Figure 2.16. Nile blue TG data at early delay and respective frequency slices with SLM off (a) and on (b).

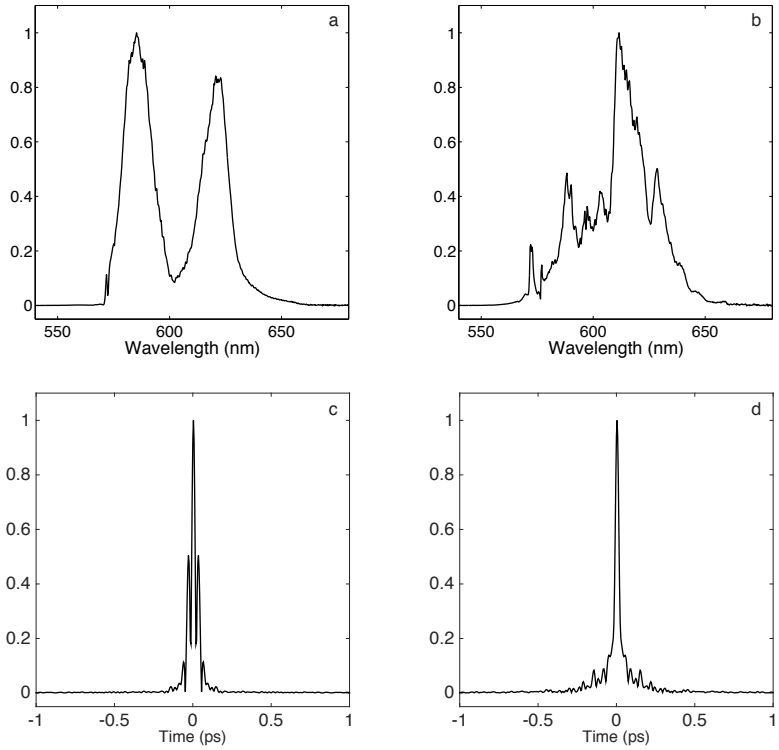

Figure 2.17. Frequency and temporal representations in the pulse overlap region of a nile blue TG spectrum with SLM off (a,c) and on (b,d).

Time domain representations of the spectral envelope reveal striking differences whether the SLM is powered on. When powered off, the primary interference occurs between the fundamental and significant contribution at ~35 fs followed by a smaller contribution at ~68 fs. When the SLM is powered on, the time spectrum becomes much more congested with several minor components evident out to nearly 500 fs.

The enhancement of this effect for resonant signals is clear when applying a periodic phase. Figure 2.18 illustrates the effect of sinusoidal phase with 5-radian amplitude on resonant (nile blue) and nonresonant (benzene) samples.

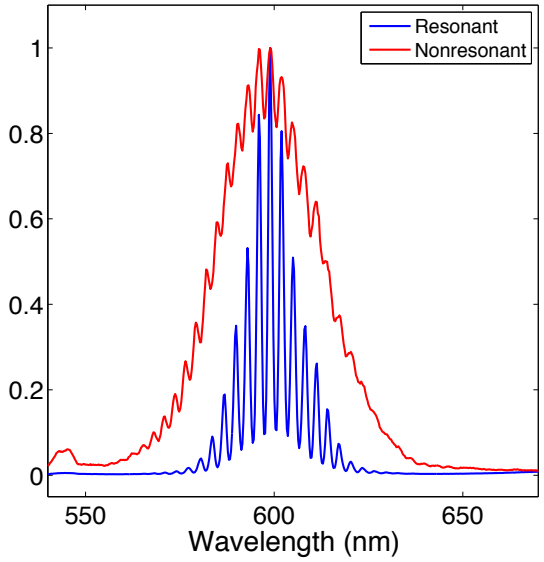

Figure 2.18. Spectral envelope following application of a sinusoidal phase on resonant (nile blue) and nonresonant (benzene) samples.

The results reported above demonstrate independent phase and amplitude control with an adaptive pulse shaper. No previous reports of this application are known for a reflective LCoS SLM at visible wavelengths. Moreover, the 65% throughput represents a 2-3 fold improvement over transmissive liquid crystal

devices. Unfortunately, lingering hardware issues compromised its full utilization in nonlinear experimentation.

The anomalous temporal interference reported above is likely related to diffraction observed across the beam following reflection off the SLM. A visible change is observed when toggling the SLM power on/off where seemingly discrete orders of stray light transform into a near continuum of light overlapping with the fundamental zeroth-order beam (Figure 2.19). Consultation with the manufacturer led a collaborative effort to identify the cause of this issue.

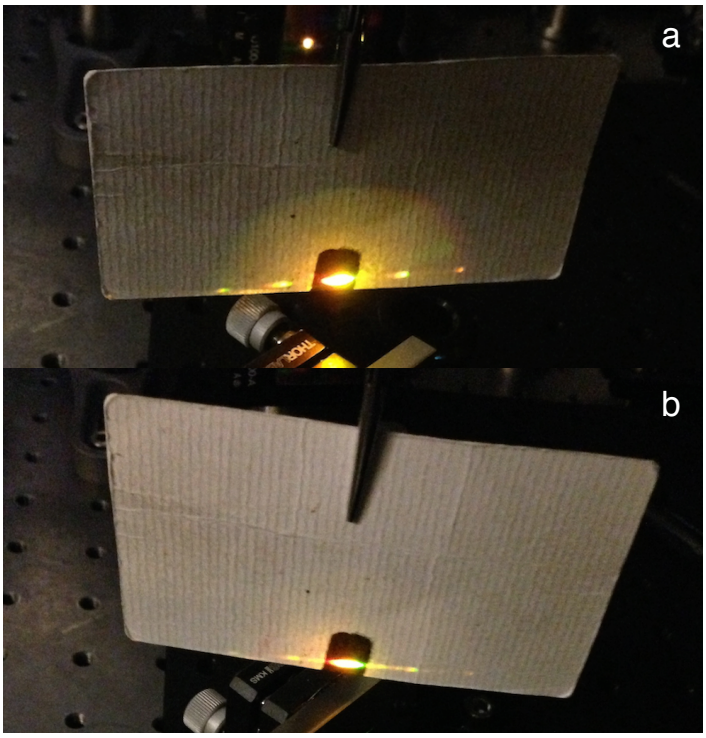

Figure 2.19. Photographs of light reflected off the SLM with power off (a) and on (b).

Upon further inspection, BNS discovered a similar diffractive effect with other devices and its extent was seemingly variable and random. They also identified a periodic 32-pixel aberration within the silicon layer containing the

electrode elements that possibly correlated with its presence. Unable to devise an immediate remedy for this fabrication dilemma, a couple possible solutions were attempted. First, BNS replaced the original device with one demonstrating less of the anomalous diffraction behavior. This substitution had a notable improvement in the resonant FWM spectrum shown in Figure 2.20.

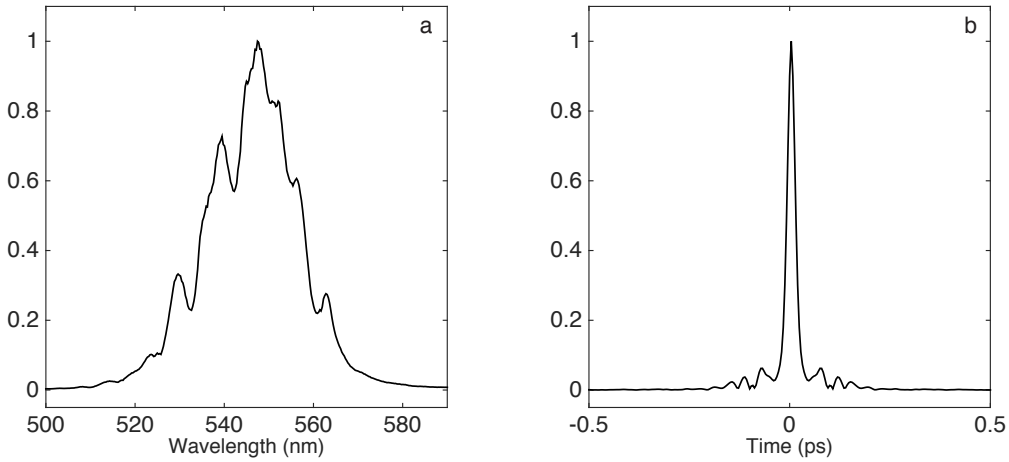

Figure 2.20. FWM spectral envelope and corresponding temporal spectrum for a second SLM.

Unfortunately, the magnitude of this improved interference still exceeds that necessary for facile utilization in nonlinear experimentation. A second proposed solution involved *in situ* electronic compensation of this periodic aberration by application of an inverse grating pattern. However, little or no improvement was realized with this strategy. Finally, a spatial filter (50 μm) was introduced between the pulse shaper and sample position to help separate extraneous diffracted light from the fundamental excitation beam. Partial improvement was observed, but not of sufficient quality for experimental utilization.

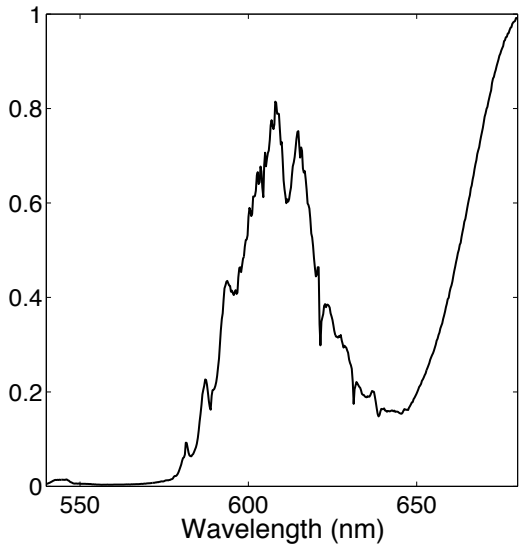

Figure 2.21. Spectral envelope of nile blue FWM signal with spatially-filtered excitation.

We discovered that temporal pulse structure has a significant influence on the shapes of peaks our 2D spectra. This is especially true at small delays when the pulses partially overlap along the T and τ time dimensions. As such, accurate characterization of pulse phase is essential for minimizing these distortions and correct interpretation of spectral features.

2.3 JILA MONSTR Nonlinear Optical Platform

Multidimensional spectroscopy demands subcycle phase stability to ensure accurate detection of the signal field. This becomes even more critical at optical frequencies where ambient mechanical fluctuations induce appreciable phase drift. Several phase stabilization strategies have been devised to mitigate this problem. Passive methods rely on common optical paths, compact experimental design, and robust mechanical construction[107]. However, these apparatus are often hindered by limited temporal range and restricted experimental resolution. This is a particular

challenge for biological systems where the slowest vibrations fall outside of the typical detection limit. Alternatively, active phase stabilization schemes utilize feedback loops or pulse shapers to control pulse phase *in situ*[108, 135]. These methods are also inhibited by experimental geometry, restricted temporal range, and related considerations.

Nonlinear spectroscopic experimentation in this project was conducted with the JILA Multidimensional Optical Nonlinear SpecTRometer (MONSTR)[106]. This instrument was developed as an actively-stabilized nonlinear optical platform capable of generating 4 phase-locked femtosecond pulses in a noncollinear BOXCARs geometry. Moreover, it operates across a wide spectral range (400-800 nm) with appropriate optical components and can access population delays of >1 ns making it a versatile tool for conducting multidimensional spectroscopy. The internal configuration of this apparatus is outlined in Figure 2.22.

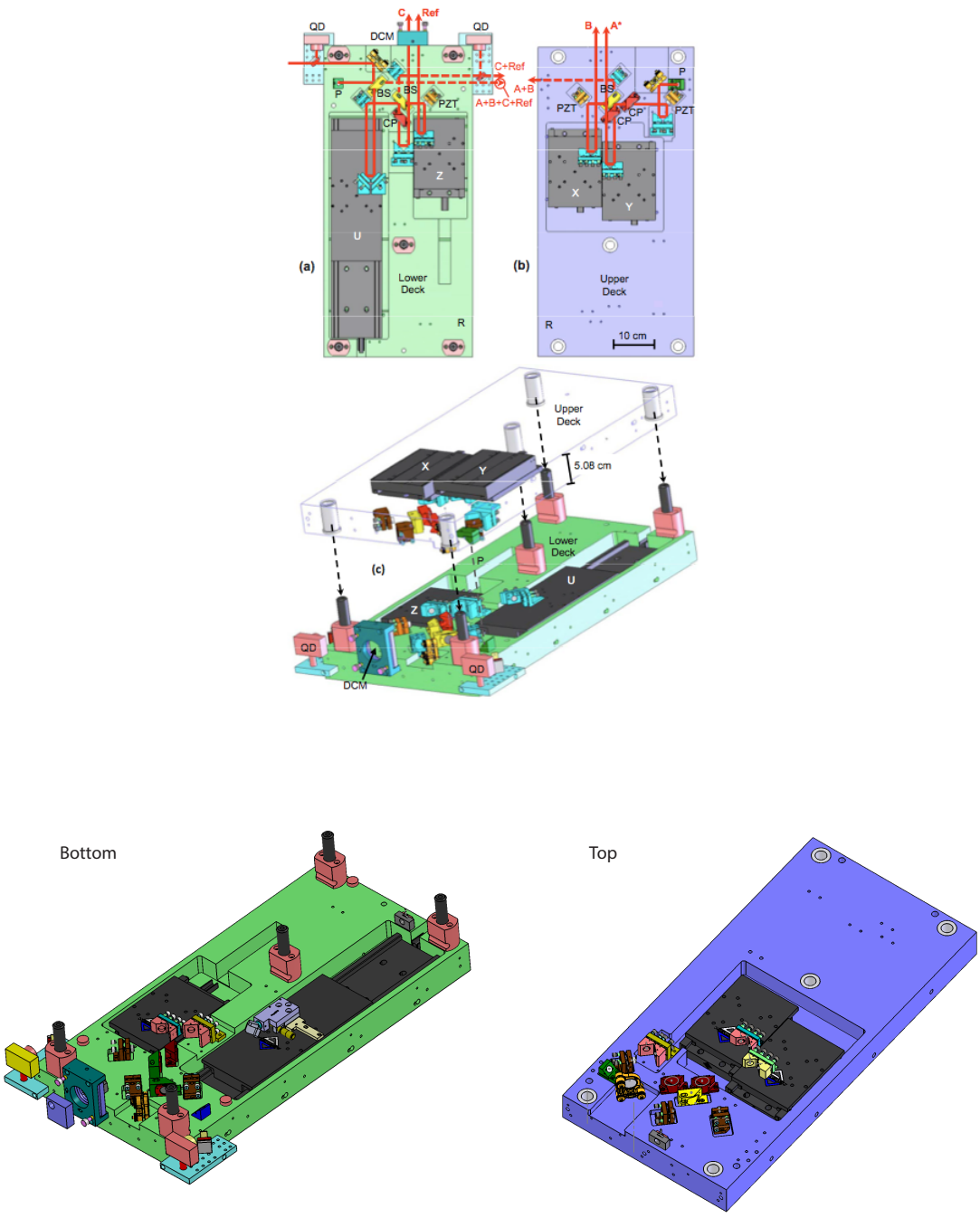

Figure 2.22. CAD drawings of JILA MONSTR assembly and beam paths.

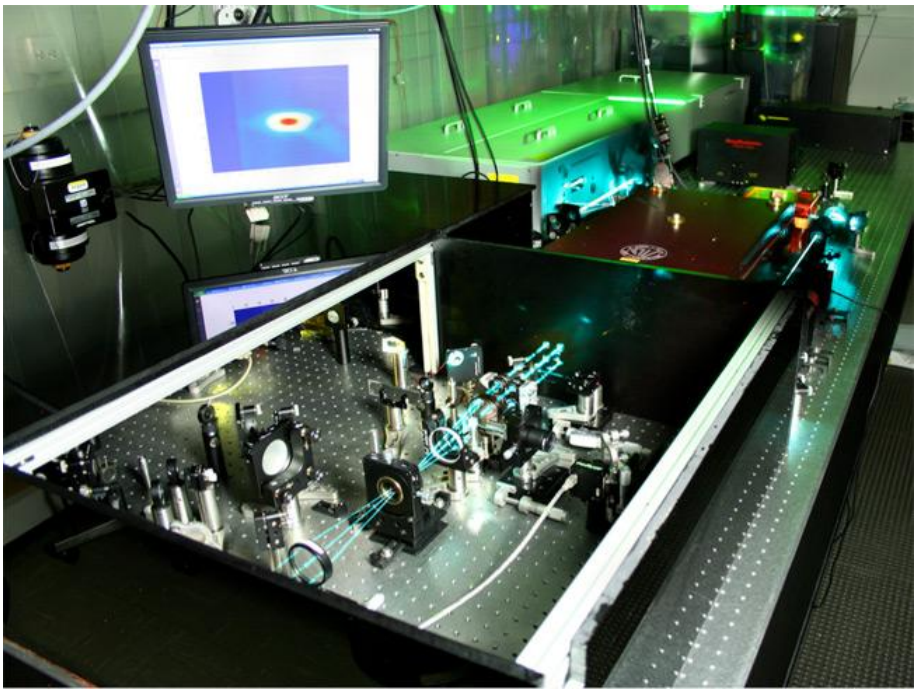

Figure 2.23. Photographs of JILA MONSTR nonlinear optical spectroscopic platform.

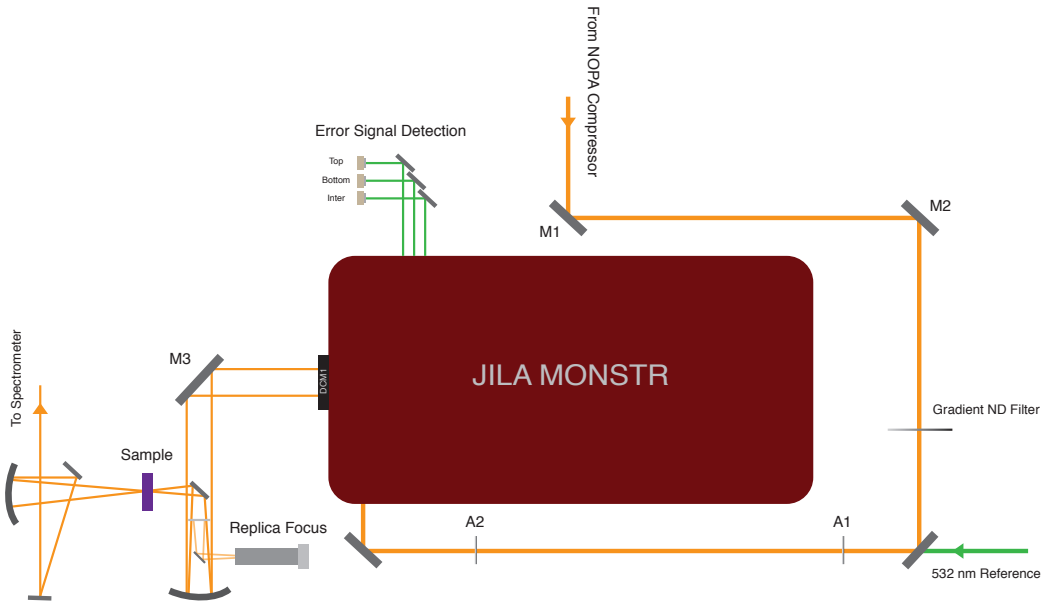

Figure 2.24. Beam path outside of JILA MONSTR.

Active Phase Stabilization

Interferometric detection of the signal field requires control of pulse time delays with subcycle precision. At visible wavelengths, this equates to roughly a 10s

to 100s of nanometer lengthscale, which is on the order of ambient mechanical fluctuations and can potentially compromise detection and ultimately, spectral interpretation. Several methods have been used to mitigate this effect. Passive phase stabilization is accomplished by compact mechanical design and use of diffractive optics[107, 109]. The JILA MONSTR incorporates an active stabilization system utilizing feedback loops that exert interferometric phase control along each beam path with piezo-driven mirrors. The phase drift is evident by following the heterodyne signal interference on the timescale of experimental data acquisition. Figure 2.25 displays FWM spectra serially collected over a 5 s interval. Phase migration is clear without utilization of feedback loops where fluctuations on the order of the signal wavelength are evident. Activation of the stabilization system was found to produce a typical phase stability of >λ/200 calculated on the basis of the locked error signal RMS deviation for each feedback loop.

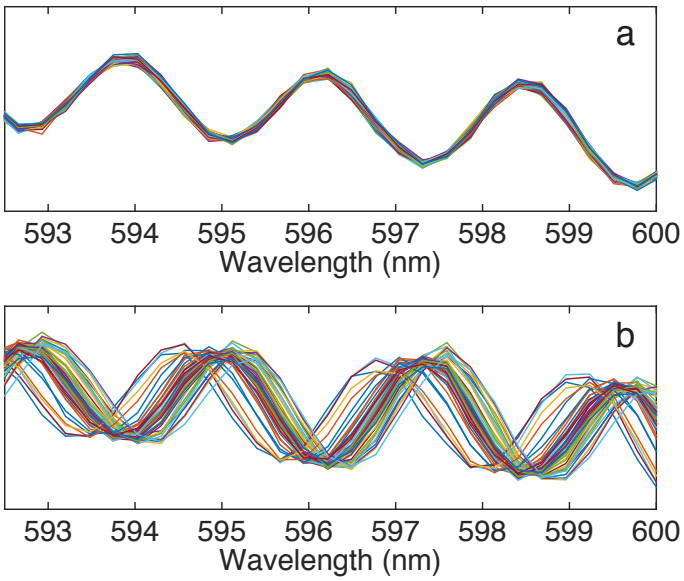

Figure 2.25. Error signals (a) with and (b) without activation of the phase stabilization feedback loops.

Phase Retrieval Procedure

Phase instability can also compromise extraction of the absolute signal phase resulting from slight imprecisions in pulse timing at the sample position. This ambiguity prevents determination of absorptive lineshapes and may complicate physical interpretation. This challenge is further compounded for measurements on biological systems where the exact bath coupling is unknown *a priori*. Several strategies have been devised for extracting the absolute signal phase. The most frequently used method, known as the projection slice theorem, equates the spectrally-resolved transient absorption spectrum at a given population time to the projection of a purely absorptive 2D spectrum along the emission frequency dimension[139]. This method is known to work reliably for strongly absorbing samples, but is hindered for cases of low excitation density, cross-polarized excitation, and double quantum coherence spectra. Moreover, replicating the exact excitation conditions in a second measurement is a tedious experimental burden. Alternative techniques have been proposed to overcome these obstacles including all-optical procedures that rely on *in situ* correction of phase drift using a pulse shaper or duplication of the beam overlap at the sample position for more efficient extraction of global phase offsets[140]. In this project, a combination of the projection slice technique and the all-optical method proposed by Bristow *et al.* are used to retrieve the absolute signal phase[141]. The SRTA spectrum used for the former method was collected as described above before each respective 2D scan.

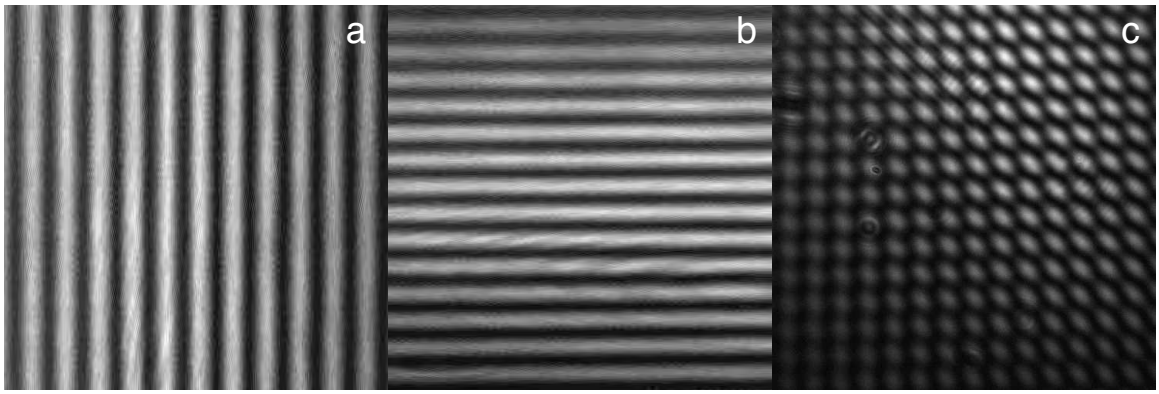

Figure 2.26. Field correlations for (a) XY, (b) YU, and (c) XYUZ beam combinations collected at the replica focus position used in absolute phase retrieval.

Phase Cycling

Excitation beam scatter is a universal challenge for most laser spectroscopies. This is especially true for liquid biological samples that are prone to aggregation and cases where a spinning sample cell is used to facilitate data collection. Heterodyne detection coupled with interferometric temporal control allows for implementation of a straightforward phase cycling procedure to minimize background scatter and improve data quality.

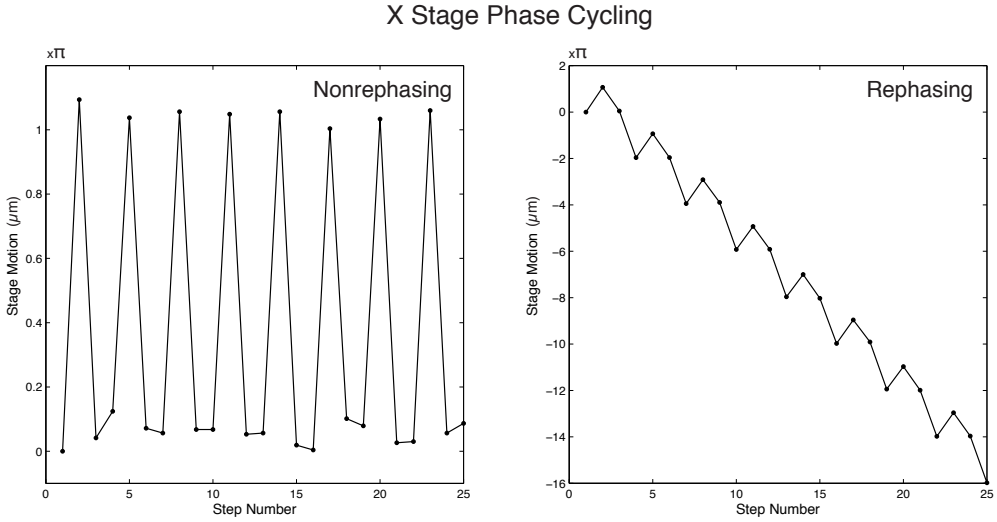

Figure 2.27. Stepping sequence for X-axis phase cycling in nonrephasing and rephasing data collection scans.

In principle, it is possible to phase cycle and eliminate scatter contributions from all excitation beams, however, it becomes increasingly time consuming to account for all phase-shifted permutations with each additional axis. For this study, phase cycling of one or two axes was sufficient to facilitate efficient collection of high quality 2D data. The stepping pattern for this procedure is described in Figure 2.28. These plots illustrate rephasing and nonrephasing stepping patterns for the X axis. For the rephasing response, X is phase cycled concurrent with scanning the τ delay ($d\tau=2\pi$), while for the nonrephasing response, X is idle and its only movement reflects the π-shifts associated with phase cycling. Interferograms are collected for the "zero-" and π-shifted cases and combined to yield the final scatter-free spectrogram. This effect is demonstrated in Figure 2.28 where the phase-cycled data quality is noticeably improved.

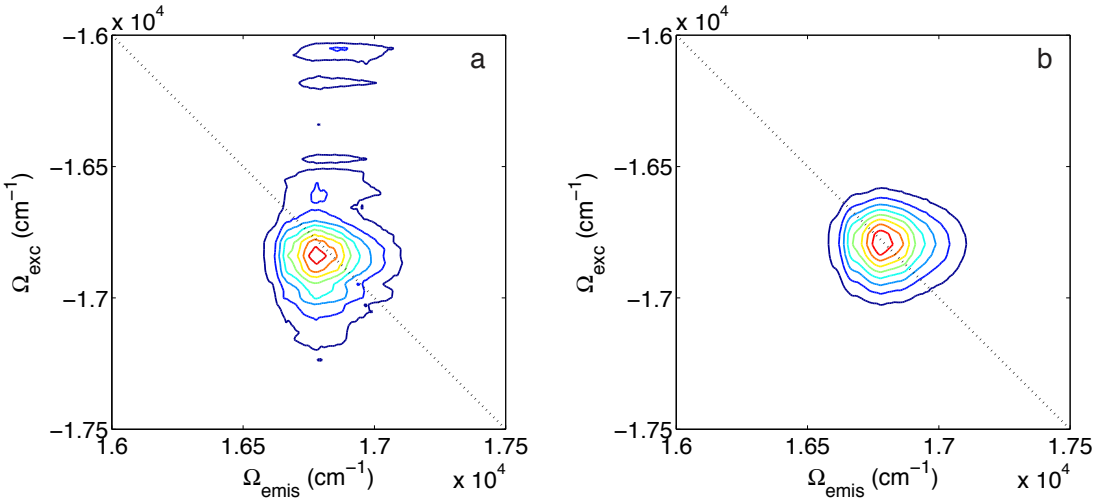

Figure 2.28. Absolute value rephasing 2DFTS spectrum of Mg-myoglobin (a) without and (b) with phase-cycled data collection.

Output and Sample Position

Upon exiting the JILA MONSTR, the excitation beams are directed to the sample position as illustrated in Figure 2.24. The beams are first turned 90 degrees with a flat 2-inch square silver mirror (M1) towards a 2-inch diameter spherical mirror (focal length=20 cm). A surface reflection off a 1-inch diameter, 1 mm thick fused silica window with backside antireflection coating is back reflected, turned 90 degrees, and focused into a 40x microscope objective, and detected with a CMOS camera (Mightex). This overlap represents a replica of the sample focal plane and is used for beam alignment and extraction of the global signal phase as described above. The converging transmitted beams are picked off with a 1-inch diameter silver mirror and turned 90 degrees towards the sample position. The beams are collimated with an identical 20 cm focal length 2-inch diameter spherical mirror. The signal is picked off with a 1-inch square silver mirror and directed towards the spectrometer for detection.

2.4 Data Acquisition Procedures

This section will detail typical data acquisition procedures for the various nonlinear spectroscopic experiments utilized in this thesis.

Transient Grating FROG

Transient Grating FROG experiments were performed by scanning $\mathbf{k_3}$ through a specified interval about $\mathbf{k_1}$ and $\mathbf{k_2}$ overlapped at time zero. The FWM signal was homodyne detected with a liquid N_2-cooled CCD camera. Typical experimental parameters:

Scan length	200 fs
Step size	1.7 fs
Integration Time	20 ms
Averaging	1
Total scan duration	~1.5 minutes

Spectrally-Resolved Transient Grating Spectroscopy

Spectrally-Resolved Transient Grating (SRTG) spectroscopy was performed by scanning $\mathbf{k_3}$ at a specified positive time delay with $\mathbf{k_1}$ and $\mathbf{k_2}$ overlapped at time zero. The FWM signal was homodyne detected with a liquid N_2-cooled CCD camera. Prior to the scan, a background at -500 fs delay was collected and subtracted from the final data to compensate for residual steady state fluorescence and excitation beam scatter. Heterodyne detection was used for measurement of weak signal intensity.

Scan length	1.3 ns
Step size	varied
Number of steps	varied
Integration time	20 ms
Averaging	1
Total scan duration	~5 minutes

Spectrally-Resolved Transient Absorption Spectrsocopy

Transient Absorption (SRTA) spectroscopy was performed in the standard pump-probe geometry. $\mathbf{k_3}$ and the local oscillator were used as the pump and probe beams respectively. The probe was attenuated with a neutral density filter to an intensity ratio of approximately 10:1. Pump modulation was carried out in one of

two possible ways. In one method, the pump beam was modulated at a harmonic of the laser repetition rate with a chopper wheel (New Focus 3502). Alternatively, this beam was blocked with a computer-controlled mechanical shutter. Integrated measurements were detected with a lock-in amplifier (Stanford Research 830) and photodiode (Thorlabs DET36A). Spectrally-resolved measurements were detected either with a liquid N_2-cooled CCD camera or a fiber-coupled USB spectrometer (Ocean Optics USB3000+). This method combined with synchronization of an optical chopper provides the most sensitive means of TA experimentation.

3PEPS

Stimulated Photon Echo Peak shift data was collected in the BOXCARs excitation geometry. Rephasing and nonrephasing responses were collected in a continuous scan by first starting $\mathbf{k_2}$ at positive time and collecting data backwards towards time zero (nonrephasing). The rephasing half followed by collecting data forward in time stepping $\mathbf{k_1}$. This strategy helps mitigate time missteps associated with acquiring the complete response in two separate (rephasing and nonrephasing) halves. Spectrally-resolved heterodyne or homodyne detection was carried out with a liquid N_2-cooled CCD camera dependent on the signal strength. Phase stabilization was utilized for the case of heterodyne detection. The integrated FWM signal versus τ was fit to a suitable function. The peak shift was determined by extracting its center position. Previous reported electronic 3PEPS measurements employed a triangular excitation beam geometry where the rephasing and nonrephasing signals emit in unique phase-matching directions[101, 142-144]. Whereas, vibrational echo experiments carried out in the BOXCARs geometry have been

previously reported[102, 145]. To measure the solvation correlation function and relative inhomogeneity, the peak shift was collected as a function of population time (T). Since our population time interval is limited to ~1.3 ns, all dynamics occurring beyond this were considered *static*.

Scan length	varied
Step size	2 fringes
Number of steps	varied
Integration time	10-20 ms
Averaging	1
Total scan duration	~2 minutes

Multidimensional Spectroscopy

Two-dimensional single and double quantum coherence data was collected in the BOXCARs excitation geometry. Rephasing and nonrephasing responses were collected, as with 3PEPS, in a continuous scan by first starting $\mathbf{k_2}$ at positive time and collecting data backwards towards time zero (nonrephasing). The rephasing half followed by collecting data forward in time stepping $\mathbf{k_1}$. Spectrally resolved heterodyne detection was employed with a liquid N_2-cooled CCD camera. An I_{LO}:I_{FWM} ratio of 4:1 was achieved with neutral density filters along the LO beam path before combination with the FWM signal. Phase stabilization was utilized to ensure proper resolution of the signal field. Phase-cycling was carried out to facilitate direct quantification E_{FWM} without subtraction of noncontributing elements from the local oscillator, excitation beam scatter, and steady state fluorescence. Quantification of Ω_{emis} was accomplished through spectral resolution of the FWM

signal at each τ delay. While Ω_{exc} information was accessed via subsequent Fourier transformation following acquisition of the entire spectrogram. Resolution along the emission axis is limited by the spectrometer and was ~8 cm^{-1} at 600 nm using a 300 grv/mm dispersion grating. Resolution of the excitation frequency was dictated by step size and scan length along τ in accordance with the Fourier theorem.

Scan length	varied
Step size	2 fringes
Number of steps	varied
Integration time	10 ms
Averaging	1
Total scan duration	~2 minutes

2.5 Sample Preparation Protocol

This section will describe preparation of samples utilized throughout this thesis.

Fluorescent Protein Expression and Purification

Fluorescent protein growth and expression was conducted in accordance with reported accounts, but with some variation for select species[11, 44, 50]. Namely, small differences in buffer composition and pH, *E. coli* cell strain, and expression conditions were tweaked to optimize protein production. The following protocol was typical for most RFP derivatives. In short, a protein gene was ligated into the pBad expression vector and subsequently transformed into Top10 competent cells. Transformed competent cells were cultured on agar plates (LB+ampicillin) and a starter culture (5-15 mL LB + ampicillin) was grown overnight at 37 °C from a single colony pick. This starter culture was then used to inoculate an expression

culture=50-100 mL of 2XYT media (100x dilution) in a 250 mL Erlenmeyer flask. The expression culture was grown at 37 °C until cloudy (OD_{600}~0.6) and subsequently induced with 0.2% arabinose (pBad). The temperature was then reduced to 30 °C and expression proceeded for 24-48 hours. The cultures were harvested by spinning in a centrifuge at 7000 RPM for 12 minutes and discarding the remaining supernatant. The residual pellets were preserved at -80 °C for future extraction and purification. Examples of poor and rich protein cultures are shown in Figure 2.29.

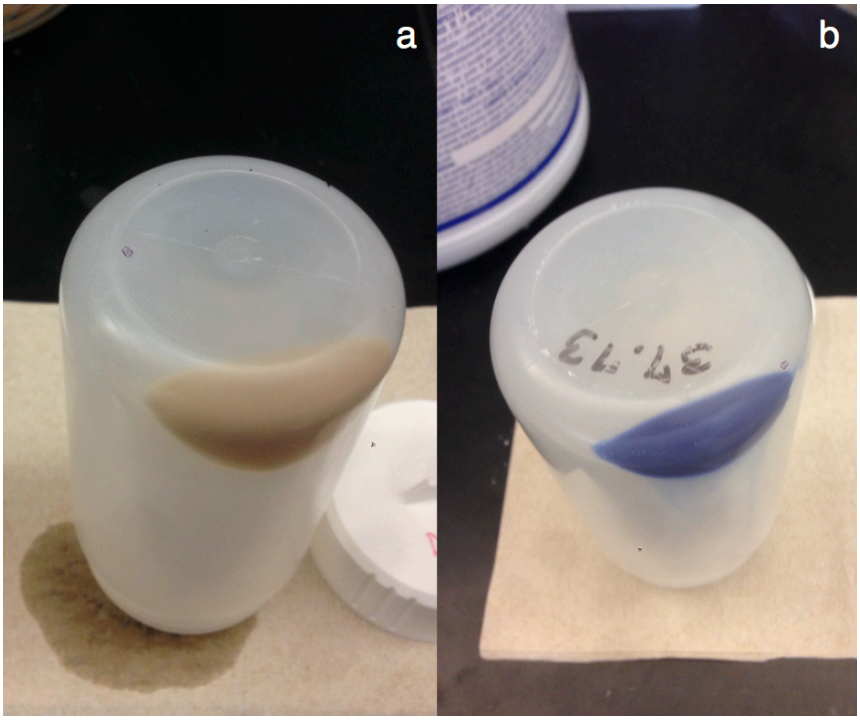

Figure 2.29. Photographs of a (a) low and (b) high yield fluorescent protein cell pellet.

The cell pellets were lysed with a commercial protein extraction agent (B-PER, Thermo Scientific) and centrifuged to remove macroscopic cellular debris. The crude product was then loaded into a Ni-ATA column and incubated for 10-15

minutes in an ice bath. Elution of the purified protein was carried out by flowing buffer containing increasing concentrations of imidazole (10-150 mM) in approximately 5 separate rinses. The final product was either refrigerated for immediate use or flash frozen in liquid-N_2 to preserve for future experimentation.

Site Directed Mutagenesis

Point mutations of a native protein sequence were used to systematically alter specific chromophore-sidechain interactions. QuikChange (Agilent) is a commercially available kit to carry out site-directed mutagenesis. Its protocol is outlined in the Figure below.

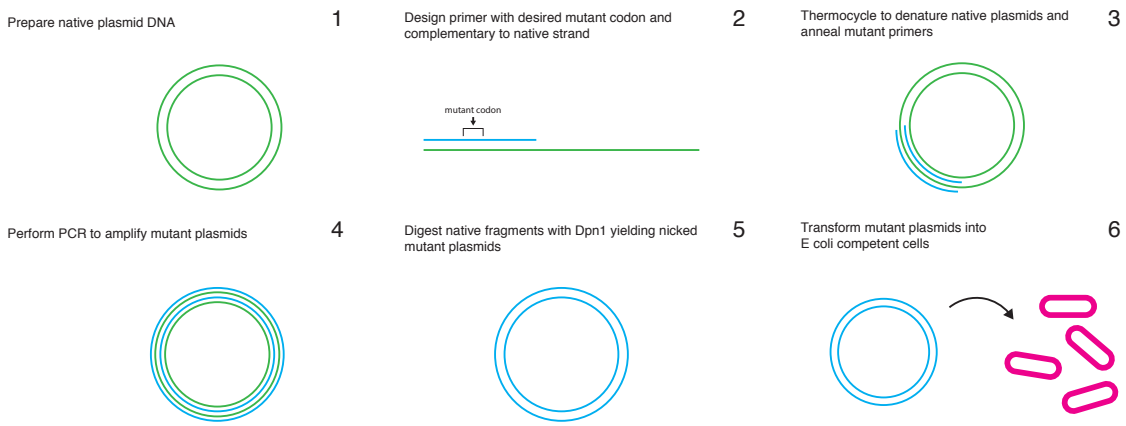

Figure 2.30. QuikChange site-directed mutagenesis protocol.

Following preparation of mutant protein plasmid DNA, expression and purification were carried out according to the previously described procedures.

Organic Dyes in Bulk Solvent

All organic dyes and solvents were used as received from the manufacturer unless noted in their respective section. Spectroscopic grade solvents were used whenever possible to avoid sample contamination and experimental interference.

2.6 Auxiliary Experimental Details

Sample Cell

The liquid sample was contained between two 1 inch round flat windows separated by an annular Teflon spacer. The front window is 1 mm thick *uv* fused silica and the back window is 3.2 mm thick BK7 glass. The experimental pathlength, *d*, was controlled by the thickness of the spacer and ranged from 10s of microns to 1 mm. This cell was contained within an aluminum optic mounting piece (Newport LPLH-1T), which is attachable to either a 3-axis translational mount or the spinning sample cell described below.

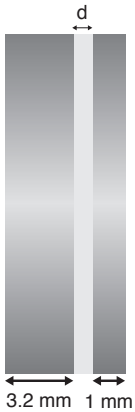

Figure 2.31. Cell used to contain liquid samples for spectroscopic experimentation.

Spinning Sample Cell

Both biological and dye samples were spun with a mechanical spinning cell for most data collection. Refreshing the sample is necessary to minimize photobleaching, diffusive fluctuations observed in the FPs, and accumulation of laser-induced byproducts with lifetimes comparable with the laser repetition rate. These considerations were evaluated by calculating the fraction of molecules in the excited state for typical experimental conditions (100 μM concentration, 50 μm spot size, 1 nJ pulse energy, 20 kHz laser repetition rate). Assuming a cell rotating at a rate of 2000 revolutions per minute, or a rotational velocity of 104.67 cm/s, ~1×10^{-6} pulses interact with a given illuminated spot on average. This equates to an approximate excited fraction of <0.0001% per spot while spinning, which should be adequately low to prevent repeated exposure of a single excited volume. Another factor considered when establishing excitation conditions is the repopulation rate of the electronic ground state. The singlet excited state lifetime of a fluorescent protein sample falls between 1-3 ns. However, a reversible dark state conversion process is known to occur in RFPs on ~ms timescale[146]. Too high a laser repetition rate would lead to accumulation of photoinduced byproducts and eventual loss of signal intensity as is observed in some porphyrin species that undergo intersystem crossing. No evidence of dark state conversion was observed with a laser repetition rate of 20 kHz.

The photographs below illustrate the spinning sample cell construction. The sample is contained within removable piece (Newport LPLH-1T) that threads directly to the rotating arm. Rotational velocity was measured by attaching a small

piece of aluminum foil on the edge of the sample cell and capturing the stray light following exposure with the 532 nm reference laser. Endurance testing revealed a constant velocity was maintained for >1 hour, which is suitable for typical spectroscopic experimentation. However, there is a short stabilization period of typically 10 minutes upon initial daily usage. This consistency was realized following conversion to a brushless DC motor and greatly exceeded that of the original, which experienced intermittent periods of acceleration and deceleration leading to baseline drift, which compromised data collection efforts.

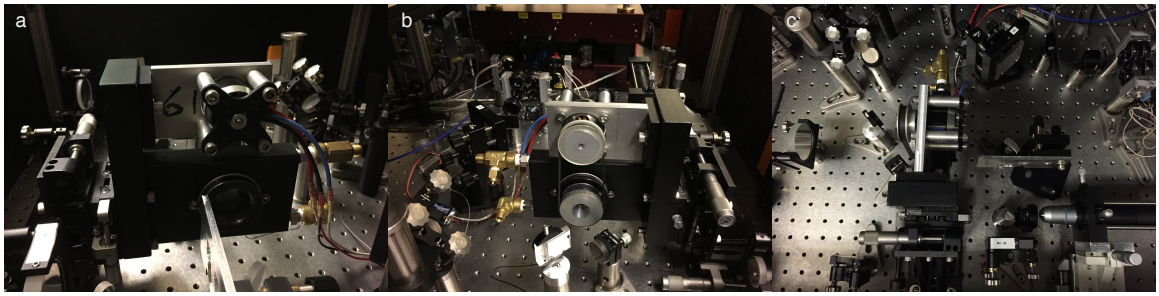

Figure 2.32. Photographs of spinning sample cell from (a) front, (b) back, and (c) top perspectives.

Phase stability was slightly hindered by mechanical vibrations accompanying rotation of the spinning cell. This is evident by monitoring the FWM signal phase over time displayed in Figure 2.33.

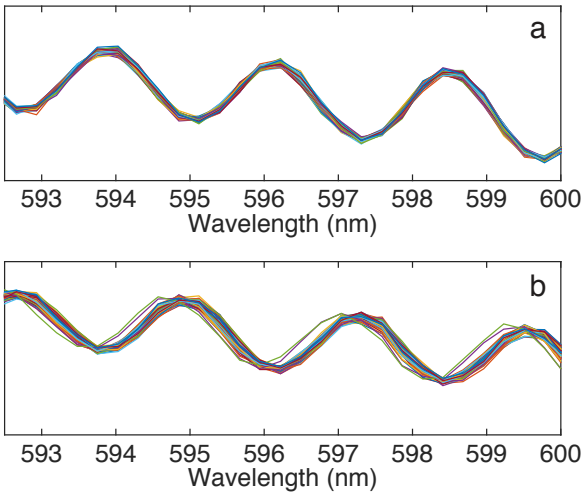

Figure 2.33. FWM signal fringe phase stability with spinning cell (a) off and (b) on.

Spinning cell components

Bearings:	B544DDFS428	Allied
Motor:	EFLM4032A	A Main Hobbies
	E-flight 32 Brushless DC	
Power Supply:	10 V/1.5 Amp DC	JILA Electronic Shop
Controller:	SPM5510	A Main Hobbies
	Spektrum DX5e	
Receiver:	CSE010-0051-00	A Main Hobbies
	Castle Creations Thunderbird 36-Amp Brushless ESC	
Pulleys:	A6A51-072NF0608	Stock Drive Products/Sterling Instruments
	Aluminum, 2 mm pitch, 0.25" bore size, 1.805" pitch diameter, 0.236" belt width	
	A6A51-060DF0608	Stock Drive Products/Sterling Instruments
	Aluminum, 2 mm pitch, 0.25" bore size, 1.505" pitch diameter, 0.236" belt width	
Belt:	A6R51M150060	Stock Drive Products/Sterling Instruments
	Timing belt, neoprene, 2 mm pitch, 300 mm pitch length	

Chapter III

Hydrogen Bond Flexibility Correlates with Stokes Shift in mPlum Variants

As Appeared in the Journal of Physical Chemistry B, 2014, Vol. 118, 2940-2048

3.1 Introduction

Fluorescent proteins (FPs) derived from marine organisms, including the green fluorescent protein extracted from the jellyfish *Aequorea victoria*, have revolutionized cellular imaging experiments and become an invaluable tool in molecular biology research[147,1]. Their utility is owed to several favorable intrinsic properties, namely, tunable excitation and emission, genetic encodability, and targetability. Next generation far-red emitting species with enhanced fluorescence quantum yields and high photostability are eagerly sought. These improvements would enable deeper tissue penetration and lengthened imaging times given a lower autofluorescence background, lower light scattering, and higher transmission beyond 650 nm[14].

The fluorescent chromophore of FPs is autocatalytically formed in the presence of molecular oxygen, and is contained within an eleven-stranded β-barrel. Electronic excitation in the chromophore occurs with electron density transferred from the phenoxy ring towards the acylimine across the π-conjugated system[148-149]. Several strategies have been used to engineer further red-emitting species[14, 18]. One approach is to extend conjugation within the chromophore itself or with nearby sidechains *via* selective mutagenesis. Alternatively, one can modify the surrounding chromophore environment leading to direct stabilization (destabilization) of the

excited (ground) state by electrostatic effects, hydrogen-bonding interactions, or isomerization. Examples of these interactions are found in several red FP species, though in most cases, interpretation is derived from crystal structures and neglects a possible dynamic element[11, 18, 47, 49].

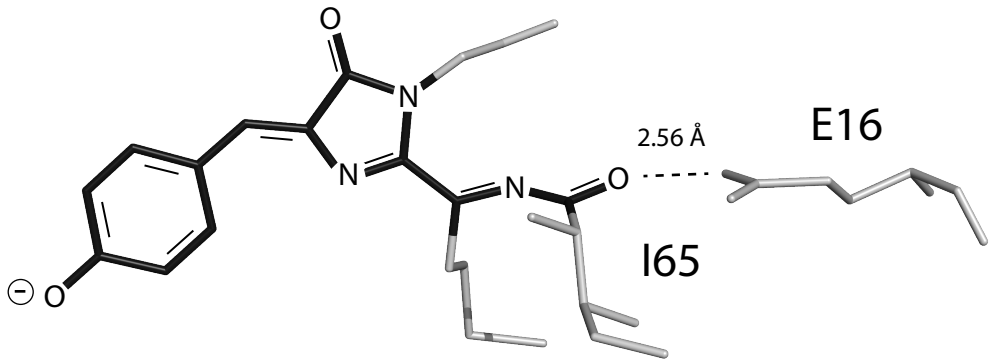

Figure 3.1. Chemical structure of mature mPlum chromophore. The hydrogen bond thought responsible for its large Stokes shift is shown as a dashed line between E16 and the chromophore terminus of residue I65.

The fluorescent protein mPlum, developed through iterative somatic hypermutation of mRFP (from the progenitor DsRed), has a peak excitation of 589 nm and a Stokes shift of 59 nm[44]. A hydrogen bond between the E16 sidechain and N-acylimine oxygen of the I65 residue at the base of the chromophore as depicted in Figure 3.1 is thought to be the key feature leading to its large Stokes shift. This hypothesis evolved from a few striking observations: first, as illustrated in the original report by Wang *et al*., steady state emission values vary widely with point mutations at these positions and all reported variants show a nearly 20 nm blue shift relative to the native E16 configuration. The Stokes shifts fall within 3 distinct groups around 25 nm, 35 nm, and 50 nm, which may imply common dynamic behavior within mutant subgroups of similar hypsochromic shift. Moreover, these

perturbations occur primarily on the excited state given the sensitivity of the emission wavelength. Second, Abbyad *et al.* identified a large dynamic Stokes shift with timescales of 4 and 71 ps in mPlum using fluorescence upconversion spectroscopy[45]. These dynamics differed from mRaspberry and mRFP, which showed very little solvation over the 1 ns probe window. They explained this shift in terms of a specific interaction between E16 and I65 on the basis of their influence on the steady state Stokes shift. This was the first report of a time dependent interaction leading to an extended red shift in FPs. These authors proposed that the solvation process resulted from an excited state rearrangement of a specific interaction between residues 16 and 65, yet their evidence did not discount the possibility that general flexibility of side-chains or water around the chromophore may be responsible. More recently, crystal structures of mPlum together with E16Q and I65L variants reaffirmed the hydrogen bond between E16 and I65 in mPlum and identified a similar interaction in the E16Q mutant[46]. They also implicated the steric influence of I65 and predict it plays a role in strengthening this hydrogen bond in the excited state.

Several different femtosecond spectroscopy techniques are capable of resolving the time dependent red-shift due to the excited state solvation dynamics[150,151]. Here, spectrally resolved transient grating spectroscopy (SRTG) is employed as previously applied by Joo *et al.* to observe nuclear wavepacket dynamics in ground and excited electronic states and solvation of dyes in bulk solvent[91, 152]. In this four-wave mixing technique, two pump pulses (with wavevectors $\mathbf{k_1}$ and $\mathbf{k_2}$) interfere imprinting a spatial grating on the sample which is

later probed by a third pulse (with wavevector $\mathbf{k_3}$) at a controllable delay that diffracts into a spatially isolated phase matching direction ($\mathbf{k_1}$-$\mathbf{k_2}$+$\mathbf{k_3}$). For a chromophore with a large Stokes shift together with a sufficient excitation window, this signal can be spectrally resolved into stimulated emission (SE) and ground-state bleach (GSB) contributions. Time evolution of the GSB and SE bands represent ground and excited state solvation dynamics respectively.

In this chapter, SRTG spectroscopy and molecular dynamics (MD) simulations are employed to explore the relationship between flexibility of the chromophore environment and the large Stokes shift in mPlum. Relaxation of a panel of strategic point mutants of the participating 16 and 65 residues was investigated. The experimental results and simulations indicate the red-shifted emission in mPlum is correlated with a facile switching between a direct and water-mediated hydrogen bond between the E16 sidechain and the N-acylimine oxygen at position 65. All discussions about the role of a hydrogen bond network in earlier papers were derived from a static crystal structure in the ground state. This chapter represents advancement in that it explores hydrogen bond dynamics around the chromophore rather than the hydrogen bond network derived from an average ground state structure.

3.2 Experimental Methods

Time-resolved Measurements

Transient grating measurements were performed in the traditional BOXCARs geometry as established in the previously described JILA MONSTR nonlinear optical platform[106]. Upon irradiation with 3 excitation pulses (20 fs, ~10 nJ/beam),

generated from a noncollinear optical parametric amplifier pumped with a Ti:Sapphire regenerative amplifier (20 kHz), the spatially isolated four-wave mixing signal emitted in the prescribed $\mathbf{k_s}=-\mathbf{k_1}+\mathbf{k_2}+\mathbf{k_3}$ phase matching direction. Excitation wavelength was chosen to maximize contrast between ground state bleach and stimulated emission components.

Table 3.1. Excitation center position and FWHM bandwidth used in SRTG measurements.

Mutant	Wavelength (nm)
mPlum	625-40
E16Q	621-50
E16H	610-40
E16L	615-45
I65L	625-50
I65A	625-50
I65V	625-50

The sample was refreshed with a spinning cell to mitigate photobleaching and accumulation of laser-induced photoproducts. Sample concentration and path length were carefully tuned to avoid aggregation and reabsorption of the nonlinear signal. Concentrations of ~50 μM and a path length of 0.5 mm were used for all samples (OD 0.15 peak absorption). Spectrally resolved detection was carried out with a liquid N_2-cooled CCD camera. Data was collected as a function of the *T* time delay ($\mathbf{k_1}$ and $\mathbf{k_2}$ temporally overlapped) from a range of 0 to 1.3 ns, spaced logarithmically, with a background spectrum collected at -500 fs delay to eliminate contributions from excitation scatter and spontaneous emission.

Protein Expression and Purification

Fluorescent proteins were expressed with a pBAD expression vector containing the mPlum gene. Point mutations were accomplished with QuikChange mutagenesis from commercial primers. Upon sequencing confirmation, plasmids were transformed into Top10 *E. coli* followed by induction with 0.02% arabinose for 24 hours at 30 °C. Samples were purified via 6X-His tag/Ni-NTA chromatography and the crude specimens were buffer-exchanged with 15 mM pH 8.0 TRIS buffer, 100 mM KCl. Emission spectra of each mutant, excited at 532 nm, were detected with a diode array spectrometer.

Molecular Dynamics Simulations

Time series trajectories were obtained from explicit solvent, all-atom simulations using the NAMD molecular dynamics package with the CHARMM27 force field[153-154]. The initial X-ray crystallographic structures were obtained from the Protein Data Bank (mPlum pdb code 2QLG, E16Q pdb code 2QLI, I65L pdb code 2QLH). The other four mutants do not have PDB structures, so we used CHARMM to make the amino acid substitution in the mPlum pdb 2QLG file. Force field parameters for the mature chromophore were adopted from the anionic GFP chromophore developed by Reuter *et al.* and from CHARMM27 parameters for acylimine nitrogen[155]. Throughout the simulation, the deprotonated anionic form of the chromophore in the ground state was used. In addition, E215 was protonated using a patch.

The VMD package was used to setup the system for simulations[156]. The initial structure of mPlum with crystallographic water molecules was solvated by

using the *solvate* plugin in VMD. For all mutants, the box cutoff was set to 10 Å. For mPlum, this resulted in a simulation box of dimensions 65.1 x 62.6 x 71.7 $Å^3$, with similar dimensions for the other mutants. The solvated system was electrically neutralized by adding five Na+ ions randomly in the bulk water using the VMD autoionize plugin. The final system contained a total of 27188 atoms. All water molecules overlapping with the protein were removed. The particle mesh Ewald method was used to treat long-range interactions with a 12 Å nonbonded cutoff[157]. Energy minimization was performed using the conjugate gradient and line search algorithm. The system was then heated for 90 ps with a linear gradient of 20K/6ps from 20 to 300 K. At 300 K, the system was equilibrated for 910 ps with a 2 fs integration time step in the NVT (constant number, volume, and temperature) ensemble. Langevin dynamics was used to maintain the temperature at 300 K. The production run was 50 ns using NVT dynamics with 2 fs time steps. The last 40 ns of the production run was used for analysis.

3.3 Results

Steady State Spectroscopy

Linear absorption and emission peaks for each mutant are shown in Table 3.2. The absorption peaks fall within a narrow range around 590 nm aside from E16L, E16H, and I65L, which exhibit ~5 nm blue and red shifts respectively. The Stokes shifts range from 1600 cm^{-1} and 778 cm^{-1} with mPlum and E16L being the largest and smallest respectively.

Table 3.2. Steady state absorption and emission data for each mutant.

Mutant	Absorption Peak (nm)	Emission Peak (nm)	Stokes Shift (cm^{-1})
mPlum	589	648	1593
E16Q	588	630	1134
E16H	586	620	936
E16L	586	614	778
I65L	596	629	881
I65A	591	630	1047
I65V	591	641	1319

Time-resolved Measurements

To differentiate the solvation dynamics of the variants, the spectral shape and time evolution of the transient grating signals was analyzed. SRTG spectra of mPlum and the I65L for various time slices are displayed in Figure 3.2a. The results for these mutants were plotted to illustrate the range of behavior among all species.

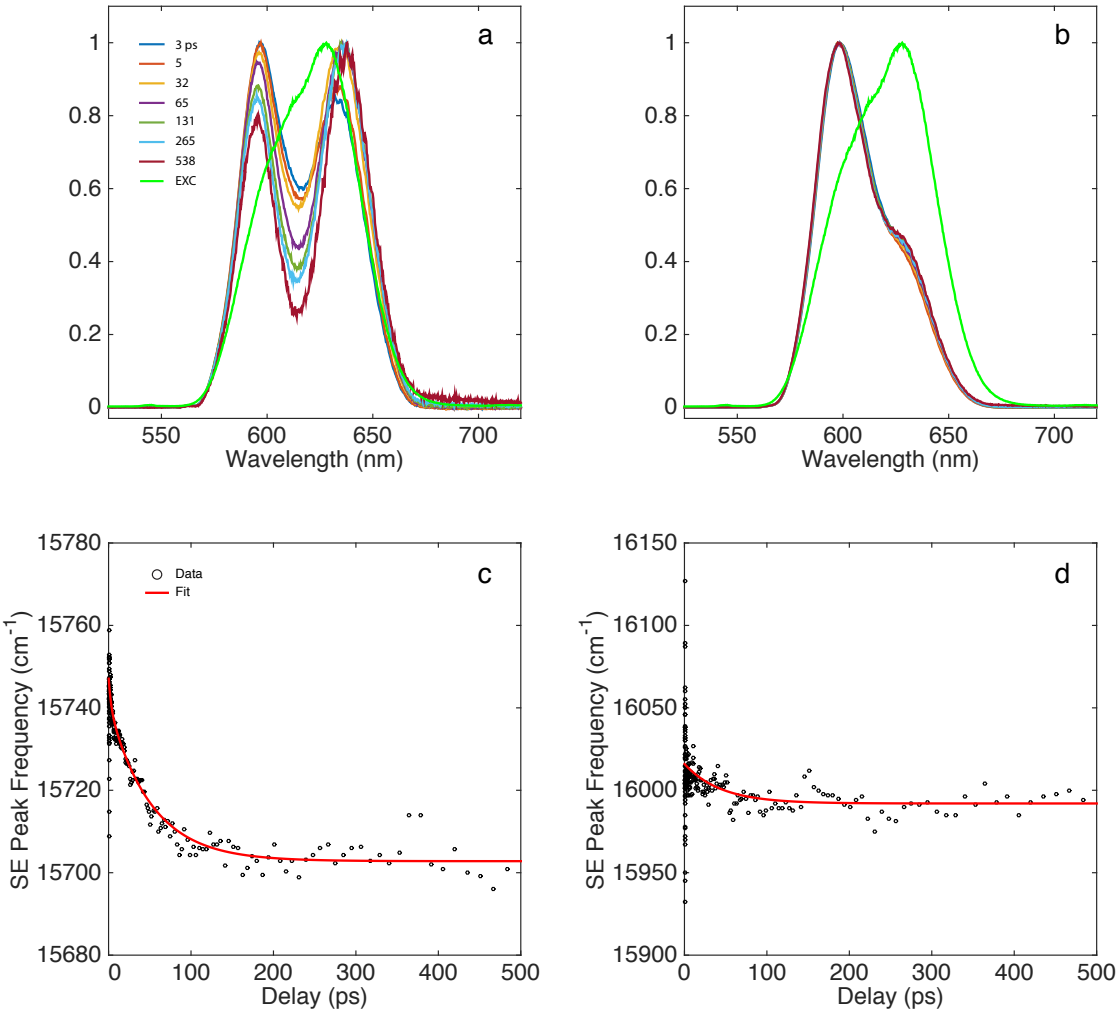

Figure 3.2. Spectrally-resolved transient grating data for (a) mPlum and the (b) I65L mutant with excitation spectrum (EXC) overlaid. Center peak positions for the SE band obtained from transient grating data for (c) mPlum and the (c) I65L mutant (black circles). A best-fit curve derived from nonlinear least squares fitting is overlaid (solid red line).

In each case, we observed two distinct bands corresponding to the GSB (high energy) and SE (low energy) responses. The absence of signal between bands for mPlum and on the red extreme for I65L suggests a strong excited state absorption (ESA). To test this effect, we evaluated our signal in the case of infinite delay. For a heterodyne detected signal (*e.g.* transient absorption), one would expect the signal

spectrum upon complete relaxation to reflect the excitation-weighted sum of steady state absorption and emission. To account for this discrepancy in this homodyne experiment, the SRTG data was divided by the probe intensity spectrum as explained previously by Lee and coworkers[152]. This test confirms the presence of ESA to the red of ω_{eg}, likely overlapping the SE band. Furthermore, the transient absorption spectrum of mPlum also shows a negative band located at wavelengths both red-shifted and blue-shifted of the GSB indicative of ESA. We assume the ESA does not spectrally evolve on the experimental timescale.

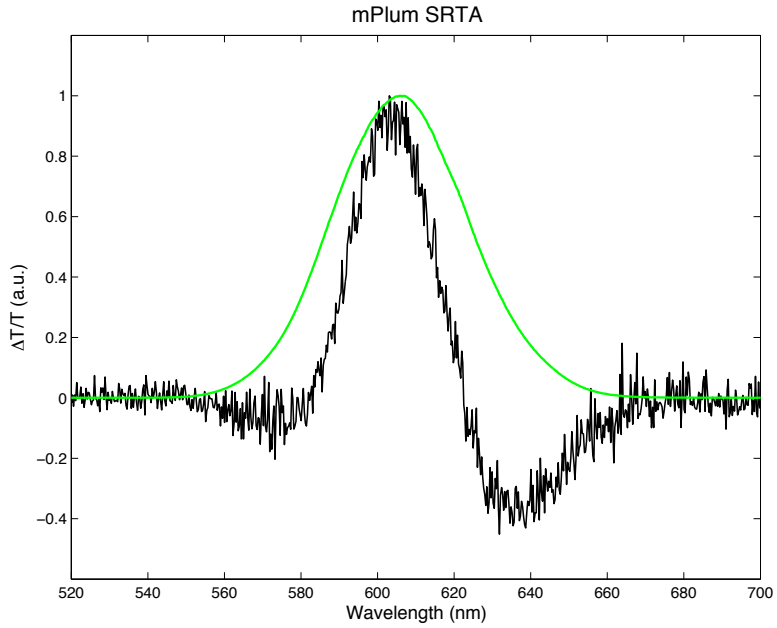

Figure 3.3. Spectrally-resolved transient absorption spectrum of mPlum (black) with excitation overlaid (green). Negative features bounding the positive bleach signal reflect the presence of multiple excited state absorption (ESA) contributions.

Transient grating spectra at each time increment were fit to a sum of two Gaussians and the center positions of each band were subsequently fit to a multiexponential decay. Data at early and later delays were omitted due to finite pulse effects and poor signal-to-noise, respectively. SE peak positions and fits for

mPlum and I65L are displayed in Figure 3.2b and the remaining mutants are shown in Figure 3.4.

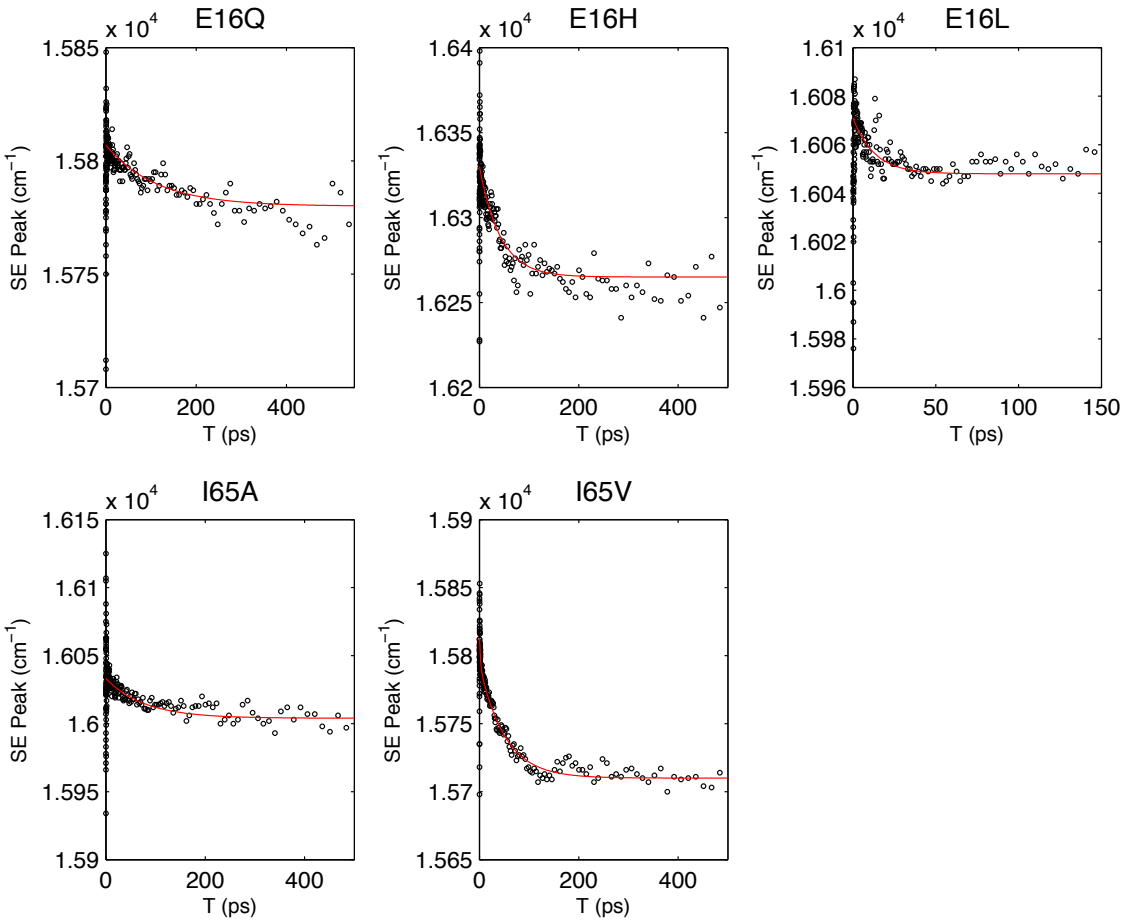

Figure 3.4. Stimulated emission (SE) peak positions for mPlum mutants (black circles). A best-fit curve derived from nonlinear least squares fitting is overlaid (solid red line).

The fitting results and associated error analysis are presented in Tables 3.3 and 3.4.

Table 3.3. Summary of SRTG fitting results following fitting the raw data to a sum of two Gaussians.

Mutant	SE Red Shift		GSB Blue Shift	
	Tau (ps)	Shift Magnitude (cm^{-1})	Tau (ps)	Shift Magnitude (cm^{-1})
mPlum	3	17	--	--
	51	95	58	46
E16Q	107	26	86	21
E16H	49	69	--	--
E16L	13	23	34	7
I65L	44	24	237	19
I65A	--	--	9	16
	100	37	173	29
I65V	2	19	19	13
	51	84	142	18

Table 3.4. Fitting error analysis for multiexponential fits to SE band shifts. The given values represent 95% confidence intervals for the parameters of the fit equation: $f(t) = a \cdot e^{-bt} + c \cdot e^{-dt}$. Amplitudes are expressed in wavenumbers (cm^{-1}) and time constants are reported as e^{-1} lifetimes in picoseconds.

Mutant	a (cm^{-1})		b (ps)		c (cm^{-1})		d (ps)	
mPlum	11.1	22.1	2	14	89.4	100.5	46	57
E16Q	24.5	26.6	93	128	--	--	--	--
E16H	67.3	71.6	44	54	--	--	--	--
E16L	20.2	24.8	10	18	--	--	--	--
I65L	20.7	28.0	27	120	--	--	--	--
I65A	27.4	31.2	62	103	--	--	--	--
I65V	12.5	25.6	1	17	77.6	89.4	45	60

The solvation responses can be categorized in terms of either timescale or amplitude. Timescales ranged from around a hundred ps (E16Q, I65A), tens of ps (mPlum, E16H, E16L, I65L), and a few ps (mPlum, I65V). It should be noted that the mPlum time constants of 3 and 51 ps are consistent with those measured with fluorescence upconversion by Abbyad *et al.* (4.3 and 71 ps)[45]. The shift magnitudes fell into two groups: 22-37 cm^{-1} (E16Q, E16L, I65L, I65A) and 65-112 cm^{-1} (mPlum,

I65V, E16H). The mutants with the largest Stokes shifts (mPlum, I65V) have multiple timescales of relaxation. The remaining show only a single timescale of tens of ps. Longer decay times cannot be ruled out given the 500 ps experimental time window. Timescales of the GSB component are in qualitative agreement suggesting similar ground and excited state dynamics in accordance with a linear response. The magnitudes of the spectral shifts in all cases are smaller than observed by Abbyad *et al.* (793 cm^{-1}). In principle, this can be attributed to either inadequate time or spectral resolution. The former is unlikely since the time resolution in the previous study was on the order of 100s of fs, whereas SRTG was performed with 20 fs excitation pulses. On the other hand, reductions in the measured spectral shifts are inevitable given a finite excitation bandwidth of approximately 1000 cm^{-1} along with an overlapping ESA.

The SRTG response was modeled to reconcile the disparity in shift magnitude between these measurements and upconversion spectroscopy. We consider the influence of a finite laser bandwidth and ESA on the SE band position. For three electronic levels, there are three possible resonant time ordered contributions to the third order optical response to consider for this experimental phase-matching direction[158]. To simplify fitting, the GSB response was omitted. This simplification will not affect the results since this band is blue-shifted relative to the SE band. An initial center position of 16178 cm^{-1} was chosen for the SE component with an asymmetric Gaussian shape replicating the steady state emission spectrum. The excitation pulse center and width mimicked that used in the experiment (16000 cm^{-1}, 1025 cm^{-1}). An asymmetric Gaussian with a shape closely matched to the ground

state absorption spectra was used to model ESA. The intensity of the ESA transition was assumed equal to 0.4 of the GSB consistent and centered at 16667 cm^{-1}, consistent with the transient absorption spectrum. The SE and ESA signal responses were added according to the signs of their respective optical responses. A red shift was assumed to follow the measured upconversion time constants and shift magnitudes for mPlum of 4.3 (301 cm^{-1}) and 71 ps (492 cm^{-1}). Figure 3.5 illustrates the modeled data with and without application of a finite excitation bandwidth and ESA. Inclusion of these effects yields a total shift magnitude of 137 cm^{-1}, in close agreement with our experimentally measured value. Moreover, the shift time constants of 5 and 72 ps for the filtered signal closely match the inputted values. By proportionally decreasing the shift magnitude relative to mPlum in Table 3.2, we also find the calculated shift magnitudes similarly agree with the experimental values for the mutants. This analysis demonstrates that accounting for a finite excitation bandwidth and ESA explains the decreased shift magnitudes relative to upconversion spectroscopy and that SRTG is sensitive to the underlying constants of the excited state reorganization.

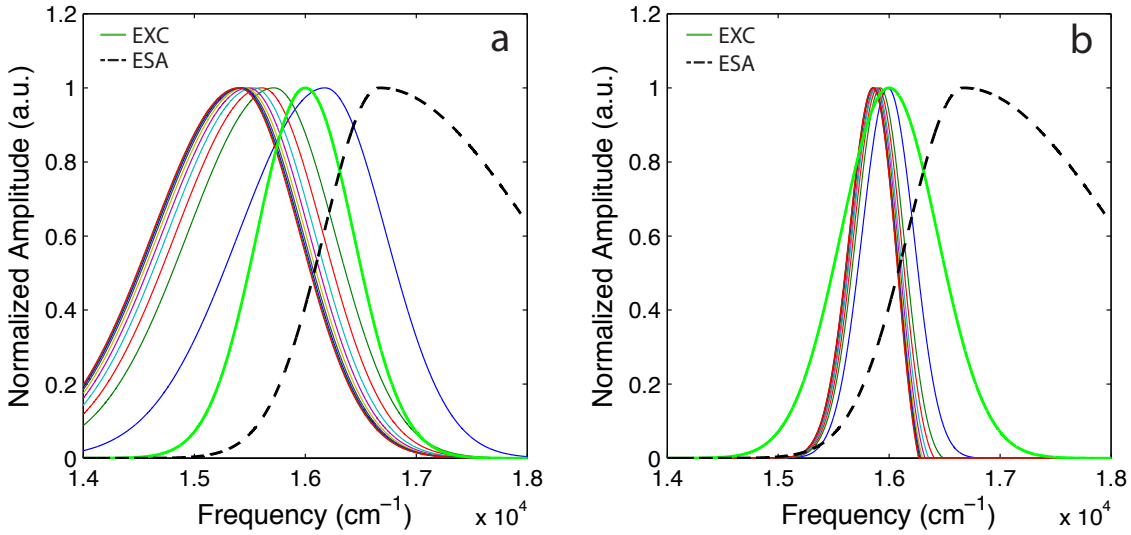

Figure 3.5. Simulated SRTG data with and without application of a finite excitation bandwidth (EXC) and ESA response. (a) Hypothetical SRTG data without excitation filter and ESA. (b) With excitation filter and ESA.

The amplitude decays of each band reveal predictable photophysical behavior (Table 3.5).

Table 3.5. SRTG amplitude decays of GSB and SE bands.

Mutant	GSB		SE	
	Tau (ps)	Amplitude	Tau (ps)	Amplitude
mPlum	22	0.29	52	0.21
	325	0.71	434	0.79
E16Q	98	0.30	152	0.22
	498	0.67	533	0.78
E16H	443	1.00	422	1.00
E16L	58	0.13	494	0.99
	549	0.85	--	--
I65L	445	0.97	211	0.26
	--	--	581	0.71
I65A	266	0.10	384	0.87
	437	0.84	--	--
I65V	19	0.16	19	0.10
	360	0.81	394	0.90

In the case of SE, the dominant component closely matches the measured excited state lifetime of 800 ps for mPlum after correcting twofold due to the effect of homodyne detection[45]. In some mutants, minor contributions exist on both shorter and longer timescales consistent with complex photophysics known to RFPs. The GSB band intensity decay reflects the ground state recovery process, which is expected to follow both directly from the excited state, or more slowly from a third level, as RFPs are known to undergo varying degrees of dark state conversion with repopulation occurring on microsecond and longer timescales[146,159]. This effect would yield a disparity between rates of ground state repopulation and excited state depopulation. The amplitude decays are also slightly influenced by bands shifting within the finite laser bandwidth. We will not further consider the GSB recovery timescales, but instead focus on the excited state dynamics revealed by the timescales of SE band shifts.

Molecular Dynamics Simulations

MD trajectories of each mutant were used to examine the chromophore flexibility and the interconversion between hydrogen bond states. First we examined the dynamics of the interaction between positions 16 and 65 in mPlum and found two distinct conformations, displayed in Figure 3.6. The important difference between Figure 3.6 (a) and (b) is the hydroxyl group orientation (OE2 and HE2 in the CHARMM file) of E16. In Figure 3.6a, the OH group is positioned so that it can make a direct hydrogen bond with I65, whereas in Figure 3.6b, it reorients to accommodate a water-mediated hydrogen bond. The simulations

reveal the presence of approximately 5 water molecules within 3 Å of the chromophore for all mutants (Figure 3.7).

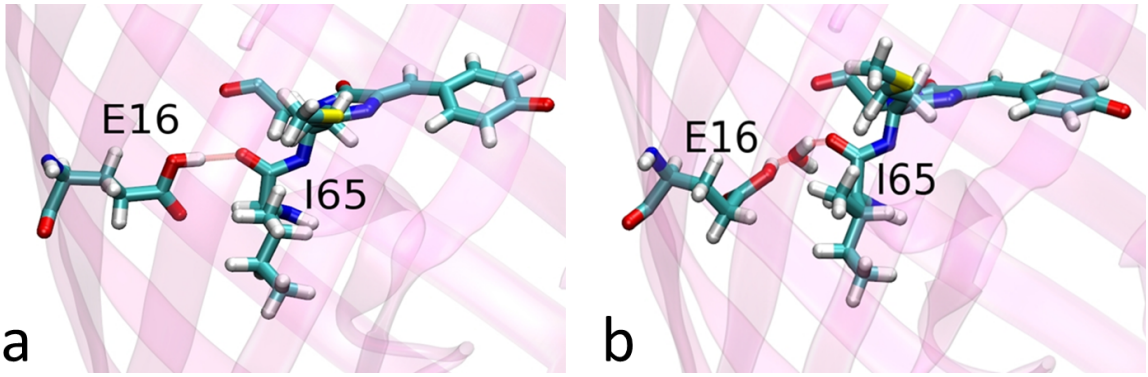

Figure 3.6. Unique 16-65 hydrogen bond conformations identified in MD simulations of mPlum. (a) The E16 hydroxyl group orientation provides a small enough separation from I65 to allow a direct hydrogen bond. (b) The E16 hydroxyl group orientation results in a larger separation from I65 and a water-mediated hydrogen bond.

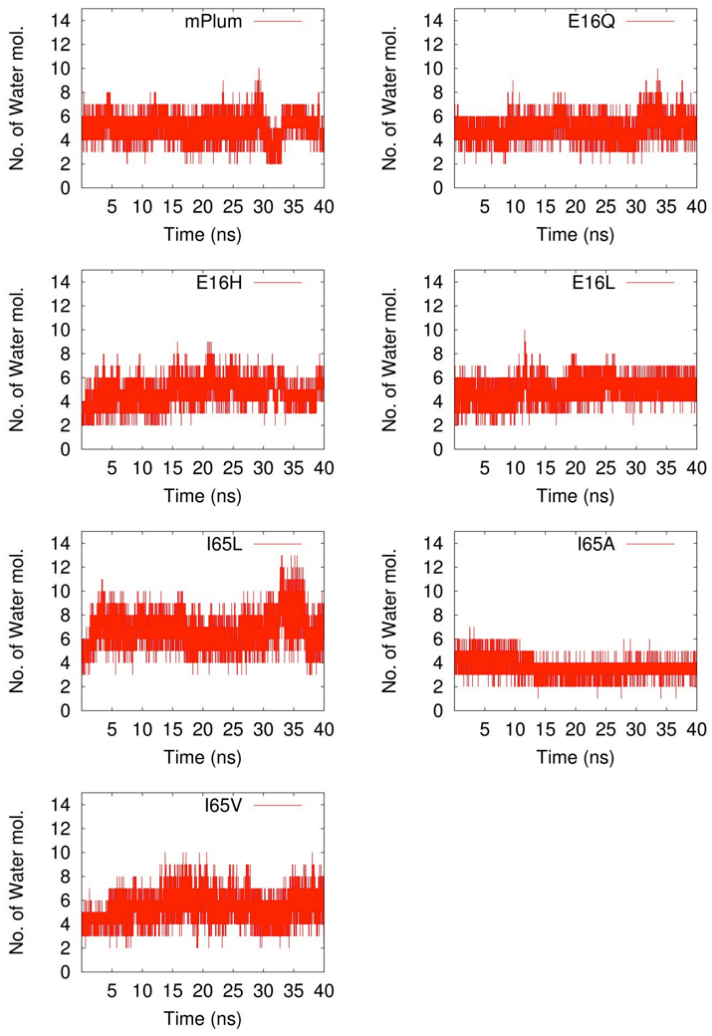

Figure 3.7. Water occupancy within 3 Å of chromophore over a 40 ns time trajectory for mPlum and variants.

In the mPlum variants, we found that some can also form two distinct 16-65 hydrogen bonds (E16Q, I65V), whereas other mutants can only form one type of hydrogen bond (I65A, I65L, E16H) or none at all (E16L). Figure 3.8 presents times series trajectories from MD simulations from 0-40 ns. The relative 16-65 positioning is expressed as Δr, and is defined as the distance between the participating atom in the 16 sidechain and the N-acylimine oxygen of residue 65.

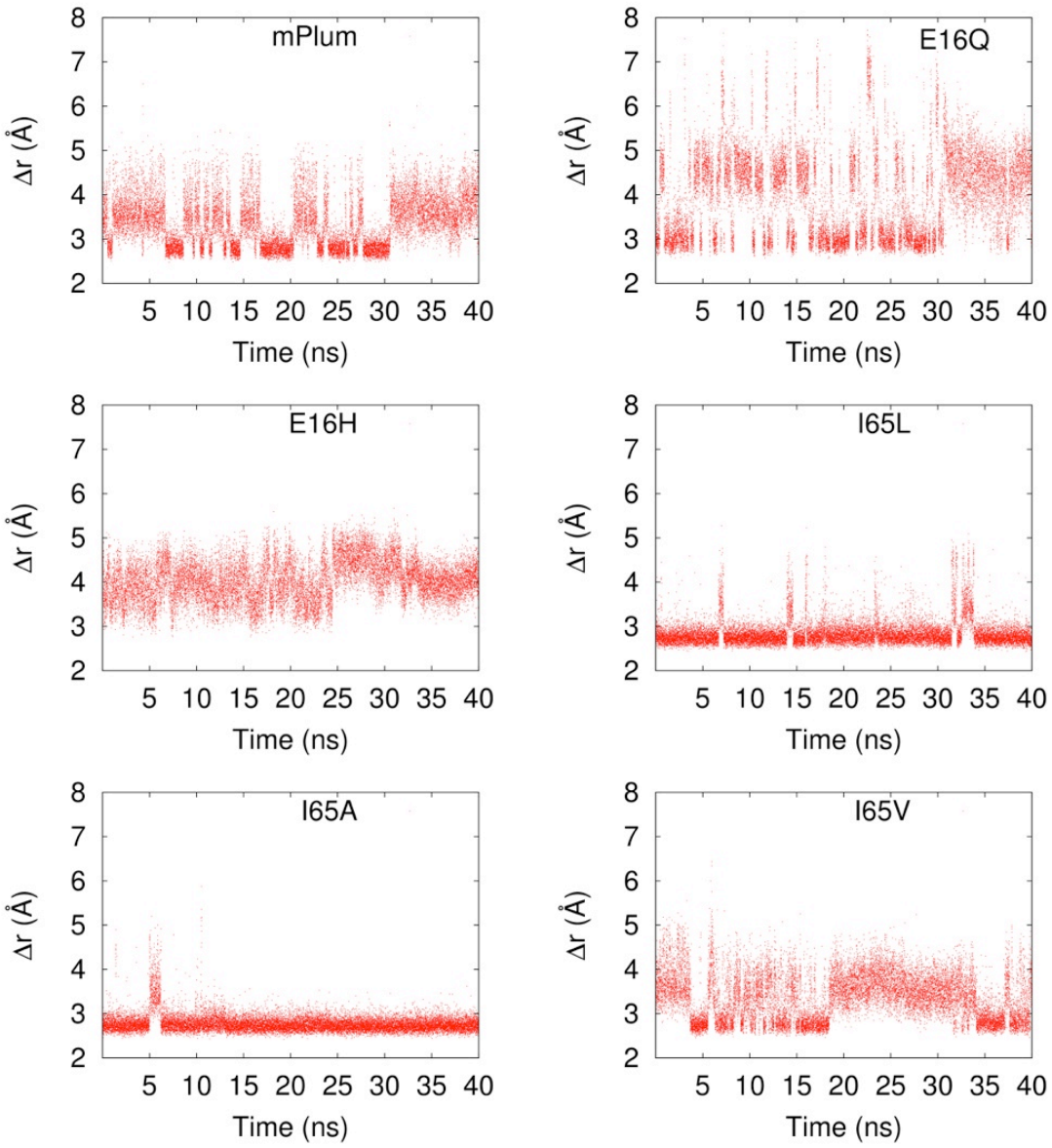

Figure 3.8. MD time series trajectories for all mPlum mutants. Δr refers to the distance between the sidechain of 16 and the N-acylimine oxygen of I65.

The capability to switch between substates is correlated with Stokes shift. For the three proteins with the largest Stokes shift, mPlum, E16Q, and I65V, there are distinct, ns-timescale periods in which the separation is characteristic of relatively stable direct hydrogen bonds (<3.5 Å), as well as switching to distinct periods in which the separation is characteristic of water-mediated hydrogen bonds

(>4 Å). This is reflected in the first two columns of Table 3.4, which shows that for these proteins, conformational interconversion allows each type of hydrogen bond to occur for a significant fraction of the MD simulation. For the other four mutants, with smaller Stokes shifts, the time series trajectories of Figure 3.8 do not reveal conversion between two relatively stable types of hydrogen bonds. Mutants I65L and I65A spend most of their trajectories in a direct hydrogen bond, while E16H fluctuates primarily within the water-mediated hydrogen bond conformation. Finally, the E16L variant cannot form a stable hydrogen bond of either variety due to its aliphatic nature and hence, exhibits random fluctuations throughout the trajectory.

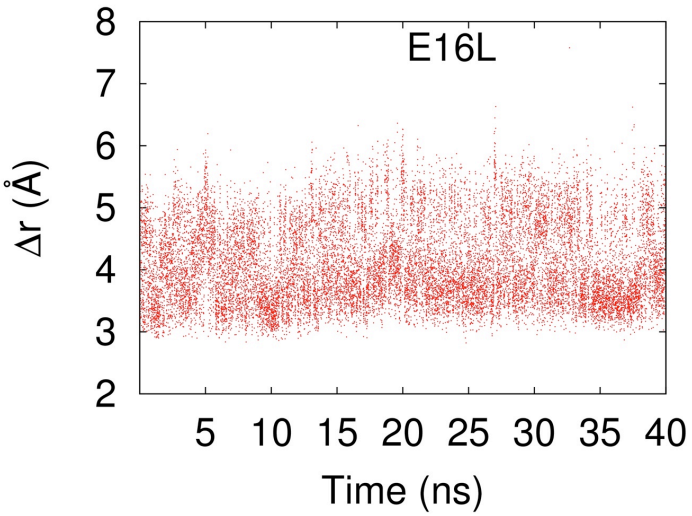

Figure 3.9. MD time series trajectory for the mPlum E16L mutant. Δr refers to the distance between the L16 sidechain and the N-acylimine oxygen of I65.

The 16-15 distance for E16Q shows an additional substate with Δr ~ 6.5 Å, caused by a unique rotation of Q16. A histogram of the 16-65 distance Δ r for each FP

similarly reveals the presence of these distinct hydrogen bond configurations described above (Figure 3.10).

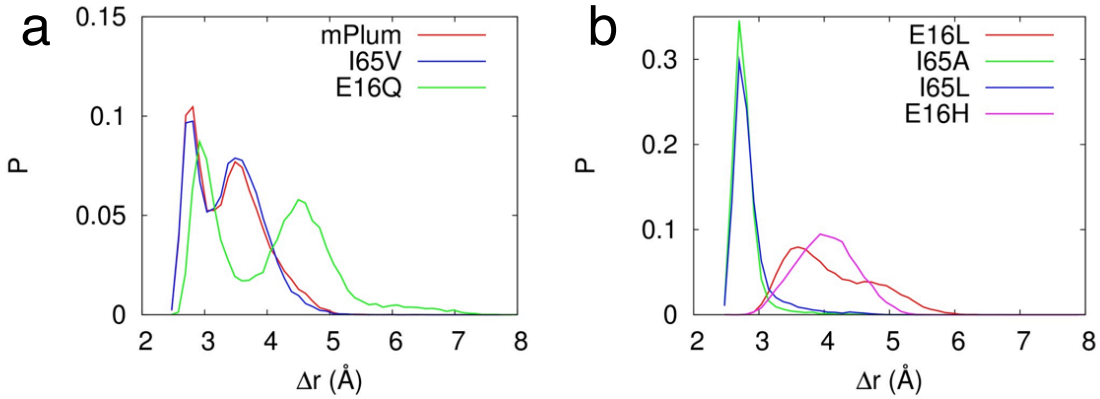

Figure 3.10. Histograms of the probability for a 16-65 separation, Δr, to occur during the MD simulations. (a) The three mutants with the largest Stokes shift show two distinct, stable configurations, corresponding to Δr characteristic of a direct hydrogen bond as well as a larger Δr characteristic of a water-mediated hydrogen bond. (b) The four mutants with the smaller Stokes shift display a single peak implying little or no fluctuations in 16-65 hydrogen bond.

Table 3.6. Survival times calculated for the direct hydrogen bond molecular configuration and for the water-mediated hydrogen bond configurations following two hydrogen bond criteria. The survival times listed are obtained from the single exponential fits to the time correlation function. Calculation of survival times was not possible for cases with negligible hydrogen bond percentage. Survival times are given using two different sets of criteria for determining hydrogen bonds (angle cut-off of 30° versus 40° in VMD).

Mutant	Survival Time (ps) 3.5 Å/30°		Survival Time (ps) 3.5 Å/40°	
	Direct	H_2O mediated	Direct	H_2O mediated
mPlum	10	2	29	4
E16Q	3	2	5	3
E16H	--	2	--	4
E16L	--	--	--	--
I65L	13	--	44	--
I65A	29	--	167	--
I65V	8	2	17	3

We next analyzed the MD results to determine if the lifetimes of the various hydrogen bond configurations are consistent with their characteristic experimental timescales. Simulations were carried out for time intervals long enough to ensure exhaustive sampling of all molecular subconformations[160]. We extracted hydrogen bond survival times from the simulations by calculating the hydrogen bond survival function in the direct substate, and separately in the water-mediated substate. The survival function gives the conditional probability that a hydrogen bond intact at time t_{i-1} will also remain intact at time t_i and is given by $p(t) = 1 - f(t)$, where $f(t)$ is the fraction of hydrogen bonds broken at time t. The average survival time was estimated by fitting the survival function to an exponential: $p(t) \sim \exp(-t/\tau)$ [161]. The survival time functions show decays on a few ps and tens of ps timescales for most mutants.

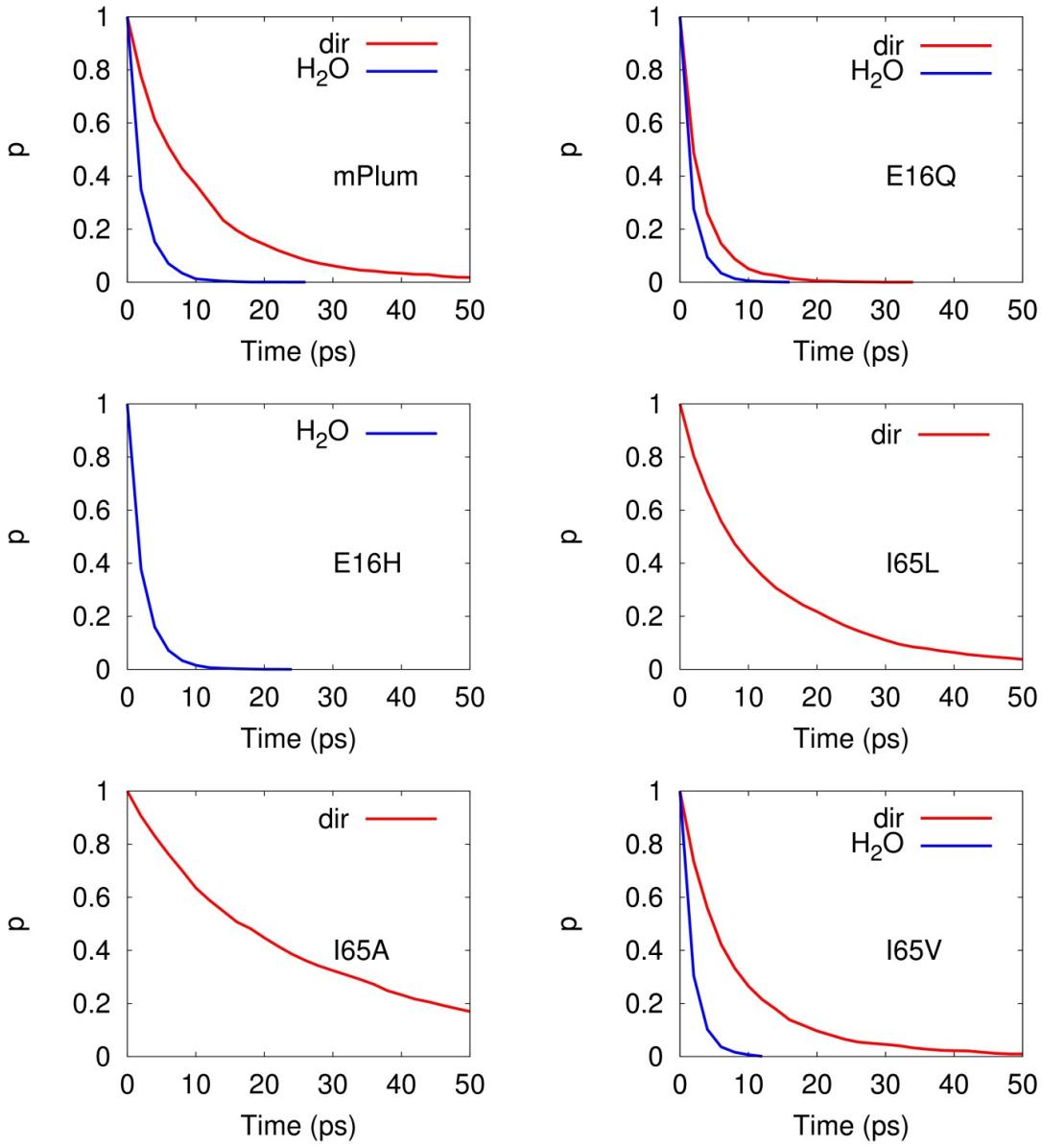

Figure 3.11. Survival functions calculated from the MD simulations for the direct and water-mediated hydrogen bonds (3.5 Å/30° cut-off).

Both sets of decays show qualitative agreement with the experimental time constants shown in Table 3.6, with the 30° criteria being proportionally shorter for the direct hydrogen bond. For variants with significant populations in both substates, it is observed that direct hydrogen bonds survive for much longer times than do the water-mediated hydrogen bonds. This implies that the shorter

experimental time constants may be due to 16-65 water-mediated hydrogen bond dynamics, whereas the longer experimental time constants may be due to 16-65 direct hydrogen bond dynamics. If the percentage of a type of hydrogen bond is very small, we are not able to calculate survival times, which might explain why mutants of smaller Stokes shift have only one experimentally observed time constant. In general, the biggest disagreements fall among the E16 mutants. The absence of shorter time component in E16Q is likely a result of poor signal-to-noise given its comparably smaller shift magnitude. A strong ESA overlap with the SE band would have an effect similar to a finite excitation bandwidth mentioned above in that it would decrease the magnitudes of the spectral shifts. The longer time constant observed in this mutant can be explained in terms of a unique rotation of Q16 with a calculated correlation time of 91 ps, which closely matches the experimental value of 112 ps. For E16L and E16H, the origin of this discrepancy is less obvious, although we find an elevated chance of a water-I65 hydrogen bond (without a simultaneous water-16 hydrogen bond) in these mutants (Table 3.7).

Table 3.7. Probability of I65-water hydrogen bond without a simultaneous 16-water hydrogen bond from the MD simulation for each mutant.

Mutant	H_20-I65 (%)
mPlum	12.8
E16Q	30.5
E16H	30.8
E16L	49.1
I65L	13.1
I65A	3.4
I65V	32.6

The survival time of this hydrogen bond is only a few picoseconds, and therefore the observed relaxation is clearly not the result of the dynamics of this bond. It is possible that water motion in this region near the chromophore could facilitate solvation on the timescales observed. In general, the mutations at position 16 yield less predictable responses than those at position 65, probably because these mutations replace a charged side chain with uncharged, polar or nonpolar sidechains, which are likely induce greater electrostatic perturbation of the chromophore environment versus the position 65 mutations. Further analysis will require quantum mechanical calculations.

To connect the dynamics observed in the MD trajectories with Stokes shift, we examined the influence of the 16-65 interaction on hydrogen bonds made to the chromophore with the surrounding environment. In particular, interactions with S146, R95, E215, and Q109 are known to be important for spectral tuning in other green and red FPs[11]. Table 3.8 summarizes this analysis. The first two columns show the fraction of time spent hydrogen-bonded, direct or water-mediated, at positions 16 and 65. The remaining columns tabulate the time a chromophore-sidechain hydrogen bond occurs, partitioned by 16-65 substate, and normalized by its respective occupancy. Residue 65 is considered to be part of the extended chromophore and therefore hydrogen bonding with 65 can directly influence the chromophore environment[10]. Chromophore-hydrogen bond interactions at other sidechains appear independent of whether there is a direct or water-mediated interaction at 16-65. We conclude that 16-65 switching constitutes the largest

observable structural change within the chromophore environment and must be integral for the bathochromic shift observed in mPlum.

Table 3.8. Hydrogen bonds to chromophore from neighboring sidechains are presented in terms of time fraction as calculated from MD simulations. For each mutant, bonds with sidechains S146, R95, E215, and Q109 are reported for each 16-65 substate, direct and H_2O-mediated, normalized by their respective occupancy. For all entries, 3.5 Å distance and 30° angle cut-off values were used for determining the hydrogen bonds.

Mutant	16-65 H-Bond (%)		S146-CRO (%)		R95-CRO (%)		E215-CRO (%)		Q109-CRO (%)	
	Direct	H_2O mediated	Direct	H_2O mediated	Direct	H_2O mediated	Direct	H_2O mediated	Direct	H_2O mediated
mPlum	31.3	18.4	72.8	49.9	88.9	89.7	82.3	79.6	38.7	10.9
E16Q	18.4	14.3	80.6	85.9	93.4	95.1	79.3	80.1	43.6	58.5
E16H	0.0	25.2	85.7	43.6	85.7	87.2	71.4	80.9	28.6	6.2
E16L	0.3	0.2	84.0	93.0	94.0	84.0	74.5	66.6	20.3	26.7
I65L	76.8	0.0	3.0	0.0	85.8	83.3	86.5	83.3	34.9	50.0
I65A	89.9	0.5	83.5	95.6	91.9	89.1	86.4	86.9	58.7	45.7
I65V	28.2	14.8	27.6	38.9	64.9	66.6	82.2	81.8	11.1	6.3

The chromophore flexibility was analyzed by extracting a root mean square fluctuation (RMSF) on an atomic basis from the MD simulations. We observe no correlation between chromophore flexibility and Stokes shift among these mutants (Figure 3.12).

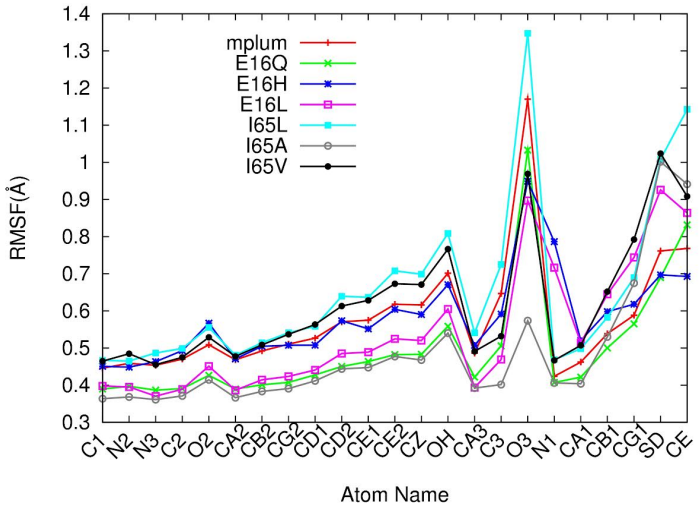

Figure 3.12. Calculated chromophore RMSF for each mutant.

3.4 Discussion

The time dependent shifts of the SE band observed in SRTG measurements are directly related to the relaxation of the excited state energy leading to the Stokes shift of the steady state emission spectrum. Classical MD simulations are not capable of estimating the magnitude of electronic energy relaxation since they only model dynamics on the ground electronic state. However, within linear response theory, these dynamics approximate motions leading to excited state solvation and thus, serve as a means of modeling the effect of variations in chromophore-environment interactions on molecular dynamics and their timescales[162]. These results provide new insight into the dynamics of the interaction between the 16 and 65 sidechains in mPlum and an explanation for its large Stokes shift relative to other DsRed-derived FPs. These conclusions follow from two key observations. First, the two timescales observed experimentally and in the simulations represent survival times of direct and water-mediated hydrogen bond substates between the 16 and

65 sidechains. Second, there is a direct correlation between the Stokes shift of each mutant and to the extent to which it undergoes hydrogen bond interconversion. Cases in which no direct hydrogen bond is possible (E16L, E16H) or where a direct hydrogen bond forms almost exclusively (I65L, I65A) show the smallest Stokes shifts of mutants tested. Conversely, species with the greatest propensity to interconvert between hydrogen bond states (mPlum, E16Q, and I65V) have the largest Stokes shift. This dynamic model of the chromophore solvation stands in contrast with previous studies of mPlum mentioned above, which primarily attributed its red-shifted emission to stabilization of the excited state through a direct hydrogen bond between E16 and the N-acylimine oxygen of I65.

The influence of confined water molecules on the solvation of probes buried within protein environments following photoexcitation has brought about intense debate[163,164]. In particular, it is questioned whether confined water or protein sidechains are responsible for the slow (relative to bulk water) ps solvation observed in these environments. For GFP, Xu and coworkers found 10 water molecules in close vicinity to the chromophore with predicted solvation dynamics timescales ranging from tens of fs to several hundred ps[165]. While the simulations indicate a similar presence of water, it is unlikely that these solvent molecules are responsible for the variation in dynamics. First, we observe similar water occupancy among all variants indicating any contribution is likely consistent regardless of mutation (Figure 3.7). Moreover, we do not observe the slowest 333 ps time constant predicted by Xu *et al.* in any sample. It is possible that the anomalous responses of the E16 mutants, noted above, is related to a water-I65

hydrogen bond not observed in the I65 variants. These observations suggest water may play a minor role in the observable dynamic Stokes shift, but the dominant response is governed by internal hydrogen bond dynamics as reflected by the above survival time calculations for most species.

It is clear that the presence of neither a direct or water-mediated hydrogen bond is the sole determinant of a large Stokes shift. It is possible that the 16-65 interaction modulates chromophore flexibility. Flexibility about the methylidene bridge would disrupt coplanarity between the imidazole and phenoxy moieties, inhibit electron delocalization, and lead to a smaller Stokes shift[19, 47]. A similar effect was proposed in quantum mechanical simulations of DsRed where a noted torsion of the terminal carbonyl of I65 leads to a blue shift due to loss of conjugation as observed in mOrange[11, 148]. It is plausible hydrogen bonding to this position serves as an anchor that preserves coplanarity either at the carbonyl or more broadly across the ring system. Among the series of mutants, this may be manifest in slightly different ways given the precise nature of the 16-65 interaction. These can be broken down into four cases: 1. forms no hydrogen bond (E16L), 2. forms a direct hydrogen bond (I65A, I65L), 3. forms a water-mediated hydrogen bond (E16H), 4. demonstrates interconversion between multiple hydrogen bond states (mPlum, E16Q, I65V). Assuming E16L as a baseline, those with a single interaction (I65A, I65L, and E16H) represent the middle grouping of observed Stokes shifts, whereas those in the fourth category (mPlum, E16Q, I65V) hold the largest Stokes shifts. The influence of switching is less obvious, but it may be true that, on average, coplanarity is higher among those interconverting between conformations.

Alternatively, the most coplanar configuration (local energetic minimum) may lie along the switching coordinate and remain unpopulated by those not able to interconvert. Lastly, switching between states may act to suppress flexibility of the chromophore in dimensions other than ring torsion, which would also help drive stabilization of the excited state. It is interesting to note that of the I65 mutants, only the valine derivative undergoes hydrogen bond switching, while I65A and I65L demonstrate more rigid conformations. We suggest this may be a steric effect and possibly essential to controlling hydrogen bond interconversion.

Chromophore-sidechain hydrogen bonding interactions are observed in crystal structures of mCherry, mStrawberry, mNeptune, mRojoA, mRouge, eqFP650, and eqFP670[11, 18, 47, 49]. These findings highlight the importance of the dynamics, not the mere presence of these interactions, and suggest that Stokes shift is related to the capability of interconversion between multiple hydrogen-bonded states. It seems reasonable to hypothesize that this behavior scales with the number of weak, interconvertible chromophore hydrogen bond interactions. Consistent with this idea, a recent publication describing the structure and properties of the farthest red emitting FP engineered to date, TagRFP675, which has a 75 nm Stokes shift[50]. They attribute its red emission to several hydrogen bonding contacts involving Q41 and S28 at the N-acylimine position with additional hydrogen bonds at the phenoxy end of the chromophore with N143, N158, and R197.

These results have significant implications in the context of engineering an ideal red fluorescent protein, *i.e.* one with both red-shifted emission and high

quantum yield desired for cellular imaging applications. Previous studies recognized an apparent tradeoff between these properties, with brightness hindered by fast nonradiative deactivation, whereas red-shifted emission results from environmental solvation of the excited state[19]. The implication is that chromophores of the brightest species, with the smallest Stokes shifts, are contained within rigid environments unable to deactivate excitation through thermal fluctuations, phenolic rotation, or cis-trans isomerization, while the reddest emission requires local flexibility to facilitate solvation of the excited state electronic distribution. We hypothesize that the hydrogen bond switching phenomenon observed here acts to selectively tether the chromophore in such a manner that provides a degree of transient flexibility combined with stabilization of the excited state. A similar effect is observed in mNeptune where the guanidinium group of R197 runs parallel along the chromophore and is thought to provide stability across the ring system[47]. This "transient flexibility" may provide a mechanism for simultaneous optimization of these two photophysical properties.

3.5 Conclusions

Time-resolved spectroscopy was carried out on mPlum and a panel of strategic point mutants. The experimental results, supported by MD simulations, provide new insight into the dynamics of the interaction between the 16 and 65 sidechains in mPlum and a possible explanation for its large Stokes shift relative to other DsRed-derived FPs. These conclusions arise following two key observations. First, the two timescales observed experimentally and in the simulations represent interconversion between direct and water-mediated hydrogen bonding substates

between the 16 and 65 sidechains. Second, there is a direct correlation between the Stokes shift of each mutant and to the extent to which it undergoes hydrogen bond interconversion. Cases in which no direct hydrogen bond is possible (E16L, E16H) or where a direct hydrogen bond forms almost exclusively (I65L, I65A) show the smallest Stokes shifts of mutants tested. Conversely, species with the greatest propensity to interconvert between hydrogen bond states (mPlum, E16Q, and I65V) have the largest Stokes shift. This dynamic model of the chromophore stands in contrast with previous studies of mPlum, which primarily attributed its red-shifted emission to direct stabilization of the excited state through a hydrogen bond between E16 and the N-acylimine oxygen of I65. We hypothesize such dynamics facilitate a bathochromic shift through a combination of direct excited state solvation and regulation of chromophore flexibility. This model may provide a guide for further development of highly desirable red-emitting FPs. Moreover, these findings demonstrate the utility of ultrafast spectroscopy in measuring functionally relevant sidechain fluctuations, not typically resolvable with steady state methods.

Chapter IV

The Origin of Extended Stokes Shift of TagRFP675

4.1 Introduction

Modification of the progenitor eqFP578, originally extracted from the sea anemone *Entacmaea quadricolor*, led to the development of a red-emitting monomeric homologue mKate[12]. The near-infrared fluorescent proteins TagRFP675 and TagRFP657 emerged from directed evolution of mKate and represent the reddest-emitting members among all GFP-like FPs reported to date[12, 50, 166]. TagRFP675 exhibits a Stokes shift, which is 30 nm red-shifted comparing to that of its parental protein. Its extended Stokes shift was suggested to be due to an extensive hydrogen-bonding network between the chromophore and its protein matrix. Indeed, as revealed by high-resolution crystal structures of TagRFP675, its DsRed-like chromophore forms multiple direct and water-mediated hydrogen-bonding interactions with the sidechains of S28, Q41, Q106, N143, N158, and R197. In particular, interactions involving the N-acylimine carbonyl of DsRed-like chromophores appear to have a strong influence on excited state properties of FPs[44]. In TagRFP675, the N-acylimine carbonyl forms two hydrogen bonds. One arises from a direct interaction with the Q41 sidechain, while the other stems from an embedded water molecule supported by tertiary interactions with amide group of Q106. These interactions are illustrated in Figure 4.1. A similar motif, formed by side chains of Q41 and T28, is observed in another mKate derivative, mCardinal[167]. This interaction was suggested to provide enhanced excited state stabilization through a stronger direct hydrogen bond interaction[167]. A water-mediated

hydrogen bond between the chromophore and S28 located on the inner wall of the β-barrel was realized in the mCardinal precursor, named mNeptune[47].

We previously investigated a similar interaction between the N-acylimine carbonyl of the chromophore and carboxylate group of the E16 residue in mPlum[45-46]. Utilizing time-resolved spectroscopy and supported by Molecular Dynamics (MD) simulations, we discovered that red-shifted emission correlates not with hydrogen bond strength, but a facile switching between direct and water-mediated hydrogen bond conformers[168]. This model suggests that localized flexibility may be important to excited state stabilization.

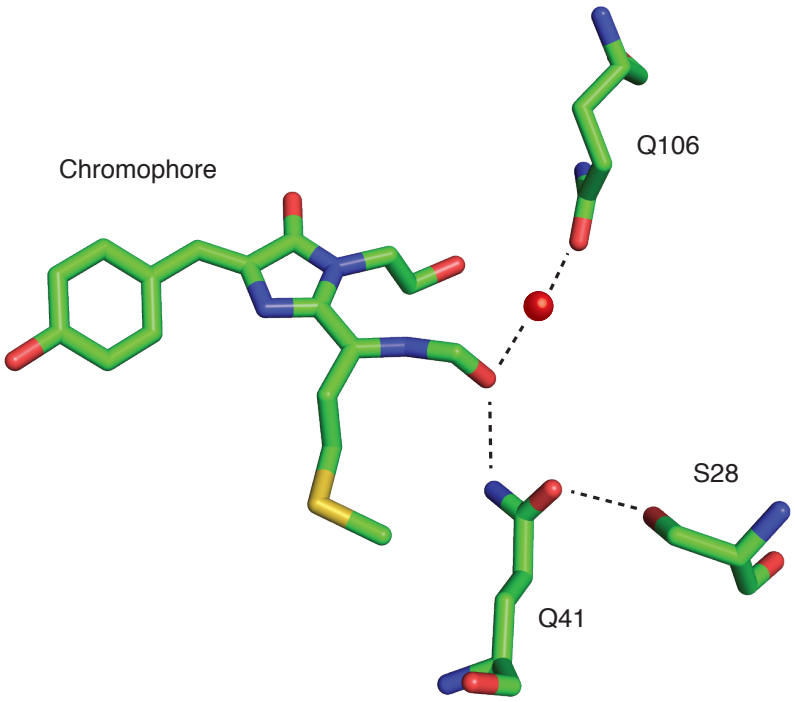

Figure 4.1. The hydrogen bond interactions between the N-acylimine oxygen of the DsRed-like chromophore, S28, Q41, Q106 side chains and water molecule identified in the crystal structure of TagRFP675 (pdb code 4KGF). Hydrogen bonds are represented as dashed black lines; atoms are colored by atom type; water molecule is shown as red sphere.

The molecular response in the condensed phase can be probed with time-resolved electronic spectroscopy. The excited chromophore is coupled to stochastic fluctuations of the surrounding bath with a spectral density spanning an extraordinary wide frequency range encompassing ultrafast sidechain motions, intramolecular vibrations, or tertiary interactions to much slower global structural rearrangements (>100s of ps) or even discrete conformational states (isomers)[59]. Such dynamics lead to time-dependent changes in the electronic energy gap that are resolvable with a variety of nonlinear techniques.

In this study, the origin of Stokes shift was explored along a lineage from mKate to TagRFP675. Site-directed mutagenesis enables targeting of specific sidechain interactions that are thought to facilitate excited state stabilization of the chromophore. A panel of mutants was devised to probe the hydrogen bond network surrounding the N-acylimine end of the chromophore. Crystal structures reveal two unique interactions, water-mediated and direct hydrogen bonds, with the F62 carbonyl as illustrated in Figure 4.1. The Q106 sidechain and an embedded water molecule compose the former, while the latter is an interaction with the carboxylic acid moiety of the Q41 sidechain. Three mutants were designed to investigate the water-mediated hydrogen bond: Q106M, F62A, and Q106M F62A. It is predicted that these changes will effectively disrupt this interaction and help elucidate its role in excited state stabilization. This hydrogen bond motif is observed in other far-red emitting FPs including mPlum, mNeptune, and mCardinal. Systematic elimination and addition of this interaction to TagRFP675 (TagRFP675 Q41M) and mKate (mKate M41Q) respectively demonstrate its role in extending Stokes shift.

To explore hydrogen bond solvation dynamics, we employed SRTG spectroscopy as previously applied in Chapter III to investigate excited state solvation stemming from the extended hydrogen bond network of the native RFPs and strategic point mutants[168]. Such information will help precisely characterize specific chromophore-sidechain interactions thought to influence their emission properties. MD simulations will be utilized to corroborate the experimental results. These results lend greater insight into the molecular mechanism of Stokes shift in far-red emitting RFPs and offer the opportunity draw a comparison with our previous findings in mPlum. Ultimately, these principles might possibly help guide the engineering of more robust red-emitting species.

4.2 Experimental Methods

Time-Resolved Spectroscopy

Transient grating measurements were performed as previously described in Chapter III with the JILA MONSTR nonlinear optical platform[106, 168]. Upon irradiation with 3 excitation pulses (20 fs, ~10 nJ/beam), the spatially isolated four-wave mixing signal emitted in the prescribed $\mathbf{k_s}=-\mathbf{k_1}+\mathbf{k_2}+\mathbf{k_3}$ phase matching direction. Excitation wavelength was chosen to maximize contrast between ground state bleach and stimulated emission components. The sample was refreshed with a spinning cell to mitigate photobleaching and accumulation of laser-induced photoproducts. Sample concentration and path length were again carefully tuned to avoid aggregation and reabsorption of the nonlinear signal. Concentrations of ~50 μM and a path length of 0.5 mm were used for all samples (OD 0.15 at peak absorption). Spectrally-resolved homodyne detection was carried out with a liquid

N_2-cooled CCD camera. Data was collected as a function of the *T* time delay ($\mathbf{k_1}$ and $\mathbf{k_2}$ temporally overlapped) from a range of 0 to 1.3 ns, spaced logarithmically, with a background spectrum collected at -500 fs delay to eliminate contributions from excitation scatter and spontaneous emission. The baselined spectral data was fit to a sum of two Gaussians using a nonlinear least squares fitting algorithm. SE peak center position and amplitude was extracted at each time delay and fit to multiexponential decays to yield solvation information.

Molecular Dynamics Simulations

Time series trajectories were obtained from explicit solvent, all-atom simulations using the NAMD molecular dynamics package with the CHARMM27 force field[153-154]. The initial X-ray crystallographic structures were obtained from the Protein Data Bank (mKate pdb code 3BXB, TagRFP675 pdb code 4KGF). The mutants studied do not have PDB structures, so we used CHARMM to make the amino acid substitution from the respective parent files. Force field parameters for the mature chromophore were adopted from the anionic GFP chromophore developed by Reuter *et al.* and from CHARMM27 parameters for acylimine nitrogen[155]. Throughout the simulation, the deprotonated anionic form of the chromophore in the ground state was used. In addition, E215 was protonated using a patch.

The VMD package was used to setup the system for simulations[156]. The initial structure with crystallographic water molecules was solvated by using the *solvate* plugin in VMD. For all mutants, the box cutoff was set to 10 Å. This resulted

in a simulation box of dimensions 66 x 72 x 77 $Å^3$, with similar dimensions for the other mutants. The solvated system was electrically neutralized by adding five Na+ ions randomly in the bulk water using the VMD autoionize plugin. The final system contained about 35000 atoms. All water molecules overlapping with the protein were removed. The particle mesh Ewald method was used to treat long-range interactions with a 12 Å nonbonded cutoff[157]. Energy minimization was performed using the conjugate gradient and line search algorithm. The system was then heated for 90 ps with a linear gradient of 20K/6ps from 20 to 300 K. At 300 K, the system was equilibrated for 910 ps with a 2 fs integration time step in the NVT (constant number, volume, and temperature) ensemble. Langevin dynamics was used to maintain the temperature at 300 K. The production run was 50 ns using NVT dynamics with 2 fs time steps. The last 40 ns of the production run was used for analysis

Protein Expression, Mutagenesis, and Purification

Fluorescent proteins were expressed with the pBAD vector containing their corresponding gene. Point mutations were introduced with QuikChange mutagenesis using custom designed primers (IDT). Expression procedures differed slightly for the two primary lineages studied. For mKate and mutants, plasmids were transformed into Top10 *E. coli*, grown to OD_{600}=0.6 at 37 °C, followed by induction with 0.02% arabinose for 24 hours at 30 °C. Plasmids of TagRFP675 and mutants were transformed into the LMG194 *E. coli* strain, grown to OD_{600}=0.6 at 37 °C, followed by induction with 0.02% arabinose for 48 hours at 18 °C. Samples

were purified via 6X-His tag/Ni-NTA chromatography and the crude specimens were buffer-exchanged with 15 mM pH 8.0 TRIS buffer, 100 mM KCl. Emission spectra of each mutant were detected with a diode array spectrometer and its peak value helped verify the purity of the final products.

4.3 Results

Steady State Spectroscopy

The linear absorption and emission data are tabulated below. The absorption peaks fall between 585-600 nm as typically observed in other RFPs. The emission values also show systematic trends. Addition of a hydrogen bond at the N-acylimine carbonyl in mKate M41Q leads to an 18 nm red-shifted emission, while its removal in TagRFP675 Q41M has the opposite effect yielding a 32 nm blue-shift relative to the native variant. Disruption of the water-mediated hydrogen bond network also leads to blue-shifted emission in the TagFP675 F62A, Q106M, and F62A Q106M mutants.

Table 4.1. Steady state absorption and emission data for all species.

Mutant	Absorption Peak (nm)	Emission Peak (nm)	Stokes Shift (cm^{-1})	Quantum Yield
mKate	588	635	1259	0.30
mKate M41Q	585	653	1780	--
TagRFP675	600	675	1852	0.08
TagRFP675 F62A	598	658	1525	--
TagRFP675 Q106M	590	648	1517	--
Tag RFP675 F62A Q106M	588	642	1430	--
TagRFP675 Q41M	590	643	1397	0.18

Time-Resolved Spectroscopy

The experimental results for all species are presented in the figures below. First, contour plots illustrating SRTG spectra and fitting results are presented in Figures 4.2-4.4. Ground State Bleach (GSB) and Stimulated Emission (SE) components are resolved in the TagRFP675, TagRFP675 F62A, TagRFP675 Q106M, TagRFP675 F62A Q106M, and mKate M41Q spectra. The SE component is not obvious for mKate and TagRFP675 Q41M. This is presumed to be an effect of a blue-shifted Excited State Absorption (ESA) band leading to greater overlap with the SE component. It is interesting to note that this effect occurs only in variants lacking a hydrogen bond interaction between the 41 sidechain and the N-acylimine carbonyl and suggests it has a role in tuning RFP electronic structure beyond the first singlet excited state.

Numerical fitting results and error analysis are tabulated below in Tables 4.2 and 4.3. In general, these results can be categorized as follows. No solvation is evident for mKate and TagRFP675 Q41M judging by the stationary GSB component and lack of spectral evolution on the low energy side of the SRTG data. All other species show a consistent biexponential decay behavior. The early component is slightly faster for mKate M41Q, TagRFP675 F62A, and TagRFP675 Q106M (4.5-7.1 ps) compared to TagRFP675 and TagRFP675 F62A Q106M (17.5 and 24 ps). The slower component can be divided into three groups: 537 ps (TagRFP675 F62A Q106M), 355-396 ps (TagRFP675, mKate M41Q), and 159-216 ps (TagRFP675 F62A, TagRFP675 Q106M). Ultrafast solvation appears evident in all mutants, but its measurement is hindered by pulse overlap effects apparent within the first ~200 fs.

The shift magnitudes were proportionally larger for the slower timescale in all cases except for TagRFP675 F62A Q106M. This mutant and TagRFP675 Q106M showed the smallest combined shifts of 35 cm^{-1}. The remaining mutants exhibited combined shifts of 75-110 cm^{-1}.

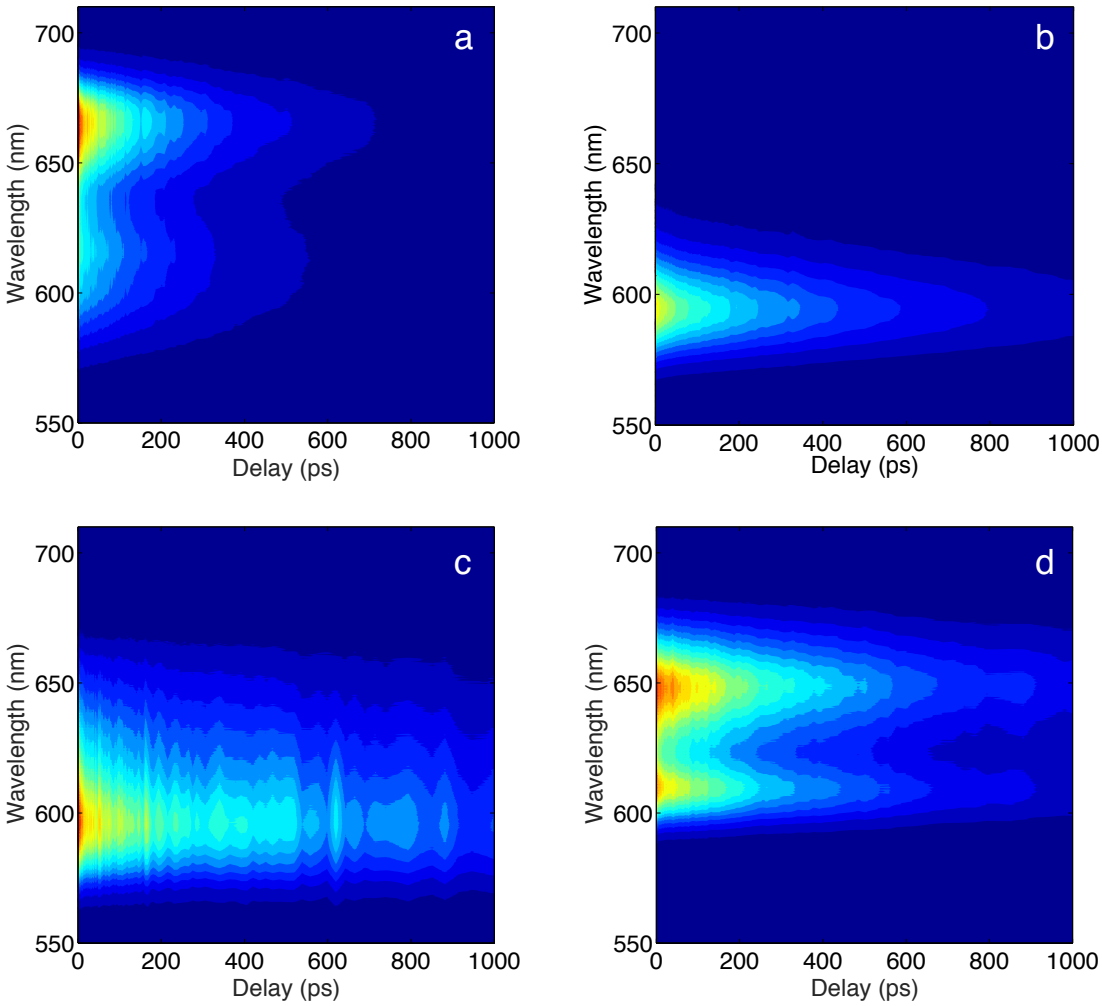

Figure 4.2. SRTG spectra of (a) TagRFP675, (b) TagRFP675 Q41M, (c) mKate, and (d) mKate M41Q.

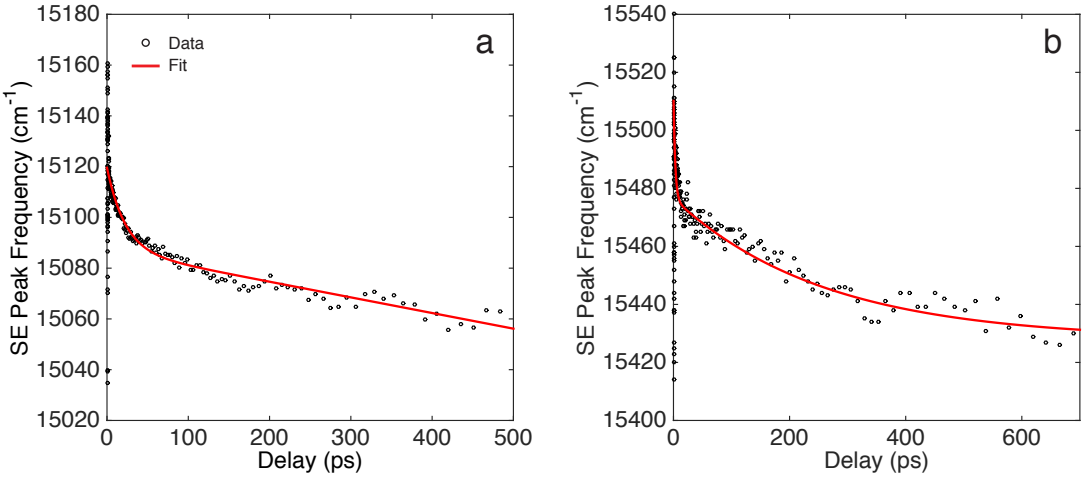

Figure 4.3. SE band peak positions extracted from double Gaussian fitting of SRTG spectra and multiexponential decay fits for (a) TagRFP675 and (b) mKate M41Q.

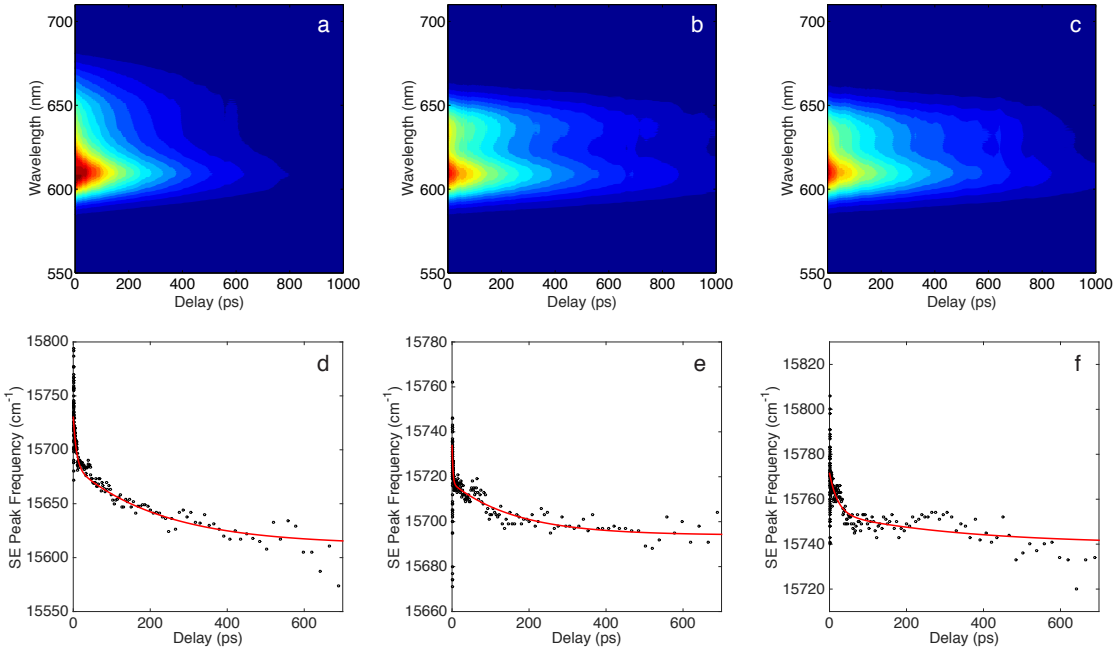

Figure 4.4. SRTG spectra and fitted SE band positions for various time delays of (a) TagRFP675 F62A, (b) TagRFP675 Q106M, (c) TagRFP675 Q106M F62A.

Table 4.2. Fitting parameters assuming multiexponential shift of SE band.

Mutant	Amplitude (cm^{-1})	τ_1 (ps)	Amplitude (cm^{-1})	τ_2 (ps)
mKate	--	--	--	--
mKate M41Q	30	5	52	355
TagRFP675	33	17	44	397
TagRFP675 Q41M	--	--	--	--
TagRFP675 F62A	41	7	68	159
TagRFP675 Q106M	12	4	24	219
Tag RFP675 F62A Q106M	18	24	17	537

Table 4.3. Fitting error analysis for multiexponential fits to SE band shifts. The given values represent 95% confidence intervals for the parameters of the fit equation: $f(t) = a \cdot e^{-bt} + c \cdot e^{-dt}$. Amplitudes are expressed in wavenumbers (cm^{-1}) and time constants are reported as e^{-1} lifetimes in picoseconds.

Mutant	a (cm^{-1})		b (ps)		c (cm^{-1})		d (ps)	
mKate	--	--	--	--	--	--	--	--
mKate M41Q	27	33	4	7	50	55	317	404
TagRFP675	27	39	12	31	38	50	309	552
TagRFP675 Q41M	--	--	--	--	--	--	--	--
TagRFP675 F62A	36	47	5	10	63	73	138	186
TagRFP675 Q106M	8	15	3	15	22	27	177	286
Tag RFP675 F62A Q106M	14	22	16	46	13	21	363	1033

Table 4.4. Amplitude decay fits of SE band extracted from SRTG spectra for variants demonstrating an excited state response.

Mutant	Amplitude	τ_1 (ps)	Amplitude	τ_2 (ps)
mKate	--	--	--	--
mKate M41Q	0.15	2598	0.85	349
TagRFP675	0.17	467	0.83	159
TagRFP675 Q41M	--	--	--	--
TagRFP675 F62A	0.77	269	0.23	39
TagRFP675 Q106M	0.35	700	0.65	214
Tag RFP675 F62A Q106M	0.14	407	0.86	15

The SE band amplitude for each mutant (Table 4.4), integrated over all wavelengths, versus time delay were determined from fits to a multiexponential decay. This value should reflect the fluorescence lifetime previously reported as 900 ps for TagRFP675[50]. The SRTG SE lifetimes appear 2x shorter due to the effect of homodyne detection. Considering this adjustment, the results here are in qualitative agreement with previous findings with a few exceptions. A lifetime component of ~1 ns was observed in most species. Their multiexponential character with both faster and slower timescales alludes to complex photophysical behavior predicted for RFPs[146]. Variation among the point mutants is observed and is not surprising given the effect of disrupting local chromophore-sidechain interactions on other spectral properties.

MD Simulations

The timescales extracted from the SE SRTG response report directly on the excited state nuclear reorganization thought to contribute to the extended Stokes

shift of far-red emitting RFPs, including TagRFP675. We utilized MD simulations to connect the experimental results to specific chromophore-sidechain interactions. While a fully quantum mechanical treatment is required to model an excited electronic state, classical MD simulations are considered a valid method to capture the timescales of molecular motions contributing to excited state solvation within the linear response approximation[162].

MD trajectories of each mutant were carried out to examine chromophore flexibility and the possibility of interconversion between hydrogen bond states as previously observed in mPlum. These modeling results represent only a preliminary investigation of the TagRFP675 system. Further analysis including simulations on the remaining mutants is ongoing and will be included in a future manuscript. We first examined the dynamics of the interaction at positions 62 and 41 in TagRFP675 and mKate M41Q. In Figure 4.5, the time trajectories of the proximity, expressed as Δr, between the participating atom in the Q41 sidechain and the N-acylimine oxygen of residue F62. It is apparent that both variants occupy only single conformation throughout the 50 ns trajectory, which is identified as direct hydrogen bond through analysis of the output coordinates. This is in contrast to the behavior observed in mPlum.

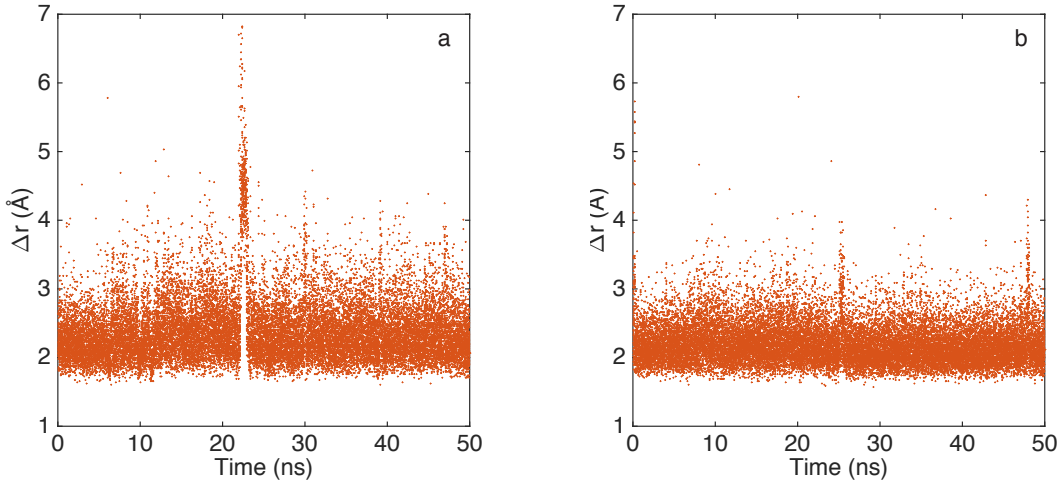

Figure 4.5. Time trajectories of the Q41-acylimine carbonyl distance (Δr) for (a) TagRFP675 and (b) mKate M41Q. Δr refers to the distance between the sidechain of Q41 and the N-acylimine oxygen of F62.

The hydrogen bond behavior between S28 and Q41 was also assessed. This interaction was identified in the crystal structure and was speculated to play a role in stabilizing the interaction between Q41 and F62. The MD trajectory presented in Figure 4.6 illustrates unique results for the two species. TagRFP675 exhibits intermittent conversion between two discrete proximities, while mKate M41Q primarily occupies the closest substate. These results are also depicted as probability histograms in Figure 4.7.

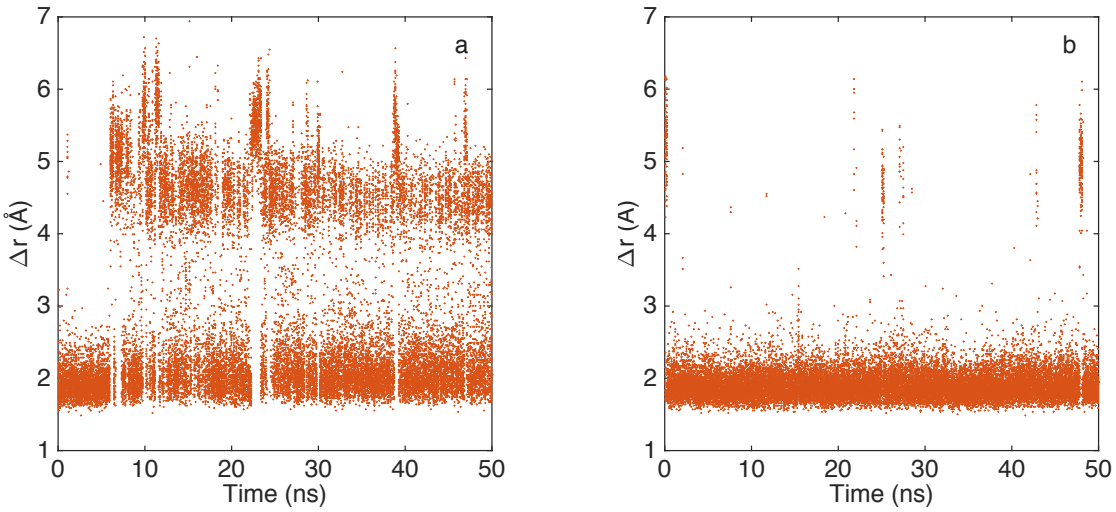

Figure 4.6. Time trajectories of the S28-Q41 distance (Δr) for (a) TagRFP675 and (b) mKate M41Q. Δr is defined as the distance between the sidechains of S28 and Q41.

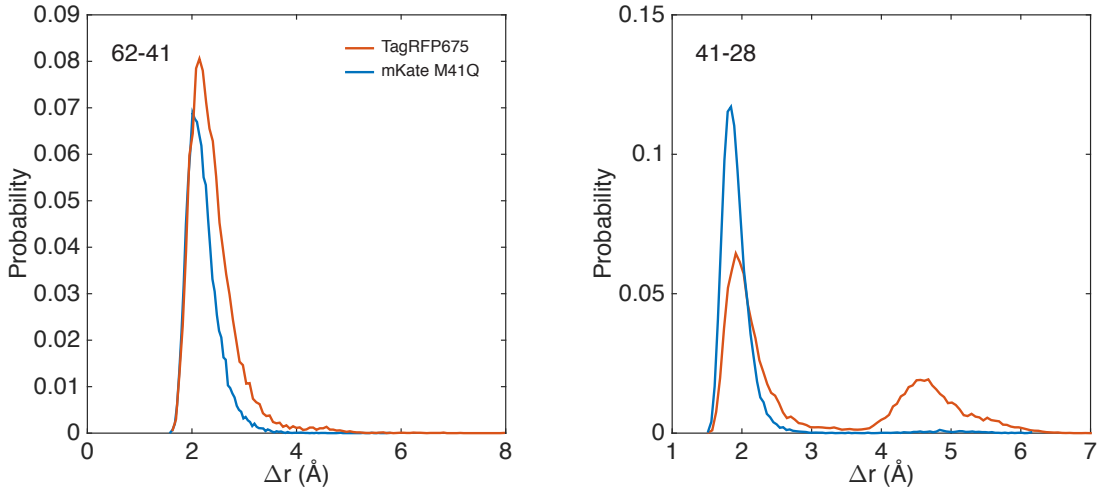

Figure 4.7. Histograms of the probability for the Q41-F62 and Q41-S28 separations, Δr, to occur during the MD simulations.

The two substates for the TagRFP675 41-28 proximity were identified as direct and water-mediated hydrogen bonds through coordinate analysis. The water-mediated bond forms following intermittent rotation of the S28 sidechain and simultaneous migration of a water molecule. The distance distributions were broader for TagRFP675 indicating greater sidechain flexibility, which may facilitate this

structural rearrangement. The prevalence of participating hydrogen bonds to the chromophore for all mutants is tabulated below. Percentages are mostly consistent across all mutants aside from the 41-62 interaction reaffirming its importance for driving excited state stabilization.

Table 4.5. Hydrogen-bonding to the chromophore from neighboring sidechains presented in terms of time fraction as calculated from MD simulations. For each mutant, bonds with sidechains Q41, Q106, W90, and S28 are reported. For all entries, 3.5 Å distance and 30° angle cut-off values were used for defining a hydrogen bond.

	41-62 (%)	106-H_2O (%)	28-41 (%)	H_2O-CHR (%)	W90-CHR (%)
TagRFP675	49	74	81	34	57
mKate	--	79	--	32	66
mKate M41Q	63	81	83	32	70

4.4 Discussion

Specific hydrogen-bonding interactions identified in crystal structures have been implicated as the origin of the extended Stokes shift of TagRFP675. Two hydrogen bonds were identified at the N-acylimine carbonyl end of the chromophore as illustrated in Figure 4.1. The time-resolved spectroscopy results help shed light on the mechanism of excited state stabilization and relative importance of these interactions. The SRTG data indicate picosecond solvation previously attributed to similar hydrogen bond dynamics in mPlum[168]. However, distinct behavior is observed among the different mutants studied. Variants lacking a direct hydrogen bond with the Q41 sidechain (mKate, TagRFP675 Q41M) show no clear solvation on the experimental timescale. Addition of this interaction to mKate with a single M41Q mutation leads to a dramatically larger Stokes shift on par with

TagRFP675 and nearly equivalent solvation dynamics. Disruption of the water-mediated hydrogen bond between Q106 and the N-acylimine was attempted with the TagRFP675 F62A, Q106M, and F62A Q106M mutants. A ~300 cm^{-1} smaller Stokes shift is observed for each of these species that reflects the removal of this bond. Oddly, this perturbation seems to have only a small effect on overall solvation dynamics where a modest increase in the slow relaxation was observed for F62A and Q106M. We attribute this difference to a change in flexibility of the N-acylimine carbonyl given a reduction in steric hindrance of the phenylalanine ring in F62A and loss of the water-mediated hydrogen bond in Q106M. These results suggest that the direct hydrogen bond at the N-acylimine carbonyl has the highest impact on extending Stokes shift in TagRFP675.

The hydrogen bond behavior of TagRFP675 is strikingly different than observed for mPlum, where interconversion between two unique conformations was predicted at the N-acylimine position, which appeared to correlate with the magnitude of the Stokes shift among a panel of point mutants[168]. Investigation of this *dynamic* component was similarly carried out in this study. The MD modeling results shown in Figure 4.5 suggest that the hydrogen bond with Q41 does not undergo conformational interconversion on the timescales observed in mPlum. An identical analysis was conducted for the water-mediated hydrogen bond with Q106, which demonstrated slow ~ns sidechain rotation in TagRFP675. A similar conformational change was predicted for mKate and mKate M41Q, however, they exhibited fast (<ps) recovery to the original hydrogen-bonded state. It is doubtful that these dynamics alone explain the red-shifted emission of TagRFP675 relative to

the parent mKate since its disruption accounts for only a small portion of the overall reorganization energy (~300 cm^{-1}) and its timescale is slower than the excited state lifetime (~900 ps). Flexibility at this position is more likely to account for its reduced quantum yield relative to the parent species either through internal conversion or chromophore cis-trans isomerization evident in crystal structures. The conformational interconversion predicted at the Q41-S28 position is an interesting result. It is possible that this interaction indirectly modulates the hydrogen bond strength of Q41-F62 and thus, chromophore flexibility in a manner similar to mPlum. Alternatively, this behavior may merely reflect a more flexible local environment leading to more robust solvation of the excited chromophore.

Our results further shed light on the role of the N-acylimine in tuning electronic properties of DsRed-like RFPs. Hydrogen bond analysis from MD simulations (Table 4.5) reveals little variation of interactions at other sites on the chromophore among the mutants studied. Its significant impact is surprising given its location at the end of the conjugated ring system. A few possibilities exist to explain this behavior. First, the direct hydrogen bond with neighboring sidechains may act as an anchor to hold the carbonyl in the plane of conjugation and facilitate stabilization of the excited state. Alternatively, this anchor may act to restrain the entire imidazolinone ring and help maintain coplanarity across the entire conjugated system. This model is counterintuitive since a substantial decrease in quantum yield occurs in species having this interaction. A second consideration is flexibility at this end of the chromophore. In principle, solvation is driven by environmental flexibility capable of conforming to a new excited state charge

distribution. The extent of this process, however, might be restricted by nuclear degrees of freedom of the donor and acceptor groups. An example of this is observed with the F62A mutant, which shows a ~300 cm^{-1} loss of Stokes shift compared to TagRFP675, however, is predicted to retain both direct and water-mediated hydrogen bonds at the N-acylimine position. Moreover, this mutation perturbs only the excited state (emission wavelength) and its accelerated solvation compared to the parent is consistent with a change in flexibility at this position possibility due to lessor steric hindrance with the loss of the bulky phenylalanine sidechain.

These results may also be interpreted in the context of designing more robust RFPs. More specifically, developing desirable variants with both red emission wavelength and high fluorescence quantum yield. This goal might be achieved in a few ways. First, Stokes shift can be increased through solvation *via* tertiary interactions (*e.g.* hydrogen bonds or π-π stacking), however, a pliable chromophore environment is most typically accompanied with a sharp drop in quantum yield due to increased nonradiative deactivation. It is unknown whether the hydrogen bond interconversion observed in mPlum might provide an additional route for extending red-emission in TagRFP675. This effect might be modulated by secondary hydrogen bonds that regulate the range of motion of the Q41 sidechain itself. In TagRFP675, S28 forms a hydrogen bond with Q41 while the E16 sidechain in mPlum is unrestricted by a second interaction. The contrasting behavior between TagRFP675 and mKate M41Q at this position identified in the MD simulations suggests it might play a role tuning its photophysical properties. Second, red

emission may be achieved, even with a moderate Stokes shift, with a simultaneous shift in absorption and emission wavelength. This occurs in closely related variants mNeptune and mCardinal, which demonstrate emission around 650 nm with ~3 fold higher quantum yield compared to TagRFP675. Finally, a third possible strategy for RFP optimization involves a combination of the previous models. Identifying structural channels of nonradiative deactivation that are particularly sensitive to quantum yield will be a critical challenge in this effort. Minimizing this effect while exploiting environmental interactions that drive excited state stabilization will be essential to achieving this goal. Nonlinear spectroscopic techniques capable of quantifying the dynamics of the chromophore and its local environment together with theoretical modeling and targeted mutagenesis are uniquely suited for guided exploration of new RFP species.

4.5 Conclusions

The excited state relaxation of the far-red emitting FP TagRFP675 and a panel of strategic point mutants was quantified with SRTG spectroscopy. We found that biexponential solvation occurred on ~10s and 100s of ps timescales. This behavior was attributed to hydrogen bond interactions between the N-acylimine carbonyl of the chromophore and the neighboring sidechains Q106 and Q41 on the basis of MD simulations. In TagRFP675 and mKate M41Q, a direct hydrogen bond was identified between F62 and Q41. While removal of this interaction in TagRFP675 Q41M and mKate coincides with a sharply blue-shifted emission wavelength and loss of transient spectral behavior and implicates its role in extending Stokes shift, the exact mechanism of this is unclear. Preliminary MD

analysis indicates TagRFP675 and mKate M41Q do not undergo hydrogen bond interconversion at the F62-Q41 position in contrast to previous observations of mPlum. However, the supporting S28-Q41 hydrogen bond of TagRFP675 is predicted to undergo similar conformational change. This behavior suggests interactions at the acylimine end of the chromophore might act to modulate its flexibility and are essential for achieving red-shifted emission. Additional modeling of these results will focus on better quantifying chromophore flexibility among the remaining variants. These results further understanding of the mechanism of red emission in RFPs and dynamics of buried probes in protein systems.

Chapter V

Excited State Electronic Landscape of mPlum Revealed by Two-Dimensional Double Quantum Coherence Spectroscopy

As Appeared in the Journal of Physical Chemistry B, 2015, Vol. 119, 3414-3422

5.1 Introduction

Given the combination of their complex photophysics and straightforward physical structure, FPs serve as an ideal model system for investigating the electronic structure of buried optical probes. GFP has garnered most attention to date. It exhibits a high fluorescence quantum yield and reversible photobleaching thought due to excited state proton transfer involving the p-hydroxybenzylidene moiety[169]. Time-resolved spectroscopy has been instrumental in uncovering intermediates within this photocycle having lifetimes ranging from femtoseconds to milliseconds[8, 170]. The study of red fluorescent protein (RFP) electronic structure, however, has remained largely unexplored. Several plausible hypotheses exist to explain the photobleaching phenomena in RFPs including conformational fluctuations about the methylidene bridge, triplet state formation, and increased oxygen permeability stemming from monomerization of the progenitor DsRed[16, 171]. Much effort has focused on understanding interactions between the surrounding environment and positions of the ground and first excited state and their association with emission efficiency[45]. However, a detailed understanding of the electronic structure underlying these photophysics and their relationship with the nature of the local protein environment is largely unexplored.

A broader knowledge of FP excited electronic structure also has practical

implications for advancing imaging applications. For example, multiphoton excitation techniques rely heavily on the position and strength of electronic excitation into single or doubly excited states[172]. However, predicting the position and strength of these transitions is not straightforward given the diverse mechanisms of environmental coupling among a large and increasing set of known FPs[148, 173-174]. Two photon absorption (2PA) studies have shed light on these transitions in several FPs and much debate exists over the peak structure of their spectra[175-176]. Features often attributed to one-photon transitions are slightly blue-shifted from the maxima of the linear absorption spectra. Drobizhev *et al.* explained this shift in terms of vibronic coupling[177]. Moreover, 2PA is also observed at energies higher than the expected S_0-S_1 region in some variants. These were assigned as transitions to higher lying electronic states, S_0-S_n, and their unusually large cross sections were attributed to near-resonance enhancement known to occur in large aromatic systems[175]. We recently reported on the time-resolved solvation dynamics of a series of mPlum mutants, where an ESA contribution observed on the low energy side of GSB led to a reduction in the magnitude of red-shift by the stimulated emission contribution[168]. This observation, along with another transient absorption study confirms the existence of nearby S_n states, but did not aim to precisely determine their transition energies or intensities[178].

In recent years, sophisticated coherent multidimensional spectroscopic techniques have been developed to effectively spread an absorption spectrum over two frequency axes whose time dependence can be monitored with femtosecond precision[110]. This information has proven invaluable for deciphering complex

electronic structure in congested spectral regions and energy transfer events within multichromophoric systems such as photosynthetic light harvesting complexes[69]. The utility of analogous NMR and vibrational spectroscopic methods has been routinely demonstrated for many years, but only recently with electronic transitions at optical frequencies given the challenges associated with femtosecond pulse generation and subcycle phase control[110].

The most frequently employed 2D electronic spectroscopy method examines the correlation between absorption and emission frequencies centered about the energy of the fundamental electronic transition (*i.e.* from ground the to first excited state). A closely-related third order optical response probes double quantum pathways that lead to oscillations near twice the incident laser frequency[179]. For a typical molecular system, this roughly overlaps with a two-electron state resulting in coherence of a double quantum resonance. Exposure to a subsequent third pulse yields signals projected from its constituent single quantum resonances leading to a spectrum that correlates single and double quantum transitions. This technique has been used in the mid infrared to decipher protein structures in biological systems, many-body effects in semiconductor quantum wells, and electron correlation effects in organic dyes[180-185]. For a three level system (3LS), in a ladder configuration, the double quantum spectrum exhibits two peaks of opposite sign, when projected on the emission axis, that represent the 0-1 and 1-2 energy gaps. The inclusion of additional states and vibrational modes leads to additional responses and complicate the peak shapes[186].

In this study, we find that 2D2Q spectra of mPlum are distinctly different from those of cresyl violet in methanol, previously well described as a 3LS. A combination of excitation dependent 2D2Q, SRTA spectra, and model calculations suggest mPlum is most consistent with a 1-1-2 electronic level structure, with two levels in the doubly excited manifold with opposite anharmonicity. These results are discussed in the context of known RFP excited-state properties.

5.2 Experimental Methods

Multidimensional Spectroscopy

Double Quantum Two-Dimensional Fourier Transform Spectroscopy (2D2Q) was carried out in the BOXCARs geometry with excitation and local oscillator beams arranged on the corners of a 1-inch square. Upon irradiation with 3 excitation pulses (~2 nJ/beam, 20 kHz), generated from a noncollinear optical parametric amplifier (20 fs, Wyvern-20 KM Labs), the spatially isolated four wave mixing signal is emitted in the prescribed $\mathbf{k_{sig}}=\mathbf{k_1}+\mathbf{k_2}-\mathbf{k_3}$ phase matching direction. The sample was contained between two fused silica windows (1-inch diameter, 1 mm thick) separated by a 250 μm Teflon spacer and was refreshed with a spinning cell rotating at 3000 rpm to mitigate photobleaching and accumulation of laser-induced photoproducts. Spectrally-resolved detection was carried out with a liquid N_2-cooled CCD camera. This dimension represents the emission frequency, Ω_{emis}. Data was collected as a function of the t_2 time delay in 0.89 fs increments and subjected to Fourier analysis yielding Ω_{exc} frequency information.

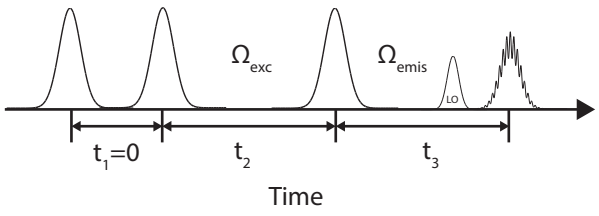

Figure 5.1. Excitation pulse sequence used to generate the third order nonlinear optical signal.

Phase stability of the temporal delays between pulses within the excitation sequence (Figure 5.1) is required to execute heterodyne detection and temporal sampling with interferometric precision. This stability is exceedingly important in the optical regime where environmental drifts may cause appreciable phase fluctuations within the experimental time interval. To minimize this effect, we employed an active phase stabilization system where pathlengths are controlled *in situ* by piezo-driven mirrors inside the JILA-MONSTR nonlinear spectroscopic platform[106]. Typical phase stabilities exceeded $\lambda/200$.

The raw spectral data for all time delays was compiled into a single matrix for data processing and normalized with the square root of the local oscillator intensity. Detected wavelength data was resampled to the frequency domain. Next, spectral filtering along the emission frequency dimension was conducted using Fourier analysis to remove extraneous signal components. Finally, Fourier transformation along the t_2 dimension was carried out to extract excitation frequency information. The excitation frequency vector was calculated in accordance with the Nyquist theorem assuming a temporal sampling interval of 0.89 fs.

Sample Preparation

Samples of mPlum were purified from a bacterial expression system based on the pBAD vector. Expression plasmids were transformed into Top10 *E. coli* followed by induction with 0.02% arabinose for 24 hours. Purification *via* 6X-His tag/Ni-NTA chromatography was carried out and samples were subsequently buffer-exchanged with 15 mM pH 8.0 TRIS buffer, 100 mM KCl. Linear absorption and emission spectra verified the purity of the final product. Cresyl violet was purchased from Sigma-Aldrich and used as received. Samples were dissolved in spectroscopic grade methanol. Sample concentrations were carefully selected to avoid aggregation and reabsorption of the nonlinear signal (0.15 OD, ~50 μM).

5.3 Results

Steady State Spectroscopy

Steady state absorption and emission spectra are shown in Figure 5.2.

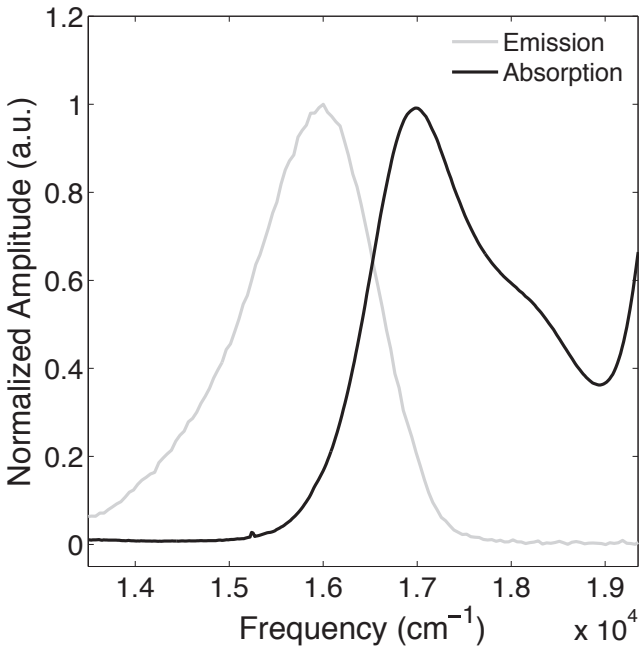

Figure 5.2. Steady state absorption and emission spectra of mPlum.

Peak positions of 16978 and 15408 cm^{-1} respectively are consistent with those previously reported[44]. mPlum SRTA spectra collected with center excitation wavelengths of 16447 and 17241 cm^{-1} are presented in Figure 5.3. Excitation dependence reveals strong positive and negative features reflecting Ground State Bleach (GSB) and Excited State Absorption (ESA) contributions. The GSB position closely matches the linear absorption peak as expected, however it is slightly obscured by an overlapping ESA feature. Interestingly, the relative position of ESA to GSB differs with excitation, falling at both higher and lower energies. These spectra suggest the existence of two ESA bands although we cannot immediately discount the possibility of a single broad overlapping ESA using this one-dimensional technique.

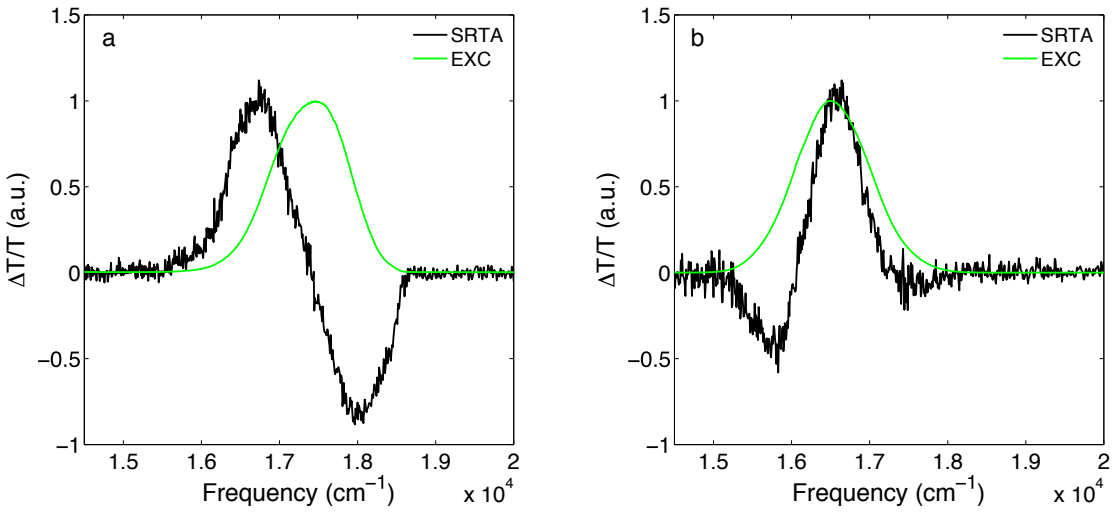

Figure 5.3. SRTA spectra of mPlum, with center excitation wavelength of (a) 17241 and (b) 16447 cm^{-1}. Excited state absorption components ($\Delta T/T<0$) are evident on either side of the GSB band.

Multidimensional Spectroscopy

2D2Q data for cresyl violet in methanol and mPlum are reported in Figures 4.4

and 5.5. For cresyl violet, the absolute value spectrum exhibits a single inhomogeneously broadened peak with intensity spanning across the diagonal in close agreement with that previously reported[183].

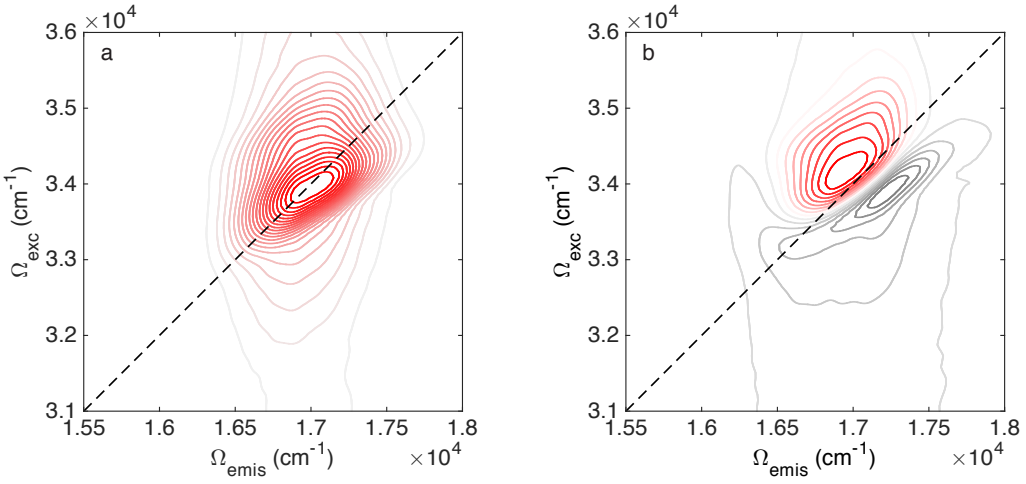

Figure 5.4. (a) Absolute value and (b) real 2D2Q spectra of cresyl violet in methanol.

The real component is consistent with the expected 3LS peak arrangement with a single positive and negative feature above and below the diagonal, respectively, representing the two optical responses respectively with positive anharmonicity. The mPlum spectrum is strikingly different from cresyl violet, and exhibits separate inhomogeneously broadened peaks above and below the diagonal at Ω_{emis}~16400 cm^{-1}. The higher energy peak shows a shoulder on the low energy edge suggesting the presence of a third peak.

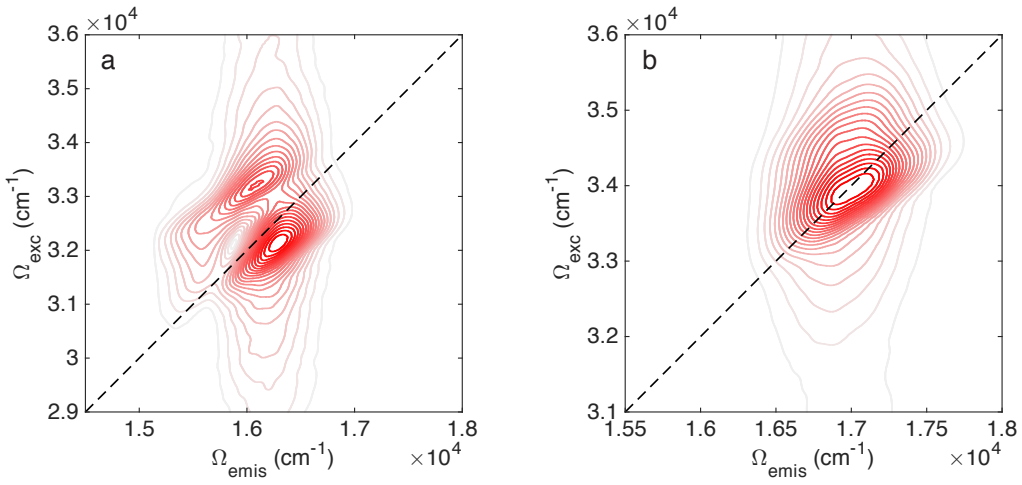

Figure 5.5. Absolute value 2D2Q spectra of (a) mPlum and (b) cresyl violet.

To better understand the 2D2Q peak structure of mPlum, we explored the excitation dependence of this response. The spectrum collected at blue excitation (16949 cm^{-1}) in Figure 5.6b displays two peaks of roughly equal intensity vertically aligned at ~17000 cm^{-1} closely matching the linear absorption peak of 16978 cm^{-1}. The red excitation (Figure 5.6f, 15748 cm^{-1}) produces a strong feature above the diagonal with Ω_{emis} =15500 cm^{-1}, along with a weaker peak below the diagonal at slightly higher energy. We attribute the peak above the diagonal to the anomalous shoulder observed in Figure 5.5. Moreover, the presence of a third response indicates mPlum demonstrates an electronic structure differing from that of cresyl violet, which was well modeled as a 3LS. The orientation and eccentricity of this anomalous peak varies slightly from those of blue excitation suggesting unique bath coupling among the different states.

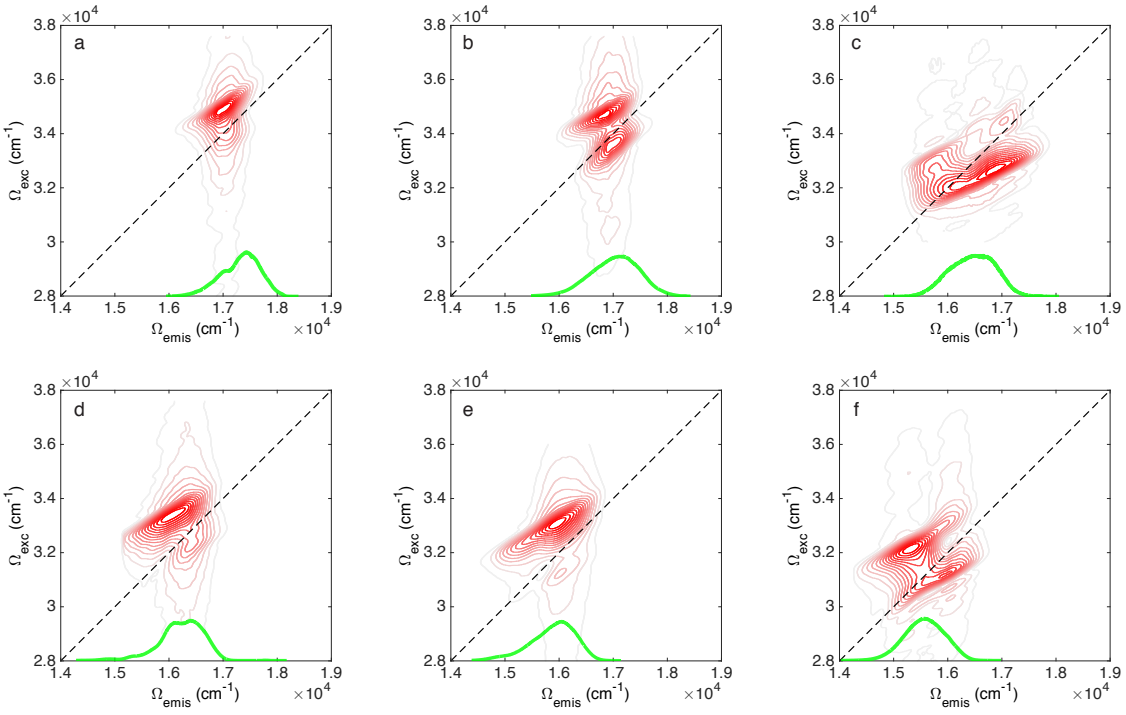

Figure 5.6. Absolute value 2D2Q spectra of mPlum with excitation center wavelengths of (a) 17452, (b) 16949, (c) 16447, (d) 16207, (e) 16000, and (f) 15748 cm^{-1} all with a bandwidth of 1000 cm^{-1} +/- 3%. Measured excitation spectra are overlaid in green along the emission frequency axis.

Model Calculations

Simulations of 2D2Q spectra were performed with a widely-used nonlinear response function approach to the third order polarization[187].

$$P^{(3)}(r,t) = \int_{-\infty}^{\infty}\int_{-\infty}^{\infty}\int_{-\infty}^{\infty} dt_3\, dt_2\, dt_1 E(r,t-t_1)E(r,t-t_1-t_2)E(r,t-t_1-t_2-t_3)R^{(3)}(t_1,t_2,t_3) \quad (5.1)$$

The following Liouville pathways define the response functions for a *N*-level electronic system[78].

$$S^{(3)}(t_1,t_2,t_3) = \left(\frac{i}{\hbar}\right)^3 \Theta(t_1)\Theta(t_2)\Theta(t_3)\sum_{\alpha=1}^{4}\sum_{\beta=1}^{N}\left[R_{\alpha\beta}(t_1,t_2,t_3) - R^{*}_{\alpha\beta}(t_1,t_2,t_3)\right] \quad (5.2)$$

In addition to the 3LS response, three additional electronic structures were explored: a mixture of two independent 3LS and with the effect of two closely

spaced levels in the first and second excited states (separation ~1500 cm^{-1}), denoted as 1-2-1 and 1-1-2 respectively (Figure 5.7).

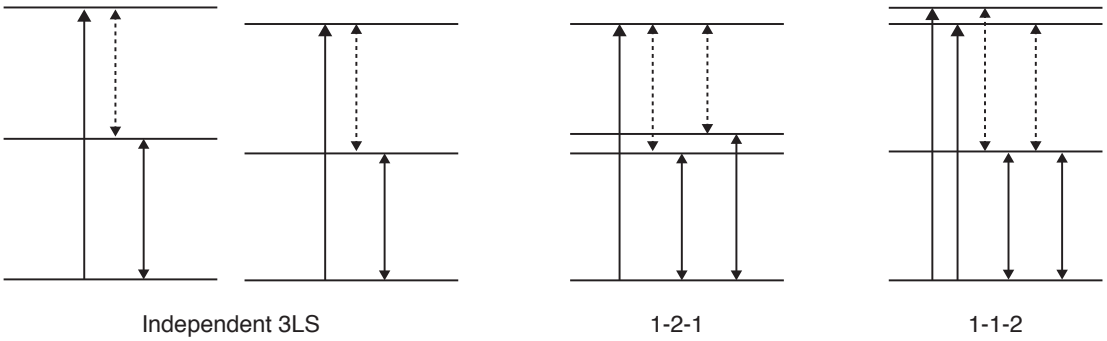

Figure 5.7. Electronic level structures considered for modeling of 2D2Q data: two independent three level systems and 1-2-1 and 1-1-2 four level systems. The arrows represent possible responses for double quantum coherence pathways.

The inclusion of additional electronic states alters the response expected for a single 3LS. The double-sided Feynman diagrams in Figure 5.8 describe these additional responses for the 1-1-2 level structure. Here, R_1 and R_2 represent the previously described contributions for a 3LS[187].

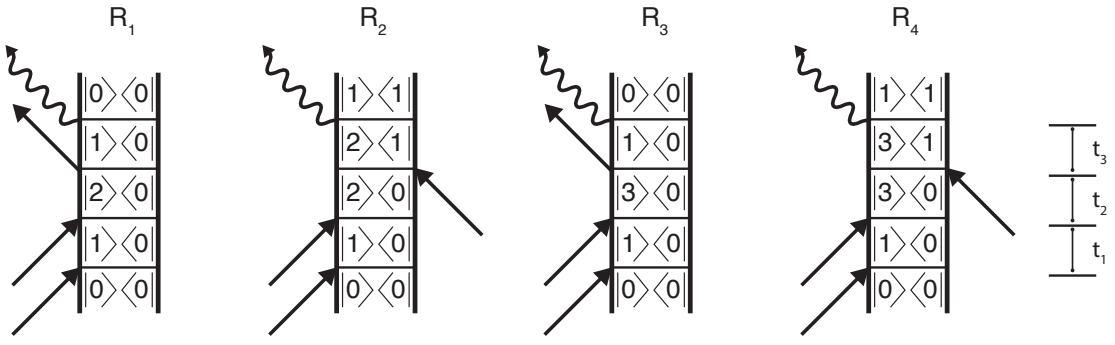

Figure 5.8. Light-matter interactions representing the double quantum responses of a 1-1-2 electronic level structure.

To simplify spectral interpretation, calculations were performed in the Bloch limit with an exponential dephasing constant Γ_{ij} and impulsive excitation.

Transition dipole moments, μ_{ij}, were set to be equal between all states and an anharmonicity of 1000 cm^{-1} was assumed for all calculations. Following these approximations, the frequency domain response for a 3LS following the above assumptions within the rotating wave approximation is

$$S^{(2D2DQ-3LS)}\left(\Omega_{exc},\Omega_{emis}\right)=\frac{\mu_{21}^2\mu_{10}^2}{\left(\Omega_{exc}-\Omega_{20}\right)^2+\Gamma_{20}^2}\times \left\{\frac{\Gamma_{10}\Gamma_{20}-\left(\Omega_{emis}-\Omega_{10}\right)\left(\Omega_{exc}-\Omega_{20}\right)}{\left(\Omega_{emis}-\Omega_{10}\right)^2+\Gamma_{10}^2}-\frac{\Gamma_{21}\Gamma_{20}-\left(\Omega_{emis}-\Omega_{21}\right)\left(\Omega_{exc}-\Omega_{20}\right)}{\left(\Omega_{emis}-\Omega_{21}\right)^2+\Gamma_{21}^2}\right\} \tag{5.3}$$

Here, Ω_{exc} and Ω_{emis} are the corresponding frequency analogues of t_2 and t_3. Moreover, the terms inside the brackets represent the R_1 and R_2 responses described by the Feynman diagrams in Figure 5.8. A treatment including nearly degenerate states at either the first or second excited level incorporates additional responses following a similar pattern as the 3LS case. For 1-1-2, the predicted response is as follows

$$S^{(2D2Q-112)}\left(\Omega_{exc},\Omega_{emis}\right)=\frac{\mu_{21}^2\mu_{10}^2}{\left(\Omega_{exc}-\Omega_{20}\right)^2+\Gamma_{20}^2}\times \left\{\frac{\Gamma_{10}\Gamma_{20}-\left(\Omega_{emis}-\Omega_{10}\right)\left(\Omega_{exc}-\Omega_{20}\right)}{\left(\Omega_{emis}-\Omega_{10}\right)^2+\Gamma_{10}^2}-\frac{\Gamma_{21}\Gamma_{20}-\left(\Omega_{emis}-\Omega_{21}\right)\left(\Omega_{exc}-\Omega_{20}\right)}{\left(\Omega_{emis}-\Omega_{21}\right)^2+\Gamma_{21}^2}\right\}+ \frac{\mu_{31}^2\mu_{10}^2}{\left(\Omega_{exc}-\Omega_{30}\right)^2+\Gamma_{30}^2}\times \left\{\frac{\Gamma_{10}\Gamma_{30}-\left(\Omega_{emis}-\Omega_{10}\right)\left(\Omega_{exc}-\Omega_{30}\right)}{\left(\Omega_{emis}-\Omega_{10}\right)^2+\Gamma_{10}^2}-\frac{\Gamma_{31}\Gamma_{30}-\left(\Omega_{emis}-\Omega_{31}\right)\left(\Omega_{exc}-\Omega_{30}\right)}{\left(\Omega_{emis}-\Omega_{31}\right)^2+\Gamma_{31}^2}\right\} \tag{5.4}$$

with two additional terms stemming from simultaneous coherence within the nearly degenerate doubly excited states. Likewise, for the case of two levels in the singly excited manifold, the signal is predicted to have the following form.

$$
\begin{aligned}
&S^{(2D2Q-121)}\left(\Omega_{exc},\Omega_{emis}\right)=\frac{\mu_{32}^{2}\mu_{20}^{2}}{\left(\Omega_{exc}-\Omega_{30}\right)^{2}+\Gamma_{30}^{2}}\times \\
&\left\{\frac{\Gamma_{20}\Gamma_{30}-\left(\Omega_{emis}-\Omega_{20}\right)\left(\Omega_{exc}-\Omega_{30}\right)}{\left(\Omega_{emis}-\Omega_{20}\right)^{2}+\Gamma_{20}^{2}}-\frac{\Gamma_{32}\Gamma_{30}-\left(\Omega_{emis}-\Omega_{32}\right)\left(\Omega_{exc}-\Omega_{30}\right)}{\left(\Omega_{emis}-\Omega_{32}\right)^{2}+\Gamma_{32}^{2}}\right\}+ \\
&\frac{\mu_{31}^{2}\mu_{10}^{2}}{\left(\Omega_{exc}-\Omega_{30}\right)^{2}+\Gamma_{30}^{2}}\times \\
&\left\{\frac{\Gamma_{10}\Gamma_{30}-\left(\Omega_{emis}-\Omega_{10}\right)\left(\Omega_{exc}-\Omega_{30}\right)}{\left(\Omega_{emis}-\Omega_{10}\right)^{2}+\Gamma_{10}^{2}}-\frac{\Gamma_{31}\Gamma_{30}-\left(\Omega_{emis}-\Omega_{31}\right)\left(\Omega_{exc}-\Omega_{30}\right)}{\left(\Omega_{emis}-\Omega_{31}\right)^{2}+\Gamma_{31}^{2}}\right\}
\end{aligned}
\tag{5.5}
$$

The 4LS responses appear similar to that of a 3LS with signal arising from ground to first excited state and first to doubly excited transitions respectively with opposite signs. However, the additional level leads to a second pair of peaks in each case compared to a 3LS.

Results of Model Calculations

2D2Q spectra were simulated within the Bloch limit for the three different models of the electronic structure depicted in Figure 5.7. The relative anharmonicity of the level positions is an important factor when interpreting 2D2Q spectra. We considered all possible permutations for all level schemes. These are denoted as [*i j*], where *i* and *j* are the anharmonicities of the two states in the doubly excited manifold. For example, the 1-1-2 electronic structure with [+ -] anharmonicity has one state at less than double the value of the single quantum energy (*i.e.* "-" anharmonicity) and one state at more than double the value of the single quantum energy gap (*i.e.* "+" anharmonicity). Level positions were chosen to best reproduce the experimental data and exact values are tabulated below.

Table 5.1. Energy values (cm^{-1}) for various electronic level structures used to model 2D2Q experimental data.

Two 3LS		
[+ -] LA_1=LA_2		
0	0	
17000	17000	
33000	35000	
[+ -] LA_1≠LA_2		
0	0	
16500	17500	
32000	36000	
[+ +]		
0	0	
17000	17000	
35000	36000	
[- -]		
0	0	
17000	17000	
32000	33000	
1-1-2		
[+ -]	[+ +]	[- -]
0	0	0
17000	17000	17000
33000	35000	32000
35000	36000	33000
1-2-1		
[+]	[-]	
0	0	
16500	16500	
17500	17500	
36000	32000	

This initial effort is only intended to demonstrate the unique electronic structure of mPlum relative to a known three level system. Several factors that play an important role in determining the peak shapes, including pulse overlap effects, finite excitation bandwidth, and a realistic system-bath coupling model are neglected here and will be explored in a future report.

Simulated double quantum coherence spectra are displayed below. For two independent 3LS, there are three possible anharmonicity configurations, [- -], [+ -], and [+ +]. Cases with an equal and unequal single quantum energy gap with [+ -] anharmonicity, illustrated in Figure 5.9, most closely match the experimental data. While simulated spectra of [+ +] and [- -] anharmonicities are shown in Figure 5.10.

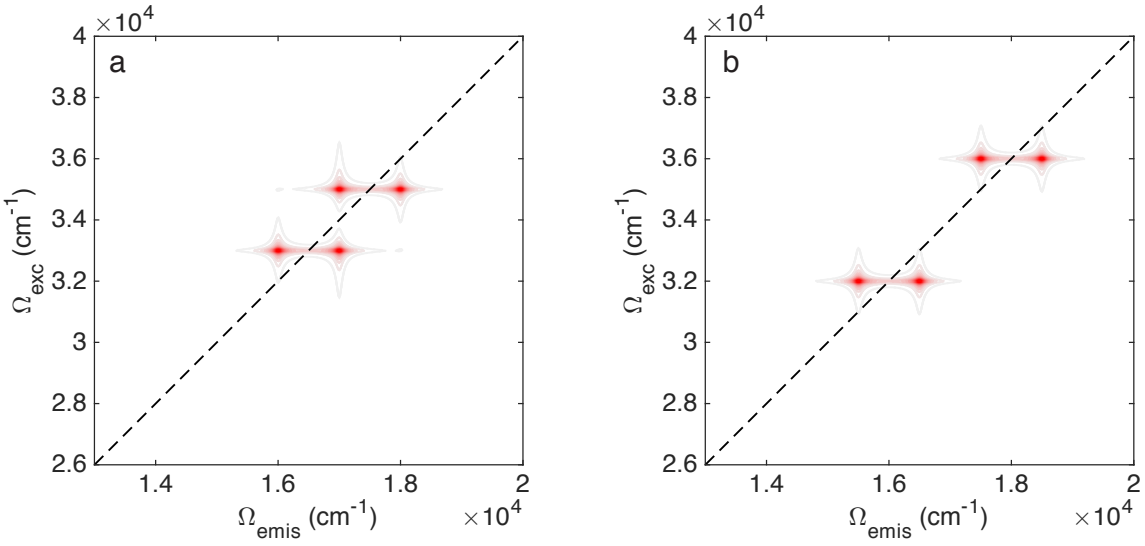

Figure 5.9. Simulated absolute value 2D2Q spectra for two independent 3LS. The two spectra represent cases of (a) equal and (b) unequal linear absorption peaks with [+ -] anharmonicity.

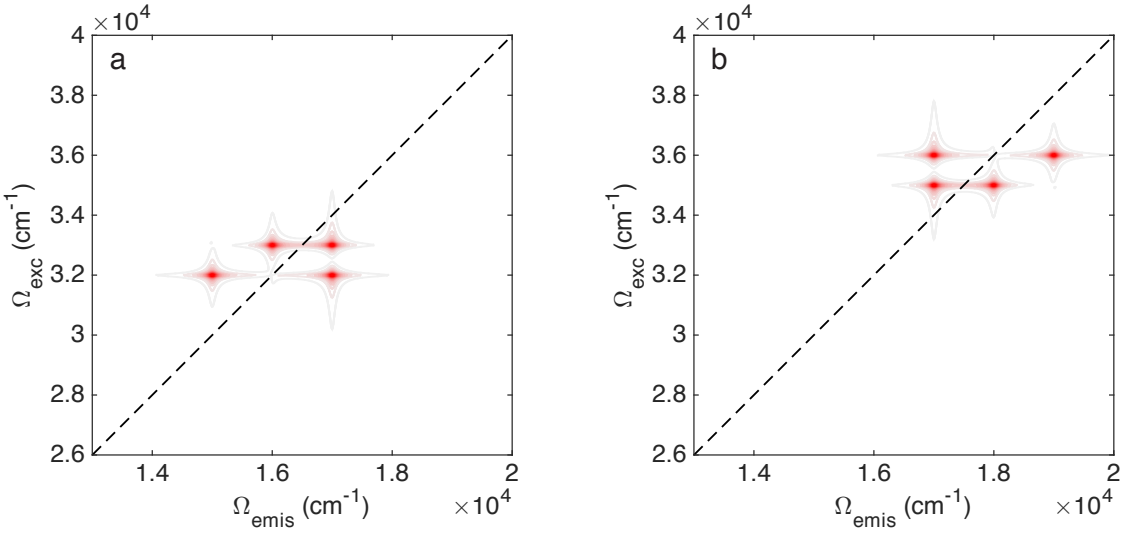

Figure 5.10. Simulated absolute 2D2Q spectra of two 3LS with equal linear absorption and (a) negative and (b) positive anharmonicity.

For the 1-1-2 electronic structure, there are three possible anharmonicities, [- -], [+ -], and [+ +]. Simulated spectra for the [+ -] configuration is provided in Figure 5.11 and the remaining permutations are shown in Figure 5.12.

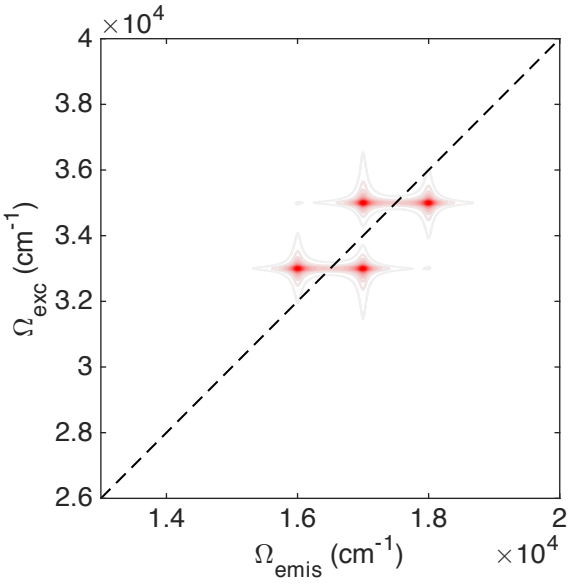

Figure 5.11. Simulated absolute value 2D2Q response of the 1-1-2 level structure with [+ -] anharmonicity.

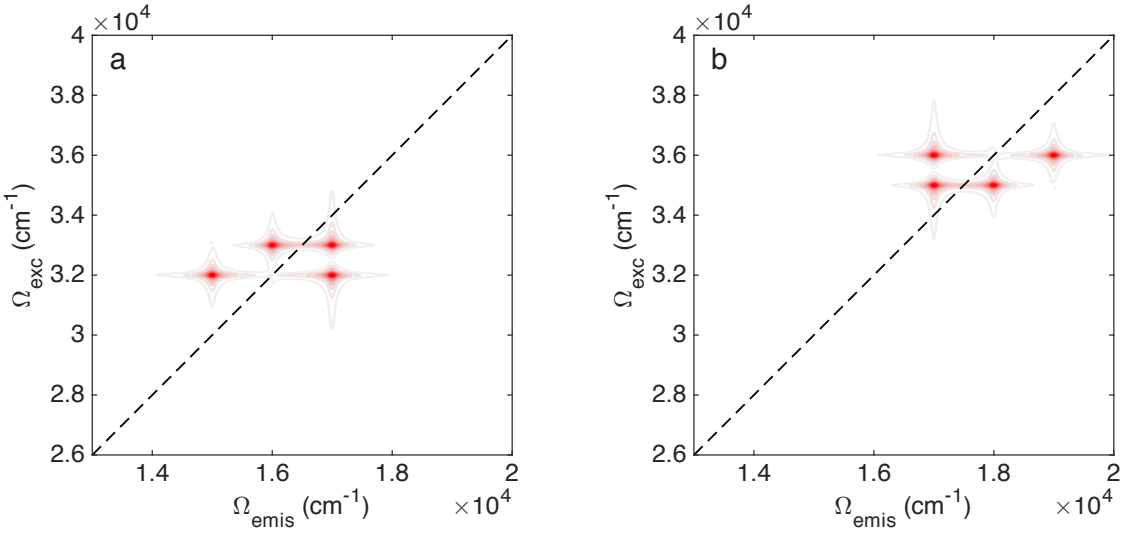

Figure 5.12. Simulated 2D2Q spectra of the 1-1-2 level structure with (a) negative and (b) positive anharmonicity.

The simulated [+ -] spectrum appears almost identical to two independent 3LS with equal linear absorption positions and [+ -] anharmonicity. Lastly, for the 1-2-1 electronic structure, there are two combinations considered with [- -] and [+ +] anharmonicity.

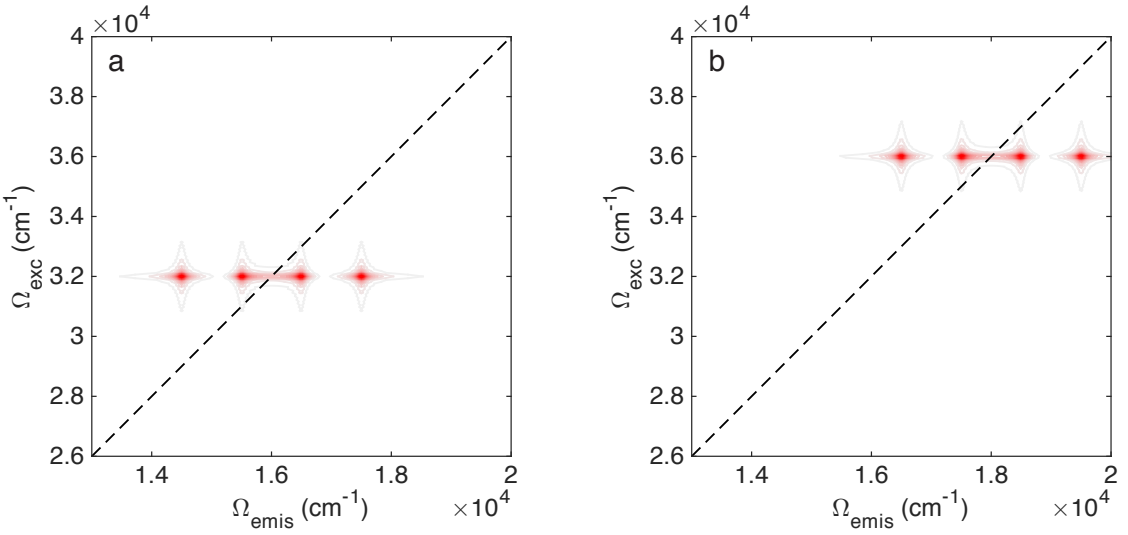

Figure 5.13. Simulated absolute value 2D2Q response of the 1-2-1 level structure with (a) negative and (b) positive anharmonicity.

The modeled spectra are most conveniently characterized by the number of peaks

present along with their sign and relative position to the diagonal boundary. Within these constraints, we can immediately discount a number of possible level schemes, leaving two 3LS [+ -] and 1-1-2 [+ -] as the most likely candidates. We further discriminate between these models in the Discussion section.

2D2Q Spectroscopy of mKate Mutants

To explore the dependence of alteration of the local electrostatic environment, 2D2Q spectra were measured for mKate and related point mutants. Variation at position 158 in mKate and its ancestors is known to strongly influence their photophysical properties leading to a 9-fold improvement in photostability in TagRFP S158T and 3-fold increase in brightness in mKate S158A[188-189]. It is reasonable to assume that the alteration of the chromophore electronic structure may underlie this behavior. These results are presented in Figure 5.14.

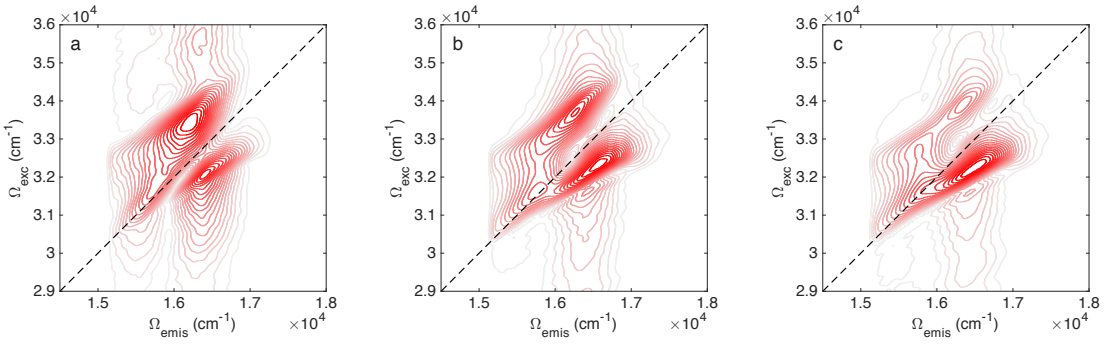

Figure 5.14. Absolute value 2D2Q spectra of (a) mKate, (b) mKate S158A, and (c) mKate S158C.

The absolute value 2D2Q spectra reveal a peak pattern similar to that observed for mPlum. Two peaks roughly vertically aligned at equal Ω_{emis} fall above and below the diagonal, while additional features are observed at lower Ω_{emis} above the diagonal. This suggests that its electronic structure likely follows the 1-1-2

scheme proposed for mPlum. The relative intensities of these features vary among the mutants. This likely reflects incomplete overlap with the center transition frequencies within a finite excitation bandwidth and implies that the positions of these states shift with alteration of the local electrostatic environment. However, considering only these preliminary results, a conclusive relationship between their electronic structure and photophysical parameters is unclear. Further study utilizing broadband excitation would enable more precise quantification of the exact positions of the electronic states and their correlation with mutation. Moreover, development of a systematic panel of variants with known photophysical behavior (*e.g.* dark state conversion, quantum yield) might help better make this connection.

5.4 Discussion

2D2Q spectra reported for dyes in bulk solvents yield two peaks of opposite sign separated by their anharmonicity according to the 3LS responses described in Figure 5.3[179,183]. We first reproduced these measurements to demonstrate the validity of our experimental technique. The third peak in the mPlum spectra suggests a more complex electronic excited state landscape. To explain the additional spectral feature, we favor the model with two closely spaced levels in the doubly excited level, with opposite anharmonicity. This preference was established on the basis of simulated 2D2Q spectra, excitation dependent 2D2Q spectra, and spectrally-resolved transient absorption data.

Since the excitation spectral bandwidth did not fully span the spectral region of interest, excitation dependent 2D2Q measurements were performed to enable

more complete identification of the optical response. The spectral features observed with blue excitation, above and below the diagonal in Figure 5.6 reflect ground to first excited state transitions associated with closely spaced levels in either the single or doubly excited manifolds given their close alignment along Ω_{emis} with the linear absorption peak of 16978 cm^{-1}. The strongest feature under red excitation represents an independent response arising from the |2><1| coherence predicted in R_2. In total, we observe 3 inhomogeneously broadened peaks, 2 centered at $\Omega_{emis} \approx \Omega_{10}$ and 1 below the diagonal at lower Ω_{emis}. Model calculations of the two 3LS and 1-1-2 level structures yield responses similar to the experimental results. Simulated spectra in the Bloch limit show a total of 4 peaks, with 2 vertically aligned at $\Omega_{emis} = \Omega_{10}$ attributed to the ground to first excited coherences and 1 each at lower and higher Ω_{emis} representing coherences between the first and doubly excited states at negative and positive anharmonicity respectively.

Next, we considered these two possible models within the context of RFP molecular structure. A model with two 3LS implies that mPlum is a mixture of two discrete subensembles likely arising from some structural rearrangement within the local protein environment or chromophore itself. While cis-trans isomerization has been reported for some RFP variants, these interconversions typically lead to a significant spectral shift in the linear absorption spectrum following from disruption of the π conjugated system[171,49-50, 189]. For example, the spectral shift between the two chromophore isomers leading to the spectral shift of mKate relative to its parent TagRFP is ~ 900 cm^{-1}. The linear absorption spectrum of the lowest energy transition in mPlum exhibits a single broad peak (~2000 cm^{-1} FWHM) with a

shoulder at higher energy, typical of RFPs and of similar width to the peaks observed in the 2D2Q spectra. We cannot completely discount the existence of conformers with smaller spectral shifts, however, experimental attempts to date addressing such conformational heterogeneity in biological systems are unclear and open to interpretation[144]. Moreover, one would not expect large perturbations at the doubly excited level in this scenario. These results suggest mPlum is most consistent with a 1-1-2 [+ -] electronic structure. This electronic structure is consistent with SRTA results reported in Figure 5.3, which reveals ESA on both the red and blue extremes of the GSB.

Our model calculations for the 1-1-2 [+ -] level scheme predict a 4th peak lying below the diagonal at $\Omega_{emis} > \Omega_{10}$ corresponding to the excited state response from the state of positive anharmonicity. However, this feature is not observed in the experimental 2D2Q spectra. Although we do not have a quantitative explanation for the absence of this peak, we consider three possible explanations. First, we discount the possibility that the peak is unobserved due to insufficient laser spectral bandwidth. The excitation dependence of the mPlum 2D2Q spectrum was probed out to 18500 cm^{-1} as illustrated in Figure 5.6. The short wavelength limit is dictated by the JILA MONSTR output dichroic mirror that separates the reference laser (18797 cm^{-1}) from the femtosecond excitation beams. We feel this spectral cutoff is unlikely to account for the missing peak because the observed peak intensity decays to zero at 17500 cm^{-1} along Ω_{emis}, while some fraction of the signal is still observed above the diagonal along Ω_{exc}. Since the position of this positive feature is coupled to that of the missing peak, it seems the spectral coverage is sufficient to observe a

similar fraction of the signal below the diagonal. A second possible explanation is that the doubly excited mPlum chromophore undergoes population transfer to a neighboring tryptophan sidechain. Typically, the S_1 absorption band of tryptophan is found at 280 nm (35714 cm^{-1}), which coincides with the edge of the observed 2D2Q peaks along Ω_{emis}. We hypothesize that the double quantum coherent state of the chromophore can be electronically coupled to a nearby tryptophan, which then undergoes radiative deactivation, and therefore does not contribute to the nonlinear signal. Crystal structures of mPlum reveal three tryptophan residues within 5 Å of the central chromophore (PDB 2QLG). A third scenario invokes an explanation put forward by Kim *et al*. to explain the mismatch in intensity of above- and below-diagonal features in 2D2Q spectra of cresyl violet[190]. They attribute this to different dephasing rates of the two coherence states in the last evolution period, which ends in emission of the signal. Following this rationale for a 1-1-2 electronic structure, we propose that $\Gamma_{31} > \Gamma_{21}$, thus reducing its relative contribution in the 2D2Q spectrum. One possible reason for the short dephasing time Γ_{31} is a fast nonradiative relaxation from state |3> to |2>, resulting from the small energy gap. This effect would decrease the contribution of R_4 relative to R_2.

Other factors considered to explain the unique 2D2Q response of mPlum are vibronic transitions and finite pulse effects. As discussed and modeled by Nemeth *et al.*, distortions arising from temporal pulse structure can lead to additional peaks and sometimes obscure spectral assignment[179]. However, these features were found to appear along the antidiagonal direction in their simulated spectra. The extraneous feature in our results falls within the area predicted for a degenerate

doubly excited electronic manifold. For a vibronic response, one would expect peaks shifted to lower energies along the Ω_{emis} dimension as previously modeled[190].

These experiments provide a means of contrasting the information extracted from several frequently employed nonlinear techniques including transient absorption, transient grating, and multidimensional methods. In a previous report, we identified an ESA component to the red of GSB via SRTG spectroscopy[168]. Moreover, as illustrated in Figure 5.3, excitation dependent SRTA spectra show ESA bounding GSB at both higher and lower energies. While the 1Q2D spectra of mPlum and cresyl violet exhibit a single inhomogeneously broadened peak, the 2D2Q data suggest a more complicated excited state landscape as illustrated below.

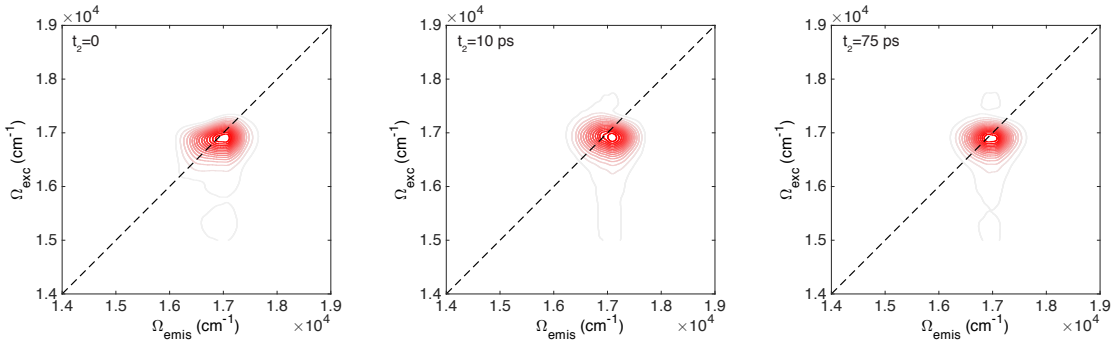

Figure 5.15. mPlum absolute value 2D1Q spectra at t_2=0, 10, and 75 ps.

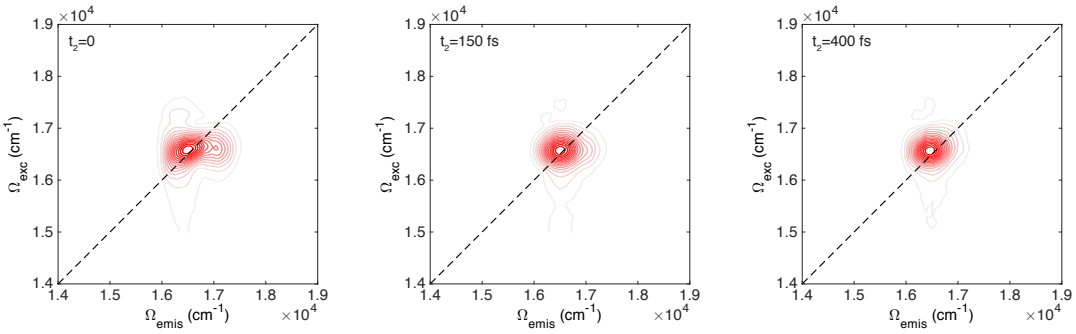

Figure 5.16. Cresyl violet absolute value 2D1Q spectra at t_2=0, 150, and 400 fs.

For instance, it would be infeasible to differentiate a single broad ESA contribution

from two separate ESA contributions considering the SRTA results alone. The 2D2Q spectra facilitate this distinction and demonstrate the power of multidimensional techniques in unraveling congested spectral features.

To date, most insight into RFP electronic structure has originated largely from theoretical model calculations[191-192]. For example, DFT calculations demonstrated the environmental influence of tuning 1PA and 2PA properties in the progenitor DsRed[148]. In another study, the prospect of π-π stacking was explored as a means of generating GFP variants with red-shifted emission[174]. In contrast, experimental accounts addressing the energies and photophysics of higher excited states in RFPs are sparse. As mentioned above, 2PA investigations on the mFruits (mPlum included) revealed absorption on the blue edge near 300 nm[175]. This would coincide with the doubly excited manifold of mPlum, although, they were explained as a resonance enhancement effect resulting from overlap of the excitation laser frequency and singly excited state. Since 2D2Q is not sensitive to this resonance enhancement phenomenon, our results represent a new response independent from the 2PA spectra. It may also explain why cross sections vary widely in this region across the mFruit family.

The finding of multiple doubly-excited states in FPs may have implications for the ongoing development of new fluorophores and imaging techniques. It would be useful to consider the likelihood of excited-state absorption as a criterion for choice of FP variants in a particular imaging modality. Site-directed mutagenesis has shown that FP photostability and brightness vary widely with a mere single

modification near the chromophore[146]. 2D2Q may be helpful in evaluating potential candidates. As described above (Equations 5.3-5.5), the magnitude of the double quantum response is dependent on the individual strengths of the constituent single quantum transitions. Thus, direct quantification of the Ω_{20} transition strength is not possible with 2D2Q experiments alone. However, this technique may be used to precisely survey the landscape of electronic excited states. Broadband (*i.e.* exceeding 2000 cm^{-1} spectral width) 2D2Q would facilitate observation of exact level positions. These studies will be particularly relevant for evaluating photoswitchable variants of FPs for nanoscopic imaging methods that rely on excitation intensities of 10-100 kW/cm^2 or higher[43, 193]. In this intensity regime, multi-photon absorption is possible even with cw excitation, and the probability of photobleaching due to multiple mechanisms increases relative to lower-intensity excitation characteristic of widefield illumination (< 1 kW/cm^2). Thus, tuning of excitation wavelength to minimize absorption into double-quantum states could result in substantial improvement of photostability.

5.5 Conclusions

2D2Q measurements indicate that mPlum displays an electronic structure that differs significantly from a simple organic dye in solution, cresyl violet in methanol. We attribute this response to closely spaced levels in the doubly excited manifold with opposite anharmonicity. These conclusions are supported by excitation dependent SRTA data and simulated spectra derived from third order nonlinear response functions. Since they share virtually the same chromophore structure, we expect that this electronic landscape to be broadly representative of all red

fluorescent proteins, though the positions of the levels are likely sensitive to the local chromophore environment. These results shed light on the largely unexplored electronic structure of RFPs as well as demonstrate the power of multidimensional spectroscopy in unraveling congested spectral features.

Chapter VI

Conclusions and Future Outlook

6.1 Future Outlook

It is important to place this work in the context of the previous fluorescent protein research. Work carried out on red fluorescent proteins to date has been primarily driven by an effort to optimize their emission wavelength, fluorescence quantum yield, and photostability. Development of new FPs was largely accomplished *via* the notion of "rational design" stemming from the information derived from the standard methods of structural biology and protein engineering (*e.g.* x-ray crystallography, linear absorption and emission spectroscopy, and site-directed mutagenesis). These methods, while useful for obtaining a steady-state picture of protein systems, are insensitive to the inherent dynamic aspects of these complex molecular systems. In this thesis, sophisticated nonlinear spectroscopic techniques were utilized to provide new insight into the origin of RFP photophysical properties. These results indicate that a dynamic perspective is necessary to gain a deeper understanding of RFP photophysics and may help guide the engineering of next-generation derivatives.

Adequate computational modeling is critical for analysis of transient spectroscopic data. The transient grating results presented in Chapters III and IV were interpreted with the aid of classical molecular dynamics simulations. Such treatment provides quantification of only ground state molecular fluctuations and is approximated to represent excited state relaxation within linear response theory. A

more accurate simulation of excited state dynamics could be achieved by employing a quantum mechanical modeling of the chromophore electronic structure. Hybrid transient quantum mechanical-molecular mechanics (QM/MM) methods have been developed to simulate dynamics of complex biological systems such as proteins and nucleic acids[194]. For applications involving an optical probe buried in a protein, a typical strategy is to treat the chromophore and important sidechain residues quantum mechanically, while motions of the remaining residues and solvent molecules are approximated with a classical force field. This approach enables a more accurate quantification of the environmental interactions with electronically excited probe, which is critical for developing a fundamental molecular understanding of solvation response. The conclusions drawn in Chapter III, namely, the hydrogen bond switching at the chromophore acylimine carbonyl may be further refined with QM/MM simulations to pinpoint specific vibrational modes integral for this phenomenon and its role in extending the Stokes shift of mPlum and TagRFP675.

The 2D2Q study described in Chapter V demonstrated the power of multidimensional spectroscopy in unraveling congested spectral features of condensed phase electronic lineshapes. In particular, a proposed electronic structure was deduced given the number and pattern of peaks observed in modeled spectra. Further understanding of these results could be achieved through various experimental and theoretical improvements. First, excitation with pulses of limited spectral bandwidth yields only partial coverage of the electronic landscape and hinders spectral assignment. Simultaneous resolution of all nonlinear responses

would be possible with broadband excitation and greatly simplify the task of assigning multiple overlapping spectral features. Second, detection of the signal phase would also enhance clarity of the spectral features enabling determination of the sign of constituent peaks. These refinements are possible with only relatively minor tweaks to the current experimental platform (JILA MONSTR). Finally, incorporation of a more rigorous modeling effort would enable accurate determination of important variables such as peak position, transition strength, and vibronic coupling. This could be accomplished through application of a multimode Brownian Oscillator model, the current standard treatment used to characterize system-bath coupling in the condensed phase. These improvements applied to the study of point mutants that are known to strongly influence RFP photophysics (*e.g.* mKate S158 series) might help connect protein-chromophore interactions to their excited electronic structure and ultimate spectral properties. Such information would be useful for the ongoing effort to design more robust RFP variants.

Bibliography

1. Wu, B.; Piatkevich, K. D.; Lionnet, T., et al., Modern Fluorescent Proteins and Imaging Technologies to Study Gene Expression, Nuclear Localization, and Dynamics. *Current Opinion in Cell Biology* **2011,** *23* (3), 310-317.
2. Day, R. N.; Davidson, M. W., The Fluorescent Protein Palette: Tools for Cellular Imaging. *Chemical Society Reviews* **2009,** *38* (10), 2887-2921.
3. Hein, B.; Willig, K. I.; Hell, S. W., Stimulated Emission Depletion (STED) Nanoscopy of a Fluorescent Protein-Labeled Organelle Inside a Living Cell. *Proceedings of the National Academy of Sciences of the United States of America* **2008,** *105* (38), 14271-14276.
4. Hell, S. W., Far-Field Optical Nanoscopy. *Science* **2007,** *316* (5828), 1153-1158.
5. Hess, S. T.; Girirajan, T. P. K.; Mason, M. D., Ultra-High Resolution Imaging by Fluorescence Photoactivation Localization Microscopy. *Biophysical Journal* **2006,** *91* (11), 4258-4272.
6. Huang, B.; Wang, W. Q.; Bates, M., et al., Three-Dimensional Super-Resolution Imaging by Stochastic Optical Reconstruction Microscopy. *Science* **2008,** *319* (5864), 810-813.
7. Betzig, E.; Patterson, G. H.; Sougrat, R., et al., Imaging Intracellular Fluorescent Proteins at Nanometer Resolution. *Science* **2006,** *313* (5793), 1642-1645.
8. Chattoraj, M.; King, B. A.; Bublitz, G. U., et al., Ultra-Fast Excited State Dynamics in Green Fluorescent Protein: Multiple States and Proton Transfer. *Proceedings of the National Academy of Sciences of the United States of America* **1996,** *93* (16), 8362-8367.
9. Baird, G. S.; Zacharias, D. A.; Tsien, R. Y., Biochemistry, Mutagenesis, and Oligomerization of DsRed, a Red Fluorescent Protein from Coral. *Proceedings of the National Academy of Sciences of the United States of America* **2000,** *97* (22), 11984-11989.
10. Campbell, R. E.; Tour, O.; Palmer, A. E., et al., A Monomeric Red Fluorescent Protein. *Proceedings of the National Academy of Sciences of the United States of America* **2002,** *99* (12), 7877-7882.
11. Shu, X.; Shaner, N. C.; Yarbrough, C. A., et al., Novel Chromophores and Buried Charges Control Color in mFruits. *Biochemistry* **2006,** *45* (32), 9639-9647.
12. Shcherbo, D.; Merzlyak, E. M.; Chepurnykh, T. V., et al., Bright Far-Red Fluorescent Protein for Whole-Body Imaging. *Nature Methods* **2007,** *4* (9), 741-746.
13. Merzlyak, E. M.; Goedhart, J.; Shcherbo, D., et al., Bright Monomeric Red Fluorescent Protein with an Extended Fluorescence Lifetime. *Nature Methods* **2007,** *4* (7), 555-557.
14. Subach, F. V.; Piatkevich, K. D.; Verkhusha, V. V., Directed Molecular Evolution to Design Advanced Red Fluorescent Proteins. *Nature Methods* **2011,** *8* (12), 1019-1026.

15. Shcherbakova, D. M.; Subach, O. M.; Verkhusha, V. V., Red Fluorescent Proteins: Advanced Imaging Applications and Future Design. *Angewandte Chemie-International Edition* **2012,** *51* (43), 10724-10738.
16. Regmi, C. K.; Bhandari, Y. R.; Gerstman, B. S., et al., Exploring the Diffusion of Molecular Oxygen in the Red Fluorescent Protein mCherry Using Explicit Oxygen Molecular Dynamics Simulations. *Journal of Physical Chemistry B* **2013,** *117* (8), 2247-2253.
17. Tsien, R. Y., The Green Fluorescent Protein. *Annual Review of Biochemistry* **1998,** *67*, 509-544.
18. Topol, I.; Collins, J.; Savitsky, A., et al., Computational strategy for tuning spectral properties of red fluorescent proteins. *Biophysical Chemistry* **2011,** *158* (2-3), 91-95.
19. Subach, F. V.; Verkhusha, V. V., Chromophore Transformations in Red Fluorescent Proteins. *Chemical Reviews* **2012,** *112* (7), 4308-4327.
20. Webber, N. M.; Litvinenko, K. L.; Meech, S. R., Radiationless Relaxation in a Synthetic Analogue of the Green Fluorescent Protein Chromophore. *Journal of Physical Chemistry B* **2001,** *105* (33), 8036-8039.
21. Vengris, M.; van Stokkum, I. H. M.; He, X., et al., Ultrafast Excited and Ground-State Dynamics of the Green Fluorescent Protein Chromophore in Solution. *Journal of Physical Chemistry A* **2004,** *108* (21), 4587-4598.
22. van Thor, J. J., Photoreactions and Dynamics of the Green Fluorescent Protein. *Chemical Society Reviews* **2009,** *38* (10), 2935-2950.
23. Fang, C.; Frontiera, R. R.; Tran, R., et al., Mapping GFP Structure Evolution During Proton Transfer with Femtosecond Raman Spectroscopy. *Nature* **2009,** *462* (7270), 200-U74.
24. Henderson, J. N.; Osborn, M. F.; Koon, N., et al., Excited State Proton Transfer in the Red Fluorescent Protein mKeima. *Journal of the American Chemical Society* **2009,** *131* (37), 13212-+.
25. Piatkevich, K. D.; Hulit, J.; Subach, O. M., et al., Monomeric red fluorescent proteins with a large Stokes shift. *Proceedings of the National Academy of Sciences of the United States of America* **2010,** *107* (12), 5369-5374.
26. Lippincott-Schwartz, J.; Altan-Bonnet, N.; Patterson, G. H., Photobleaching and Photoactivation: Following Protein Dynamics in Living Cells. *Nature Reviews Molecular Cell Biology* **2003**, S7-S14.
27. Chudakov, D. M.; Belousov, V. V.; Zaraisky, A. G., et al., Kindling Fluorescent Proteins for Precise in vivo Photolabeling. *Nature Biotechnology* **2003,** *21* (2), 191-194.
28. van Thor, J. J.; Gensch, T.; Hellingwerf, K. J., et al., Phototransformation of Green Fluorescent Protein with UV and Visible Light Leads to Decarboxylation of Glutamate 222. *Nature Structural Biology* **2002,** *9* (1), 37-41.
29. Otto, H.; Hoersch, D.; Meyer, T. E., et al., Time-Resolved Single Tryptophan Fluorescence in Photoactive Yellow Protein Monitors Changes in the Chromophore Structure During the Photocycle via Energy Transfer. *Biochemistry* **2005,** *44* (51), 16804-16816.
30. Ihee, H.; Rajagopal, S.; Srajer, V., et al., Visualizing Reaction Pathways in Photoactive Yellow Protein from Nanoseconds to Seconds. *Proceedings of the*

National Academy of Sciences of the United States of America **2005,** *102* (20), 7145-7150.
31. Kandori, H.; Shichida, Y.; Yoshizawa, T., Photoisomerization in Rhodopsin. *Biochemistry-Moscow* **2001,** *66* (11), 1197-1209.
32. Kennis, J. T. M.; Larsen, D. S.; Ohta, K., et al., Ultrafast Protein Dynamics of Bacteriorhodopsin Probed by Photon Echo and Transient Absorption Spectroscopy. *Journal of Physical Chemistry B* **2002,** *106* (23), 6067-6080.
33. Ando, R.; Mizuno, H.; Miyawaki, A., Regulated Fast Nucleocytoplasmic Shuttling Observed by Reversible Protein Highlighting. *Science* **2004,** *306* (5700), 1370-1373.
34. Andresen, M.; Stiel, A. C.; Trowitzsch, S., et al., Structural Basis for Reversible Photoswitching in Dronpa. *Proceedings of the National Academy of Sciences of the United States of America* **2007,** *104* (32), 13005-13009.
35. Stiel, A. C.; Trowitzsch, S.; Weber, G., et al., 1.8 Angstrom Bright-State Structure of the Reversibly Switchable Fluorescent Protein Dronpa Guides the Generation of Fast Switching Variants. *Biochemical Journal* **2007,** *402*, 35-42.
36. Wilmann, P. G.; Turcic, K.; Battad, J. M., et al., The 1.7 Angstrom Crystal Structure of Dronpa: A Photoswitchable Green Fluorescent Protein. *J. Mol. Biol.* **2006,** *364* (2), 213-224.
37. Warren, M. M.; Kaucikas, M.; Fitzpatrick, A., et al., Ground-state proton transfer in the photoswitching reactions of the fluorescent protein Dronpa. *Nature Communications* **2013,** *4*.
38. Kao, Y.-T.; Zhu, X.; Min, W., Protein-flexibility mediated coupling between photoswitching kinetics and surrounding viscosity of a photochromic fluorescent protein. *Proceedings of the National Academy of Sciences of the United States of America* **2012,** *109* (9), 3220-3225.
39. Li, X.; Chung, L. W.; Mizuno, H., et al., Primary Events of Photodynamics in Reversible Photoswitching Fluorescent Protein Dronpa. *Journal of Physical Chemistry Letters* **2010,** *1* (23), 3328-3333.
40. Hofmann, M.; Eggeling, C.; Jakobs, S., et al., Breaking the Diffraction Barrier in Fluorescence Microscopy at Low Light Intensities by Using Reversibly Photoswitchable Proteins. *Proceedings of the National Academy of Sciences of the United States of America* **2005,** *102* (49), 17565-17569.
41. Rust, M. J.; Bates, M.; Zhuang, X., Sub-Diffraction-Limit Imaging by Stochastic Optical Reconstruction Microscopy (STORM). *Nature Methods* **2006,** *3* (10), 793-795.
42. Subach, F. V.; Patterson, G. H.; Manley, S., et al., Photoactivatable mCherry for High-Resolution Two-Color Fluorescence Microscopy. *Nature Methods* **2009,** *6* (2), 153-159.
43. Subach, F. V.; Patterson, G. H.; Renz, M., et al., Bright Monomeric Photoactivatable Red Fluorescent Protein for Two-Color Super-Resolution sptPALM of Live Cells. *Journal of the American Chemical Society* **2010,** *132* (18), 6481-6491.
44. Wang, L.; Jackson, W. C.; Steinbach, P. A., et al., Evolution of New Nonantibody Proteins via Iterative Somatic Hypermutation. *Proceedings of the National Academy of Sciences of the United States of America* **2004,** *101* (48), 16745-16749.

45. Abbyad, P.; Childs, W.; Shi, X., et al., Dynamic Stokes Shift in Green Fluorescent Protein Variants. *Proceedings of the National Academy of Sciences of the United States of America* **2007,** *104* (51), 20189-20194.
46. Shu, X.; Wang, L.; Colip, L., et al., Unique Interactions Between the Chromophore and Glutamate 16 Lead to Far-Red Emission in a Red Fluorescent Protein. *Protein Sci.* **2009,** *18* (2), 460-466.
47. Lin, M. Z.; McKeown, M. R.; Ng, H.-L., et al., Autofluorescent Proteins with Excitation in the Optical Window for Intravital Imaging in Mammals. *Chemistry & Biology* **2009,** *16* (11), 1169-1179.
48. Nienhaus, K.; Nar, H.; Heilker, R., et al., Trans-Cis Isomerization is Responsible for the Red-Shifted Fluorescence in Variants of the Red Fluorescent Protein eqFP611. *Journal of the American Chemical Society* **2008,** *130* (38), 12578-+.
49. Pletnev, S.; Pletneva, N. V.; Souslova, E. A., et al., Structural Basis for Bathochromic Shift of Fluorescence in Far-Red Fluorescent Proteins eqFP650 and eqFP670. *Acta Crystallographica Section D-Biological Crystallography* **2012,** *68*, 1088-1097.
50. Piatkevich, K. D.; Malashkevich, V. N.; Morozova, K. S., et al., Extended Stokes Shift in Fluorescent Proteins: Chromophore-Protein Interactions in a Near-Infrared TagRFP675 Variant. *Scientific Reports* **2013,** *3*.
51. Bakshiev, G., Universal Intermolecular Interactions and Their Effect on the Position of the Electronic Spectra of Molecules in Two-Component Solutions. *Optical Spectroscopy* **1964,** *16*, 446-451.
52. Ware, W. R.; Lee, S. K.; Brant, G. J., et al., Nanosecond Time-Resolved Emission Spectroscopy-Spectral Shifts due to Solvent-Excited Solute Relaxation. *Journal of Chemical Physics* **1971,** *54* (11), 4729-&.
53. Ware, W. R.; Chow, P.; Lee, S. K., Time-Resolved Nanosecond Emission Spectroscopy: Spectral Shift due to Solvent-Solute Relaxation. *Chemical Physics Letters* **1968,** *2* (6), 356-358.
54. Jimenez, R.; Fleming, G. R.; Kumar, P. V., et al., Femtosecond Solvation Dynamics of Water. *Nature* **1994,** *369* (6480), 471-473.
55. Pierce, D. W.; Boxer, S. G., Dielectric-Relaxation in a Protein Matrix. *Journal of Physical Chemistry* **1992,** *96* (13), 5560-5566.
56. Brand, L.; Gohlke, J. R., Nanosecond Time-Resolved Fluorescence Spectra of a Protein-Dye Complex. *Journal of Biological Chemistry* **1971,** *246* (7), 2317-&.
57. Stryer, L., Fluorescence Spectroscopy of Proteins. *Science* **1968,** *162* (3853), 526-&.
58. Bashkin, J. S.; McLendon, G.; Mukamel, S., et al., Influence of Medium Dynamics on Solvation and Charge Separation Reactions-Comparison of a Simple Alcohol And a Protein Solvent. *Journal of Physical Chemistry* **1990,** *94* (12), 4757-4761.
59. Frauenfelder, H.; Sligar, S. G.; Wolynes, P. G., The Energy Landscapes and Motions of Proteins. *Science* **1991,** *254* (5038), 1598-1603.
60. Frauenfelder, H.; Parak, F.; Young, R. D., Conformational Substates in Proteins. *Annual Review of Biophysics and Biophysical Chemistry* **1988,** *17*, 451-479.

61. Jones, C. M.; Henry, E. R.; Hu, Y., et al., Fast Events in Protein-Folding Initiated by Nanosecond Laser Photolysis. *Proceedings of the National Academy of Sciences of the United States of America* **1993,** *90* (24), 11860-11864.
62. Easter, J. H.; Brand, L., Nanosecond Time-Resolved Emission-Spectroscopy of a Fluorescence Probe Bound to L-Alpha-Egg Lecithin Vesicles. *Biochemical and Biophysical Research Communications* **1973,** *52* (3), 1086-1092.
63. Lakowicz, J. R.; Weber, G., Quenching of Protein Fluorescence by Oxygen-Detection of Structural Fluctuations in Proteins on Nanosecond Time Scale. *Biochemistry* **1973,** *12* (21), 4171-4179.
64. Loken, M. R.; Brand, L.; Hayes, J. W., et al., Excited-State Proton-Transfer as a Biological Probe-Determination of Rate Constants by Means of Nanosecond Fluorimetry. *Biochemistry* **1972,** *11* (25), 4779-&.
65. Frauenfelder, H.; McMahon, B. H.; Austin, R. H., et al., The Role of Structure, Energy Landscape, Dynamics, and Allostery in the Enzymatic Function of Myoglobin. *Proceedings of the National Academy of Sciences of the United States of America* **2001,** *98* (5), 2370-2374.
66. Jimenez, R.; Case, D. A.; Romesberg, F. E., Flexibility of an Antibody Binding Site Measured with Photon Echo Spectroscopy. *Journal of Physical Chemistry B* **2002,** *106* (5), 1090-1103.
67. Jimenez, R.; Salazar, G.; Baldridge, K. K., et al., Flexibility and Molecular Recognition in the Immune System. *Proceedings of the National Academy of Sciences of the United States of America* **2003,** *100* (1), 92-97.
68. Schoenlein, R. W.; Peteanu, L. A.; Mathies, R. A., et al., The 1st Step in Vision-Femtosecond Isomerization of Rhodopsin. *Science* **1991,** *254* (5030), 412-415.
69. Brixner, T.; Stenger, J.; Vaswani, H. M., et al., Two-Dimensional Spectroscopy of Electronic Couplings in Photosynthesis. *Nature* **2005,** *434* (7033), 625-628.
70. Kao, Y.-T.; Saxena, C.; Wang, L., et al., Femtochemistry in Enzyme Catalysis: DNA Photolyase. *Cell Biochemistry and Biophysics* **2007,** *48* (1), 32-44.
71. Chang, C.-W.; Guo, L.; Kao, Y.-T., et al., Ultrafast Solvation Dynamics at Binding and Active Sites of Photolyases. *Proceedings of the National Academy of Sciences of the United States of America* **2010,** *107* (7), 2914-2919.
72. Zhong, D. P.; Zewail, A. H., Femtosecond Dynamics of Flavoproteins: Charge Separation and Recombination in Riboflavine (Vitamin B-2)-Binding Protein and in Glucose Oxidase Enzyme. *Proceedings of the National Academy of Sciences of the United States of America* **2001,** *98* (21), 11867-11872.
73. Childs, W.; Boxer, S. G., Solvation Response along the Reaction Coordinate in the Active Site of Ketosteroid Isomerase. *Journal of the American Chemical Society* **2010,** *132* (18), 6474-6480.
74. Ansari, A.; Jones, C. M.; Henry, E. R., et al., Conformational Relaxation and Ligand-Binding in Myoglobin. *Biochemistry* **1994,** *33* (17), 5128-5145.
75. Ansari, A.; Berendzen, J.; Bowne, S. F., et al., Protein States and Protein Quakes. *Proceedings of the National Academy of Sciences of the United States of America* **1985,** *82* (15), 5000-5004.
76. Asaki, M. T.; Huang, C. P.; Garvey, D., et al., Generation of 11-fs Pulses from a Self-Mode-Locked Ti-Sapphire Laser. *Optics Letters* **1993,** *18* (12), 977-979.

77. Joo, T.; Jia, Y. W.; Fleming, G. R., Ti-Sapphire Regenerative Amplifier for Ultrashort High-Power Multikilohertz Pulses Without an External Stretcher. *Optics Letters* **1995,** *20* (4), 389-391.
78. Mukamel, S., *Principles of Nonlinear Optical Spectroscopy*. Oxford University Press: New York, NY, 1995.
79. Kong, Q.; Baudelet, F.; Han, J., et al., Microsecond Time-Resolved Energy-Dispersive EXAFS Measurement and its Application to Film the Thermolysis of (NH4)(2) PtCl6. *Scientific Reports* **2012,** *2*.
80. Chergui, M., Picosecond and Femtosecond X-ray Absorption Spectroscopy of Molecular Systems. *Acta Crystallographica Section A* **2010,** *66*, 229-239.
81. Ihee, H.; Lorenc, M.; Kim, T. K., et al., Ultrafast X-ray Diffraction of Transient Molecular Structures in Solution. *Science* **2005,** *309* (5738), 1223-1227.
82. Nibbering, E. T. J.; Fidder, H.; Pines, E., Ultrafast Chemistry: Using Time-Resolved Vibrational Spectroscopy for Interrogation of Structural Dynamics. *Annual Review of Physical Chemistry* **2005,** *56*, 337-367.
83. Mukamel, S., Femtosecond Optical Spectroscopy-A Direct Look at Elementary Chemical Events. *Annual Review of Physical Chemistry* **1990,** *41*, 647-681.
84. Shen, Y. R., Surface-Properties Probed by 2nd-Harmonic and Sum-Frequency Generation. *Nature* **1989,** *337* (6207), 519-525.
85. Nitzan, A., *Chemical Dynamics in Condensed Phases: Relaxation Transfer, and Reactions in Condensed Molecular Systems*. Oxford University Press: New York, NY, 2014.
86. Belabas, N.; Jonas, D. M., Three-dimensional View of Signal Propagation in Femtosecond Four-Wave Mixing with Application to the Boxcars Geometry. *Journal of the Optical Society of America B-Optical Physics* **2005,** *22* (3), 655-674.
87. Bloch, F., Nuclear Induction. *Physical Review* **1946,** *70* (7-8), 460-474.
88. Kubo, M., A Stochastic Theory of Line Shape. *Advances in Chemical Physics* **1969,** *15*, 101-127.
89. Li, B. L.; Johnson, A. E.; Mukamel, S., et al., The Brownian Oscillator Model for Solvation Effects in Spontaneous Light-Emission and Their Relationship to Electron-Transfer. *Journal of the American Chemical Society* **1994,** *116* (24), 11039-11047.
90. Stock, G.; Domcke, W., Detection of Ultrafaset Molecular-Excited-State Dynamics with Time-Resolved and Frequency-Resolved Pump-Probe Spectroscopy. *Physical Review A* **1992,** *45* (5), 3032-3040.
91. Park, J. S.; Joo, T., Nuclear Dynamics in Electronic Ground and Excited States Probed by Spectrally Resolved Four Wave Mixing. *Journal of Chemical Physics* **2002,** *116* (24), 10801-10808.
92. Joo, T. H.; Jia, Y. W.; Yu, J. Y., et al., Third-Order Nonlinear Time Domain Probes of Solvation Dynamics. *Journal of Chemical Physics* **1996,** *104* (16), 6089-6108.
93. Hahn, E. L., Spin Echoes. *Physical Review* **1950,** *80* (4), 580-594.
94. Igumenova, T. I.; Frederick, K. K.; Wand, A. J., Characterization of the Fast Dynamics of Protein Amino Acid Side Chains Using NMR Relaxation in Solution. *Chemical Reviews* **2006,** *106* (5), 1672-1699.
95. Boehr, D. D.; McElheny, D.; Dyson, H. J., et al., The Dynamic Energy Landscape of Dihydrofolate Reductase Catalysis. *Science* **2006,** *313* (5793), 1638-1642.

96. Hybl, J. D.; Albrecht, A. W.; Faeder, S. M. G., et al., Two-Dimensional Electronic Spectroscopy. *Chemical Physics Letters* **1998,** *297* (3-4), 307-313.
97. Khalil, M.; Demirdoven, N.; Tokmakoff, A., Coherent 2D IR Spectroscopy: Molecular Structure and Dynamics in Solution. *Journal of Physical Chemistry A* **2003,** *107* (27), 5258-5279.
98. West, B. A.; Moran, A. M., Two-Dimensional Electronic Spectroscopy in the Ultraviolet Wavelength Range. *Journal of Physical Chemistry Letters* **2012,** *3* (18), 2575-2581.
99. Kinrot, O.; Prior, Y., 4-Wave-Mixing in Optically Dense Media. *Physical Review A* **1994,** *50* (3), R1999-R2002.
100. Abella, I. D.; Kurnit, N. A.; Hartmann, S. R., Photon Echoes. *Physical Review* **1966,** *141* (1), 391-&.
101. Cho, M. H.; Yu, J. Y.; Joo, T. H., et al., The Integrated Photon Echo and Solvation Dynamics. *Journal of Physical Chemistry* **1996,** *100* (29), 11944-11953.
102. Zanni, P. H. M., *Concepts and Methods of 2D Infrared Spectroscopy*. Cambridge University Press: New York, NY, 2011.
103. Bax, A., Two-Dimensional NMR and Protein-Structure. *Annual Review of Biochemistry* **1989,** *58*, 223-256.
104. Bagchi, S.; Thorpe, D. G.; Thorpe, I. F., et al., Conformational Switching between Protein Substates Studied with 2D IR Vibrational Echo Spectroscopy and Molecular Dynamics Simulations. *Journal of Physical Chemistry B* **2010,** *114* (51), 17187-17193.
105. Thielges, M. C.; Fayer, M. D., Protein Dynamics Studied with Ultrafast Two-Dimensional Infrared Vibrational Echo Spectroscopy. *Accounts of Chemical Research* **2012,** *45* (11), 1866-1874.
106. Bristow, A. D.; Karaiskaj, D.; Dai, X., et al., A Versatile Ultrastable Platform for Optical Multidimensional Fourier-Transform Spectroscopy. *Review of Scientific Instruments* **2009,** *80* (7).
107. Brixner, T.; Mancal, T.; Stiopkin, I. V., et al., Phase-Stabilized Two-Dimensional Electronic Spectroscopy. *Journal of Chemical Physics* **2004,** *121* (9), 4221-4236.
108. Fuller, F. D.; Wilcox, D. E.; Ogilvie, J. P., Pulse Shaping Based Two-Dimensional Electronic Spectroscopy in a Background Free Geometry. *Optics Express* **2014,** *22* (1), 1018-1027.
109. Cowan, M. L.; Ogilvie, J. P.; Miller, R. J. D., Two-Dimensional Spectroscopy Using Diffractive Optics Based Phased-Locked Photon Echoes. *Chemical Physics Letters* **2004,** *386* (1-3), 184-189.
110. Jonas, D. M., Two-Dimensional Femtosecond Spectroscopy. *Annual Review of Physical Chemistry* **2003,** *54*, 425-463.
111. Hybl, J. D.; Ferro, A. A.; Jonas, D. M., Two-Dimensional Fourier Transform Electronic Spectroscopy. *Journal of Chemical Physics* **2001,** *115* (14), 6606-6622.
112. Siemens, M. E.; Moody, G.; Li, H. B., et al., Resonance Lineshapes in Two-Dimensional Fourier Transform Spectroscopy. *Optics Express* **2010,** *18* (17), 17699-17708.

113. Fayer, M. D., Dynamics of Liquids, Molecules, and Proteins Measured with Ultrafast 2D IR Vibrational Echo Chemical Exchange Spectroscopy. In *Annual Review of Physical Chemistry*, 2009; Vol. 60, pp 21-38.
114. Backus, S.; Durfee, C. G.; Murnane, M. M., et al., High Power Ultrafast Lasers. *Review of Scientific Instruments* **1998,** *69* (3), 1207-1223.
115. Moulton, P. F., Spectroscopic and Laser Characteristics of Ti-Al2O3. *Journal of the Optical Society of America B-Optical Physics* **1986,** *3* (1), 125-133.
116. Scully, M. O.; Lamb, W. E., Quantum Theory of an Optical Maser .I. General Theory. *Physical Review* **1967,** *159* (2), 208-&.
117. Keller, U.; Weingarten, K. J.; Kartner, F. X., et al., Semiconductor Saturable Absorber Mirrors (SESAM's) for Femtosecond to Nanosecond Pulse Generation in Solid-State Lasers. *Ieee Journal of Selected Topics in Quantum Electronics* **1996,** *2* (3), 435-453.
118. Rundquist, A.; Durfee, C.; Chang, Z., et al., Ultrafast Laser and Amplifier Sources. *Applied Physics B-Lasers and Optics* **1997,** *65* (2), 161-174.
119. Yamakawa, K.; Magana, A.; Chiu, P. H., Tunable Ti-Sapphire Regenerative Amplifier for Femtosecond Chirped-Pulse Amplification. *Applied Physics B-Lasers and Optics* **1994,** *58* (4), 323-326.
120. Gibson, E. A.; Gaudiosi, D. M.; Kapteyn, H. C., et al., Efficient Reflection Grisms for Pulse Compression and Dispersion Compensation of Femtosecond Pulses. *Optics Letters* **2006,** *31* (22), 3363-3365.
121. Gaudiosi, D. M.; Gagnon, E.; Lytle, A. L., et al., Multi-Kilohertz Repetition Rate Ti : Sapphire Amplifier Based on Down-Chirped Pulse Amplification. *Optics Express* **2006,** *14* (20), 9277-9283.
122. Nikogosyan, D. N., Beta-Barium Borate (BBO)-A Review of Its Properties and Applications. *Applied Physics a-Materials Science & Processing* **1991,** *52* (6), 359-368.
123. Eimerl, D.; Davis, L.; Velsko, S., et al., Optical, Mechanical, and Thermal-Properties of Barium Borate. *J. Appl. Phys.* **1987,** *62* (5), 1968-1983.
124. Cerullo, G.; De Silvestri, S., Ultrafast Optical Parametric Amplifiers. *Review of Scientific Instruments* **2003,** *74* (1), 1-18.
125. Tekavec, P. F.; Myers, J. A.; Lewis, K. L. M., et al., Effects of Chirp on Two-Dimensional Fourier Transform Electronic Spectra. *Optics Express* **2010,** *18* (11), 11015-11024.
126. Fork, R. L.; Martinez, O. E.; Gordon, J. P., Negative Dispersion Using Pairs of Prisms. *Optics Letters* **1984,** *9* (5), 150-152.
127. Fork, R. L.; Cruz, C. H. B.; Becker, P. C., et al., Compression of Optical Puleses to 6 Femtosecons by Using Cubic Phase Compensation. *Optics Letters* **1987,** *12* (7), 483-485.
128. Baum, P.; Breuer, M.; Riedle, E., et al., Brewster-Angled Chirped Mirrors for Broadband Pulse Compression Without Dispersion Oscillations. *Optics Letters* **2006,** *31* (14), 2220-2222.
129. Trebino, R., *Frequency-Resolved Optical Gating: The Measurement of Ultrashort Laser Pulses*. Kluwer Academic Publishers: Norwell, Massachusetts, 2002.
130. Trebino, R.; DeLong, K. W.; Fittinghoff, D. N., et al., Measuring Ultrashort Laser Pulses in the Time-Frequency Domain Using Frequency-Resolved Optical Gating. *Review of Scientific Instruments* **1997,** *68* (9), 3277-3295.

131. Weiner, A. M., Femtosecond Pulse Shaping Using Spatial Light Modulators. *Review of Scientific Instruments* **2000,** *71* (5), 1929-1960.
132. Wilson, J. W.; Schlup, P.; Bartels, R. A., Ultrafast Phase and Amplitude Pulse Shaping with a Single, One-Dimensional, High-Resolution Phase Mask. *Optics Express* **2007,** *15* (14), 8979-8987.
133. Shim, S.-H.; Strasfeld, D. B.; Zanni, M. T., Generation and Characterization of Phase and Amplitude Shaped Femtosecond Mid-IR Pulses. *Optics Express* **2006,** *14* (26), 13120-13130.
134. Weiner, A. M., Ultrafast Optical Pulse Shaping: A Tutorial Review. *Optics Communications* **2011,** *284* (15), 3669-3692.
135. Grumstrup, E. M.; Shim, S.-H.; Montgomery, M. A., et al., Facile Collection of Two-Dimensional Electronic Spectra Using Femtosecond Pulse-Shaping Technology. *Optics Express* **2007,** *15* (25), 16681-16689.
136. Shim, S.-H.; Zanni, M. T., How to Turn Your Pump-Probe Instrument Into a Multidimensional Spectrometer: 2D IR and Vis Spectroscopies via Pulse Shaping. *Physical Chemistry Chemical Physics* **2009,** *11* (5), 748-761.
137. Gundogdu, K.; Stone, K. W.; Turner, D. B., et al., Multidimensional Coherent Spectroscopy Made Easy. *Chemical Physics* **2007,** *341* (1-3), 89-94.
138. Grumstrup, E. M.; Damrauer, N. H., Modeling and Correction of Distorted Two-Dimensional Fourier Transform Spectra from Pixelated Pulse Shaping Devices. *Optics Express* **2012,** *20* (19), 20908-U1308.
139. Faeder, S. M. G.; Jonas, D. M., Two-Dimensional Electronic Correlation and Relaxation Spectra: Theory and Model Calculations. *Journal of Physical Chemistry A* **1999,** *103* (49), 10489-10505.
140. Backus, E. H. G.; Garrett-Roe, S.; Hamm, P., Phasing Problem of Heterodyne-Detected Two-Dimensional Infrared Spectroscopy. *Optics Letters* **2008,** *33* (22), 2665-2667.
141. Bristow, A. D.; Karaiskaj, D.; Dai, X., et al., All-Optical Retrieval of the Global Phase for Two-Dimensional Fourier-Transform Spectroscopy. *Optics Express* **2008,** *16* (22), 18017-18027.
142. Lang, M. J.; Jordanides, X. J.; Song, X., et al., Aqueous solvation dynamics studied by photon echo spectroscopy. *Journal of Chemical Physics* **1999,** *110* (12), 5884-5892.
143. Jordanides, X. J.; Lang, M. J.; Song, X. Y., et al., Solvation dynamics in protein environments studied by photon echo spectroscopy. *Journal of Physical Chemistry B* **1999,** *103* (37), 7995-8005.
144. Gibson, E. A.; Shen, Z.; Jimenez, R., Three-Pulse Photon Echo Peak Shift Spectroscopy as a Probe of Flexibility and Conformational Heterogeneity in Protein Folding. *Chemical Physics Letters* **2009,** *473* (4-6), 330-335.
145. Fayer, M. D., *Ultrafast Infrared Vibrational Spectroscopy*. CRC Press: Boca Raton, FL, 2013.
146. Dean, K. M.; Lubbeck, J. L.; Binder, J. K., et al., Analysis of Red-Fluorescent Proteins Provides Insight into Dark-State Conversion and Photodegradation. *Biophysical Journal* **2011,** *101* (4), 961-969.

147. Chudakov, D. M.; Matz, M. V.; Lukyanov, S., et al., Fluorescent Proteins and Their Applications in Imaging Living Cells and Tissues. *Physiological Reviews* **2010,** *90* (3), 1103-1163.
148. List, N. H.; Olsen, J. M. H.; Jensen, H. J. A., et al., Molecular-Level Insight into the Spectral Tuning Mechanism of the DsRed Chromophore. *Journal of Physical Chemistry Letters* **2012,** *3* (23), 3513-3521.
149. Hasegawa, J.; Ise, T.; Fujimoto, K. J., et al., Excited States of Fluorescent Proteins, mKO and DsRed: Chromophore-Protein Electrostatic Interaction Behind the Color Variations. *Journal of Physical Chemistry B* **2010,** *114* (8), 2971-2979.
150. de Boeij, W. P.; Pshenichnikov, M. S.; Wiersma, D. A., Ultrafast solvation dynamics explored by femtosecond photon echo spectroscopies. *Annual Review of Physical Chemistry* **1998,** *49*, 99-123.
151. Fayer, M. D., Fast Protein Dynamics Probed with Infrared Vibrational Echo Experiments. *Annual Review of Physical Chemistry* **2001,** *52*, 315-356.
152. Lee, S. H.; Park, J. S.; Joo, T., Frequency-Time-Resolved Four-Wave Mixing of a Dye Molecule in Liquid. *Journal of Physical Chemistry A* **2000,** *104* (30), 6917-6923.
153. Phillips, J. C.; Braun, R.; Wang, W., et al., Scalable Molecular Dynamics with NAMD. *Journal of Computational Chemistry* **2005,** *26* (16), 1781-1802.
154. Brooks, B. R.; Bruccoleri, R. E.; Olafson, B. D., et al., CHARMM - A Program for Macromolecular Energy, Minimization and Dynamics Calculations. *Journal of Computational Chemistry* **1983,** *4* (2), 187-217.
155. Reuter, N.; Lin, H.; Thiel, W., Green Fluorescent Proteins: Empirical Force Field for the Neutral and Deprotonated Forms of the Chromophore: Molecular Dynamics Simulations of the Wild Type and S65T Mutant. *Journal of Physical Chemistry B* **2002,** *106* (24), 6310-6321.
156. Humphrey, W.; Dalke, A.; Schulten, K., VMD: Visual Molecular Dynamics. *Journal of Molecular Graphics & Modelling* **1996,** *14* (1), 33-38.
157. Essmann, U.; Perera, L.; Berkowitz, M. L., et al., A Smooth Particle Mesh Ewald Method. *Journal of Chemical Physics* **1995,** *103* (19), 8577-8593.
158. Sugisaki, M.; Fujiwara, M.; Nair, S. V., et al., Excitation-Energy Dependence of Transient Grating Spectroscopy in Beta-Carotene. *Physical Review B* **2009,** *80* (3).
159. Hendrix, J.; Flors, C.; Dedecker, P., et al., Dark States in Monomeric Red Fluorescent Proteins Studied by Fluorescence Correlation and Single Molecule Spectroscopy. *Biophysical Journal* **2008,** *94* (10), 4103-4113.
160. Elber, R.; Karplus, M., Multiple Conformational States of Proteins-A Molecular-Dynamics Analysis of Myoglobin. *Science* **1987,** *235* (4786), 318-321.
161. Swiatla-Wojcik, D., Evaluation of the Criteria of Hydrogen Bonding in Highly Associated Liquids. *Chemical Physics* **2007,** *342* (1-3), 260-266.
162. Kumar, P. V.; Maroncelli, M., Polar Solvation Dynamics of Polyatomic Solutes-Simulations Studies in Acetonitrile and Methanol. *Journal of Chemical Physics* **1995,** *103* (8), 3038-3060.
163. Pal, S. K.; Peon, J.; Bagchi, B., et al., Biological Water: Femtosecond Dynamics of Macromolecular Hydration. *Journal of Physical Chemistry B* **2002,** *106* (48), 12376-12395.
164. Halle, B.; Nilsson, L., Does the Dynamic Stokes Shift Report on Slow Protein Hydration Dynamics? *Journal of Physical Chemistry B* **2009,** *113* (24), 8210-8213.

165. Xu, Y.; Gnanasekaran, R.; Leitner, D. M., The Dielectric Response to Photoexcitation of GFP: A Molecular Dynamics Study. *Chemical Physics Letters* **2013,** *564*, 78-82.
166. Morozova, K. S.; Piatkevich, K. D.; Gould, T. J., et al., Far-Red Fluorescent Protein Excitable with Red Lasers for Flow Cytometry and Superresolution STED Nanoscopy. *Biophysical Journal* **2010,** *99* (2), L13-L15.
167. Chu, J.; Haynes, R. D.; Corbel, S. Y., et al., Non-Invasive Intravital Imaging of Cellular Differentiation with a Bright Red-excitable Fluorescent Protein. *Nature Methods* **2014,** *11* (5), 572-578.
168. Konold, P.; Regmi, C. K.; Chapagain, P. P., et al., Hydrogen Bond Flexibility Correlates with Stokes Shift in mPlum Variants. *The Journal of Physical Chemistry B* **2014,** *118* (11), 2940-8.
169. Haupts, U.; Maiti, S.; Schwille, P., et al., Dynamics of Fluorescence Fluctuations in Green Fluorescent Protein Observed by Fluorescence Correlation Spectroscopy. *Proceedings of the National Academy of Sciences of the United States of America* **1998,** *95* (23), 13573-13578.
170. van Thor, J. J.; Sage, J. T., Charge Transfer in Green Fluorescent Protein. *Photochemical & Photobiological Sciences* **2006,** *5* (6), 597-602.
171. Mudalige, K.; Habuchi, S.; Goodwin, P. M., et al., Photophysics of the Red Chromophore of HcRed: Evidence for Cis-Trans Isomerization and Protonation-State Changes. *Journal of Physical Chemistry B* **2010,** *114* (13), 4678-4685.
172. Xu, C.; Zipfel, W.; Shear, J. B., et al., Multiphoton Fluorescence Excitation: New Spectral Windows for Biological Nonlinear Microscopy. *Proceedings of the National Academy of Sciences of the United States of America* **1996,** *93* (20), 10763-10768.
173. Drobizhev, M.; Tillo, S.; Makarov, N. S., et al., Color Hues in Fluorescent Proteins with the Same Chromophore are due to Internal Quadratic Stark Effect. *Biophysical Journal* **2010,** *98* (3), 413A-413A.
174. Grigorenko, B. L.; Nemukhin, A. V.; Polyakov, I. V., et al., Triple-Decker Motif for Red-Shifted Fluorescent Protein Mutants. *Journal of Physical Chemistry Letters* **2013,** *4* (10), 1743-1747.
175. Drobizhev, M.; Makarov, N. S.; Tillo, S. E., et al., Two-Photon Absorption Properties of Fluorescent Proteins. *Nature Methods* **2011,** *8* (5), 393-399.
176. Drobizhev, M.; Tillo, S.; Makarov, N. S., et al., Absolute Two-Photon Absorption Spectra and Two-Photon Brightness of Orange and Red Fluorescent Proteins. *Journal of Physical Chemistry B* **2009,** *113* (4), 855-859.
177. Drobizhev, M.; Makarov, N. S.; Tillo, S. E., et al., Describing Two-Photon Absorptivity of Fluorescent Proteins with a New Vibronic Coupling Mechanism. *Journal of Physical Chemistry B* **2012,** *116* (5), 1736-1744.
178. Vegh, R. B.; Bravaya, K. B.; Bloch, D. A., et al., Chromophore Photoreduction in Red Fluorescent Proteins is Responsible for Bleaching and Phototoxicity. *Journal of Physical Chemistry B* **2014,** *118* (17), 4527-4534.
179. Nemeth, A.; Milota, F.; Mancal, T., et al., Double-Quantum Two-Dimensional Electronic Spectroscopy of a Three-Level System: Experiments and Simulations. *Journal of Chemical Physics* **2010,** *133* (9).
180. Fulmer, E. C.; Mukherjee, P.; Krummel, A. T., et al., A Pulse Sequence for Directly Measuring the Anharmonicities of Coupled Vibrations: Two-Quantum Two-

Dimensional Infrared Spectroscopy. *Journal of Chemical Physics* **2004,** *120* (17), 8067-8078.
181. Stone, K. W.; Gundogdu, K.; Turner, D. B., et al., Two-Quantum 2D FT Electronic Spectroscopy of Biexcitons in GaAs Quantum Wells. *Science* **2009,** *324* (5931), 1169-1173.
182. Karaiskaj, D.; Bristow, A. D.; Yang, L., et al., Two-Quantum Many-Body Coherences in Two-Dimensional Fourier-Transform Spectra of Exciton Resonances in Semiconductor Quantum Wells. *Physical Review Letters* **2010,** *104* (11).
183. Kim, J.; Mukamel, S.; Scholes, G. D., Two-Dimensional Electronic Double-Quantum Coherence Spectroscopy. *Accounts of Chemical Research* **2009,** *42* (9), 1375-1384.
184. Dai, X.; Richter, M.; Li, H., et al., Two-Dimensional Double-Quantum Spectra Reveal Collective Resonances in an Atomic Vapor. *Physical Review Letters* **2012,** *108* (19).
185. Christensson, N.; Milota, F.; Nemeth, A., et al., Electronic Double-Quantum Coherences and Their Impact on Ultrafast Spectroscopy: The Example of beta-Carotene. *Journal of Physical Chemistry Letters* **2010,** *1* (23), 3366-3370.
186. Fingerhut, B. P.; Richter, M.; Luo, J.-W., et al., Dissecting Biexciton Wave Functions of Self-Assembled Quantum Dots by Double-Quantum-Coherence Optical Spectroscopy. *Physical Review B* **2012,** *86* (23).
187. Mukamel, S.; Oszwaldowski, R.; Yang, L., A Coherent Nonlinear Optical Signal Induced by Electron Correlations. *Journal of Chemical Physics* **2007,** *127* (22).
188. Shaner, N. C.; Lin, M. Z.; McKeown, M. R., et al., Improving the photostability of bright monomeric orange and red fluorescent proteins. *Nature Methods* **2008,** *5* (6), 545-551.
189. Pletnev, S.; Shcherbo, D.; Chudakov, D. M., et al., A Crystallographic Study of Bright Far-Red Fluorescent Protein mKate Reveals pH-induced cis-trans Isomerization of the Chromophore. *Journal of Biological Chemistry* **2008,** *283* (43), 28980-28987.
190. Kim, J.; Huxter, V. M.; Curutchet, C., et al., Measurement of Electron-Electron Interactions and Correlations Using Two-Dimensional Electronic Double-Quantum Coherence Spectroscopy. *Journal of Physical Chemistry A* **2009,** *113* (44), 12122-12133.
191. Nifosi, R.; Luo, Y., Predictions of Novel Two-Photon Absorption Bands in Fluorescent Proteins. *Journal of Physical Chemistry B* **2007,** *111* (50), 14043-14050.
192. Taguchi, N.; Mochizuki, Y.; Nakano, T., et al., Fragment Molecular Orbital Calculations on Red Fluorescent Proteins (DsRed and mFruits). *Journal of Physical Chemistry B* **2009,** *113* (4), 1153-1161.
193. Stiel, A. C.; Andresen, M.; Bock, H., et al., Generation of Monomeric Reversibly Switchable Red Fluorescent Proteins for Far-Field Fluorescence Nanoscopy. *Biophysical Journal* **2008,** *95* (6), 2989-2997.
194. Senn, H. M.; Thiel, W., QM/MM Methods for Biomolecular Systems. *Angewandte Chemie-International Edition* **2009,** *48* (7), 1198-1229.

Appendix

A. Data Acquisition Software

Labview Software Programs

2DFTS_scan_DQC.vi

MoveStages.vi

View CCD.vi

TG-FROG.vi

Collect Mightex image and bin.vi

pulse overlap webcam Mightex.vi

PumpProbeDiagnostics.vi

B. Data Processing Software

Matlab (Mathworks) was the primary software program used to process experimental data. Several scripts were written for each individual experiment. The mathematical conversions within these scripts are represented in the flow charts below. Note: Since the functional forms evolved slightly over the course of this project and the names were not chronological, the most recent versions, and presumably most comprehensive, are documented here.

Transient Grating FROG

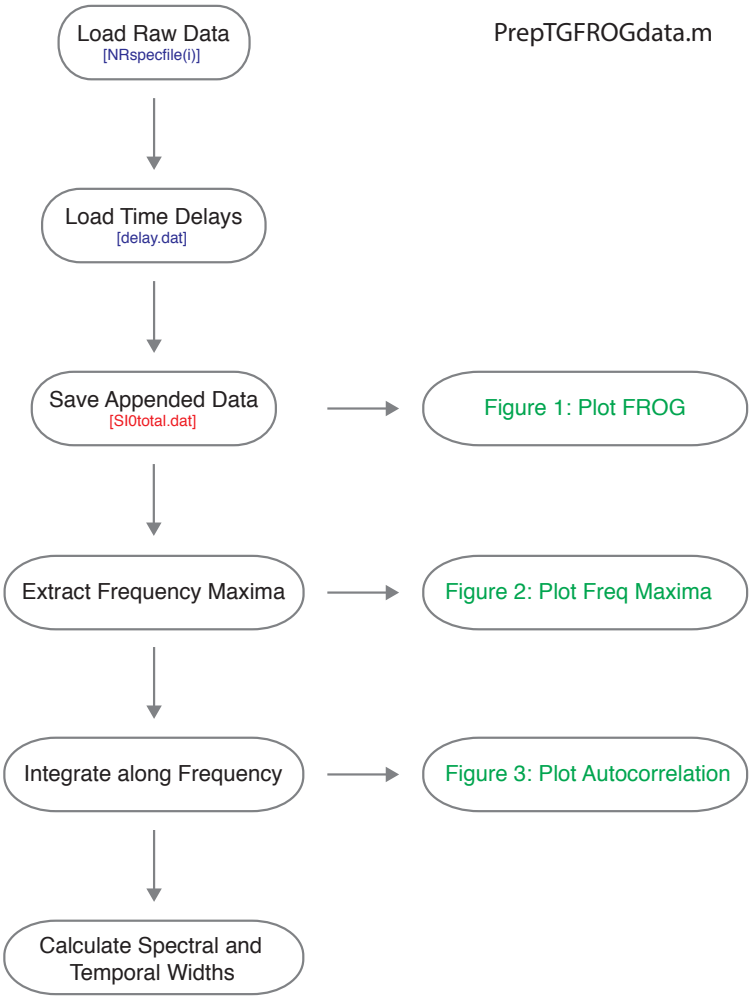

Spectrally Resolved Transient Grating

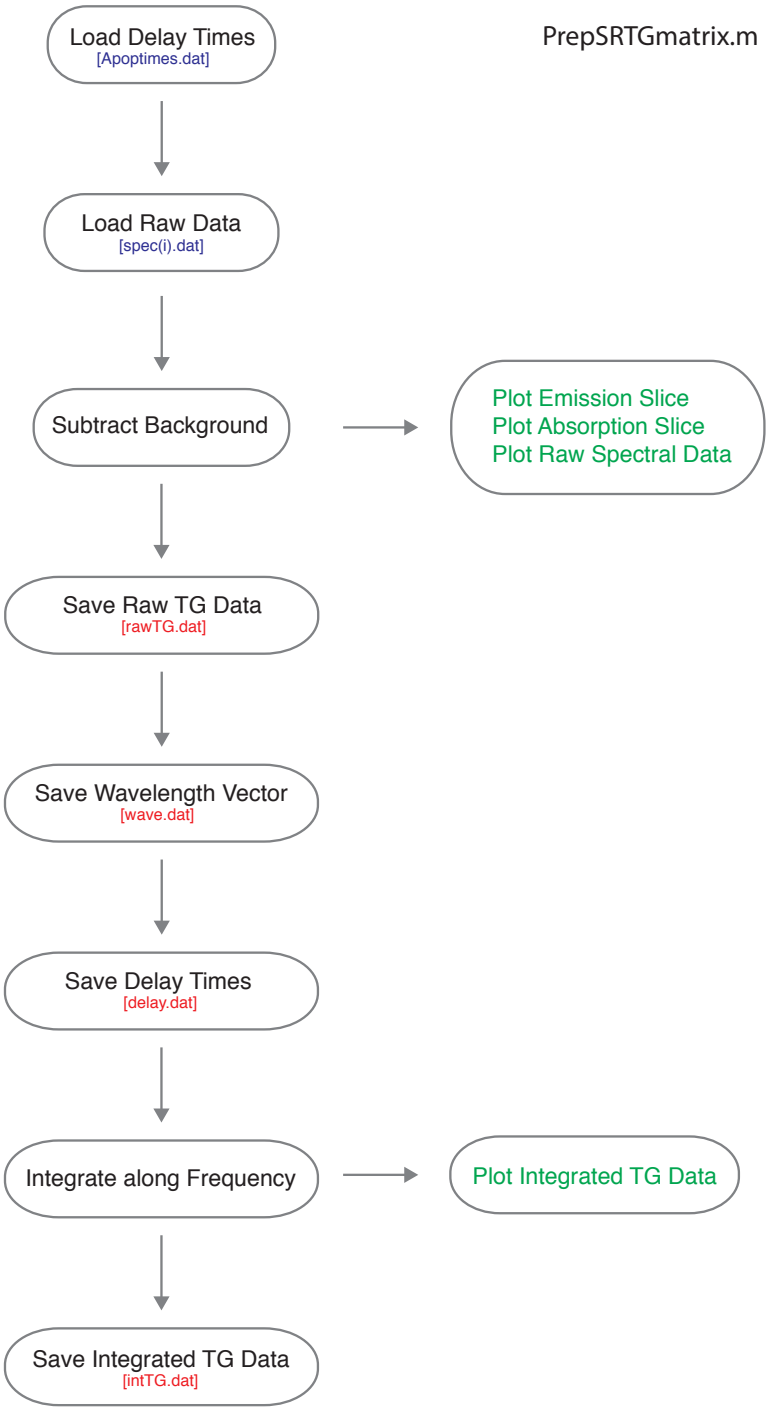

averageSRTGdata.m

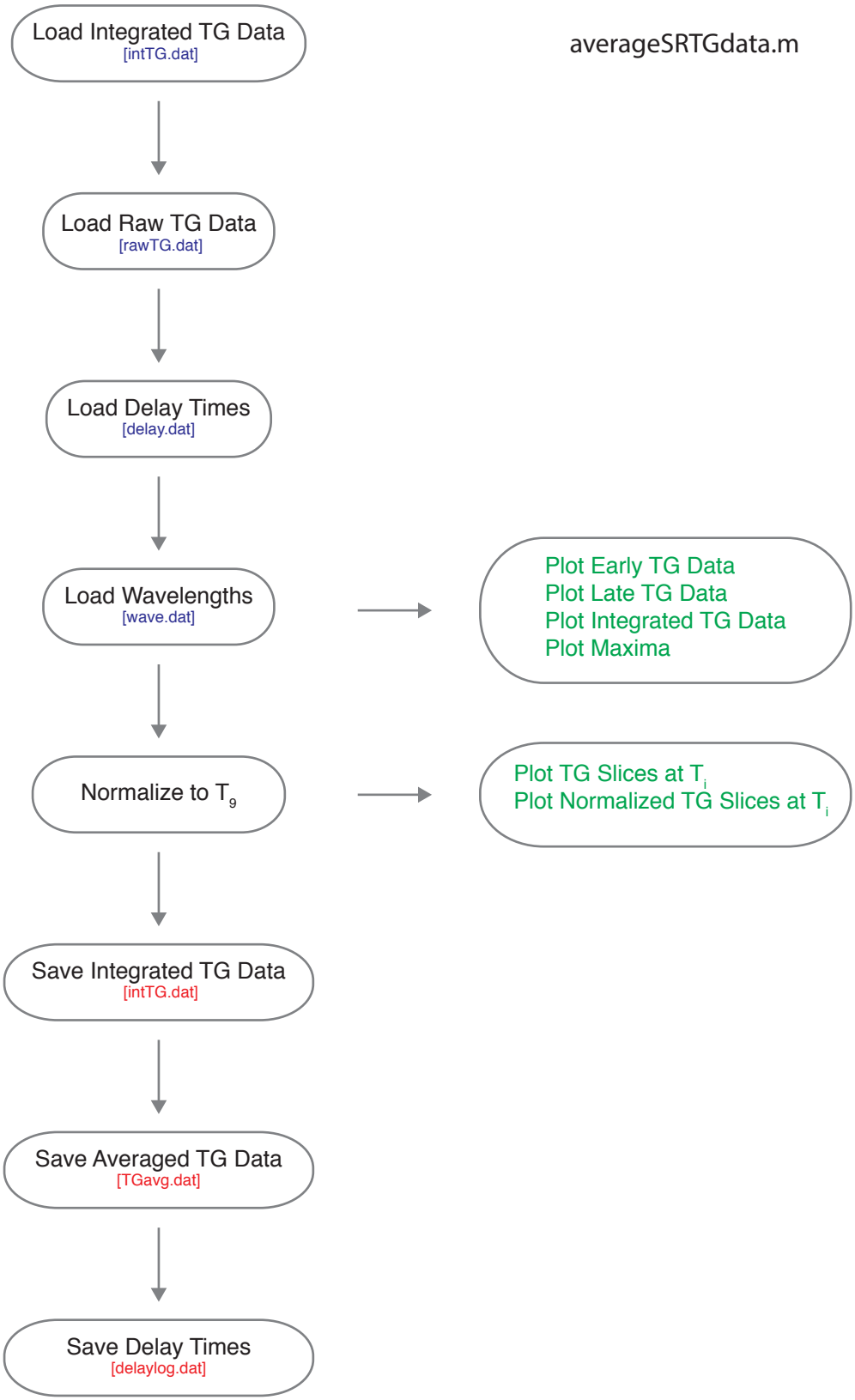

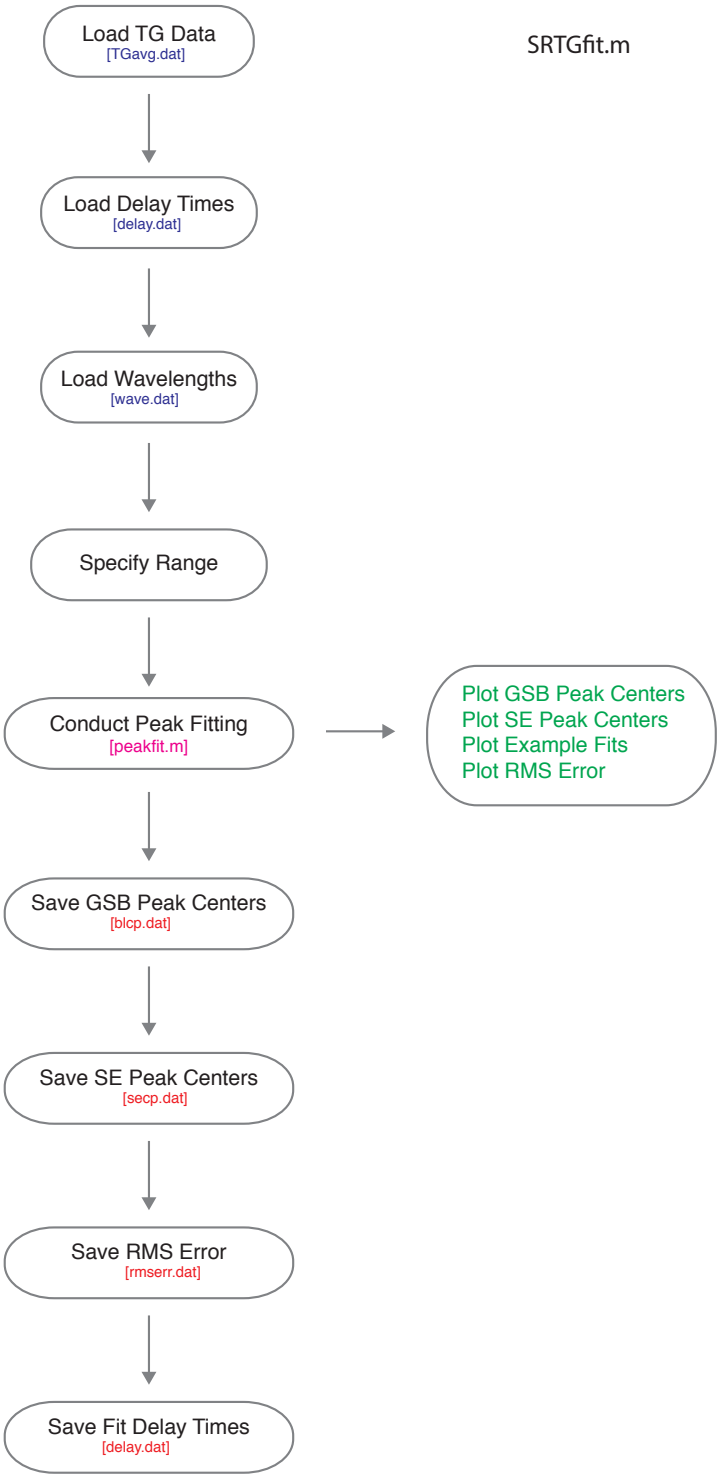
SRTGfit.m
Load TG Data
[TGavg.dat]
Load Delay Times
[delay.dat]
Load Wavelengths
[wave.dat]
Specify Range
Conduct Peak Fitting
[peakfit.m]
Plot GSB Peak Centers
Plot SE Peak Centers
Plot Example Fits
Plot RMS Error
Save GSB Peak Centers
[blcp.dat]
Save SE Peak Centers
[secp.dat]
Save RMS Error
[rmserr.dat]
Save Fit Delay Times
[delay.dat]

2D Fourier Transform Spectroscopy

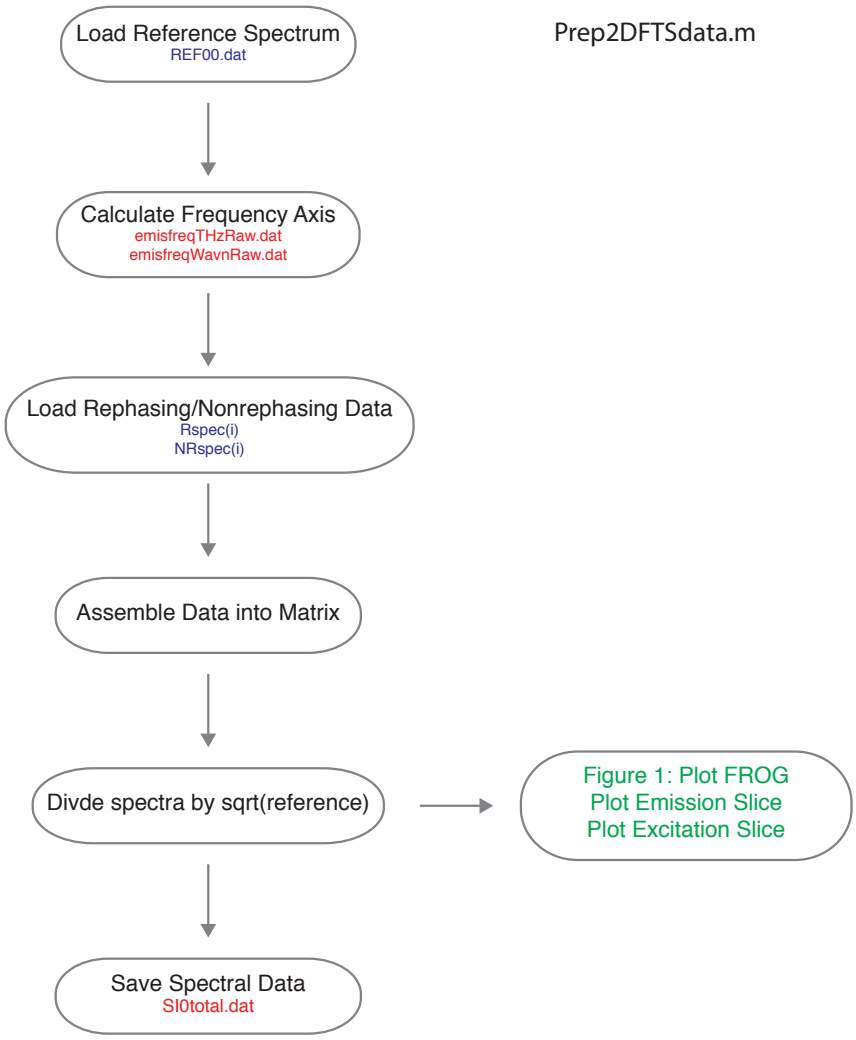

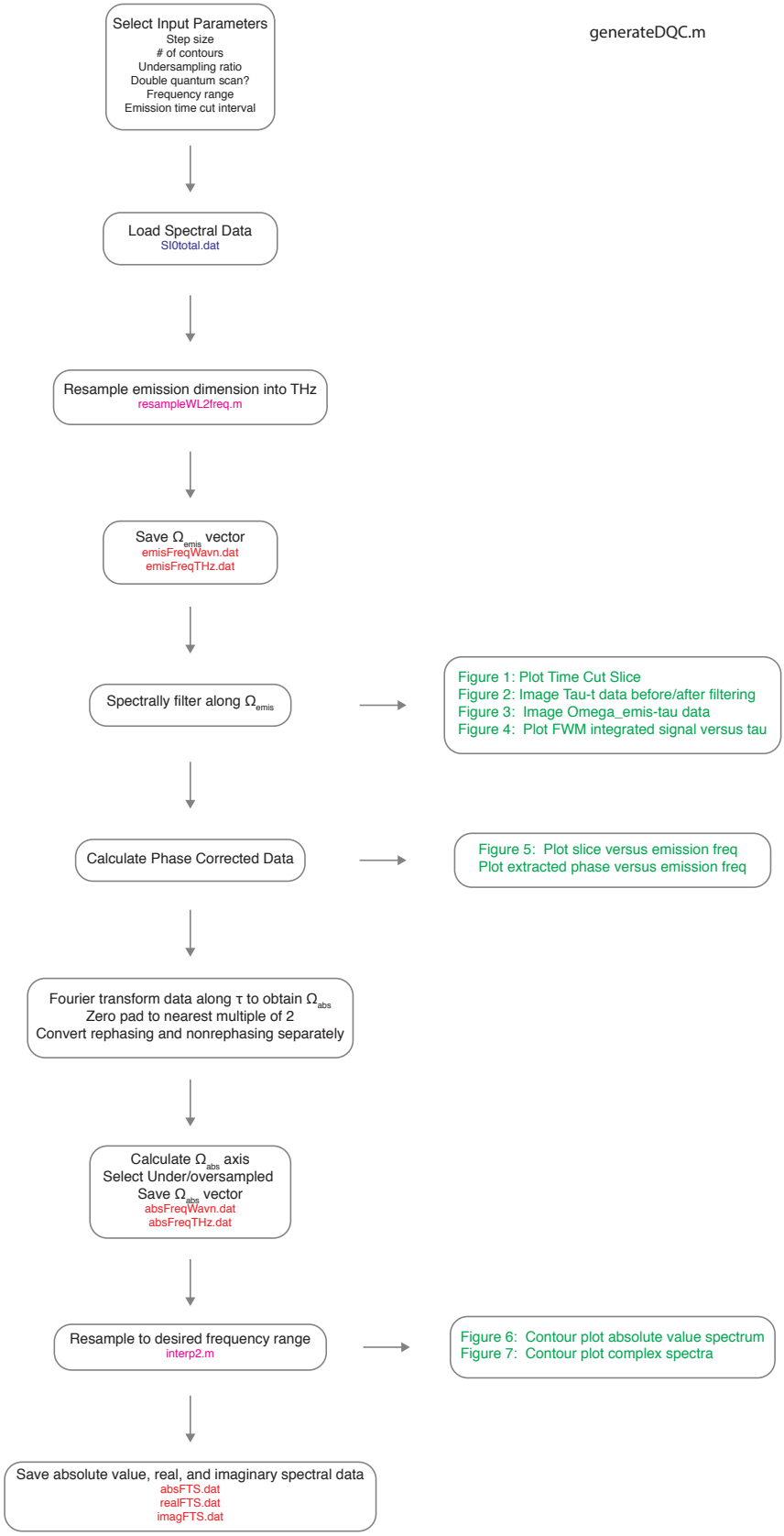
generateDQC.m
Select Input Parameters
Step size
# of contours
Undersampling ratio
Double quantum scan?
Frequency range
Emission time cut interval
Load Spectral Data
SI0total.dat
Resample emission dimension into THz
resampleWL2freq.m
Save Ωemis vector
emisFreqWavn.dat
emisFreqTHz.dat
Spectrally filter along Ωemis
Figure 1: Plot Time Cut Slice
Figure 2: Image Tau-t data before/after filtering
Figure 3: Image Omega_emis-tau data
Figure 4: Plot FWM integrated signal versus tau
Calculate Phase Corrected Data
Figure 5: Plot slice versus emission freq
Plot extracted phase versus emission freq
Fourier transform data along τ to obtain Ωabs
Zero pad to nearest multiple of 2
Convert rephasing and nonrephasing separately
Calculate Ωabs axis
Select Under/oversampled
Save Ωabs vector
absFreqWavn.dat
absFreqTHz.dat
Resample to desired frequency range
interp2.m
Figure 6: Contour plot absolute value spectrum
Figure 7: Contour plot complex spectra
Save absolute value, real, and imaginary spectral data
absFTS.dat
realFTS.dat
imagFTS.dat

C. Data Modeling Software

Spectron 2.8

The modeled 2Q2D data presented in Chapter V were calculated using the Spectron 2.8 software program. This program was developed by the research group of Shaul Mukamel with the intent of providing a universal package for conducting calculations of optical nonlinear spectroscopic signals of arbitrary systems.

D. JILA MONSTR Calibration Procedures

The JILA Multdimensional Optical Nonlinear SpecTRometer (MONSTR) was developed as a versatile platform for conducting nonlinear optical spectroscopy[106]. A detailed summary is provided in the reference provided, but the key features together with practical advice for its routine operation will be discussed in this section. A single input beam is divided in 4 equal parts and exit the device in the traditional BOXCARs geometry. Pulse time delay is controlled with independent direct drive linear stages with 5 cm length X, Y, and Z and 20 cm for the U axis. These lengths translate into time ranges of 334 ps and 1.3 nanoseconds respectively. Active phase stabilization is carried out by monitoring error signals generated from a copropagating 532 nm cw laser. Interference patterns from the top, bottom, and inter decks result from retroreflection of the cw light off the output dichroic mirror and are routed on a unique path to independent silicon photodetectors. Error signals are sent through loop filters driving a piezo-mounted mirror within each respective beam path. Subcycle phase corrections are conducted *in situ* by locking to an established baseline.

Internal Alignment

Internal MONSTR alignment was carried out as suggested by Bristow *et al.* in the original report[106]. A cw laser was used at low intensity as an alignment reference. For initial alignment, the top and bottom halves were first aligned separately using the prearranged apertures ensuring no beam drift for the entire range of stage movement. As an aside, it was discovered that this point stability worsened when the stages were physically bolted to the aluminum case. As such, the U stage was unbolted and wedged along its aligned pins using a thin rubber gasket. This is critical since $\mathbf{k_3}$ was typically scanned through its entire delay range and most susceptible to alignment drift. These pieces were then assembled and a minor tweak was typically necessary to account for slight horizontal offset between the top and bottom decks. This was adjustment was made with a small change of the input periscope. Upon assembly and ensuring point stability, the output beams were propagated a large distance (several meters) to examine their parallelism and proximity. Minor adjustments to the final mirror along each beam path were made to achieve the necessary 1" box pattern.

The beam overlap at the sample position was tested two different ways. In one method, the beams were aligned through a μm 50 pinhole and small tweaks were made to the output mirrors if necessary. Alternatively, a surface backreflection off an uncoated flat 1" diameter fused silica window placed perpendicular across the converging beams. This reflection was focused into a 40x microscope objective (Edmund NT43-908), collimated, and imaged with a CMOS

camera (Mightex S series). This represents a replica of the focal plane at the sample position and served as a convenient aid for monitoring beam overlap.

Daily Input Alignment

The input femtosecond light is aligned through two apertures set to the predetermined alignment path prior to the MONSTR input. It was found that routine alignment to these references with external steering mirrors yielded reproducible beam overlap at the sample position. This was verified by testing the overlap through a 50 μm pinhole. A typical beam overlap measured at the replica focus position is illustrated in Figure A1.

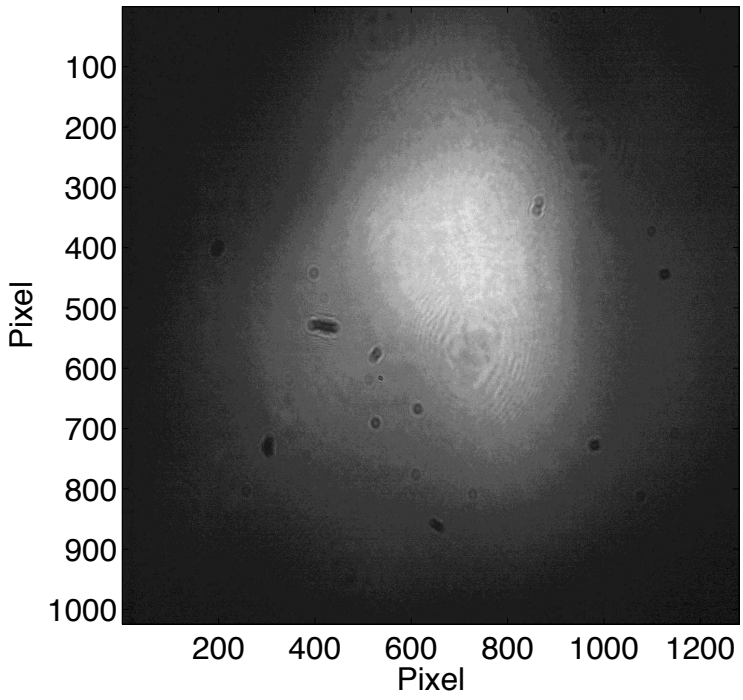

Figure A1. Overlap of XYU beams at the replica focus position.

Pulse Time Zero Calibration

Pulse timing at the sample position was typically established in two steps. First, a rough search for time zero positions was conducted by monitoring the field

correlations on the replica focus image described above. These scans were performed and analyzed with the "pulse overlap webcam Mightex.vi" program. Upon measuring the approximate relative temporal position of all pulses, a more precise measurement was made at the sample position. For this calibration, three excitation beams (X, Y, U) irradiated a sample of benzene generating a nonresonant FWM signal in the $\mathbf{k_1}$-$\mathbf{k_2}$+$\mathbf{k_3}$ direction. Benzene was chosen given its high nonlinear susceptibility and it was found to exhibit no interfering resonant or nonresonant solvation response. Iterative scans of a single beam were performed (TG-FROG.vi) with subsequent timing adjustments based on the fitted peak of the FWM signal integrated along detection frequency. Representative FROG traces and fits are presented below in Figure A2.

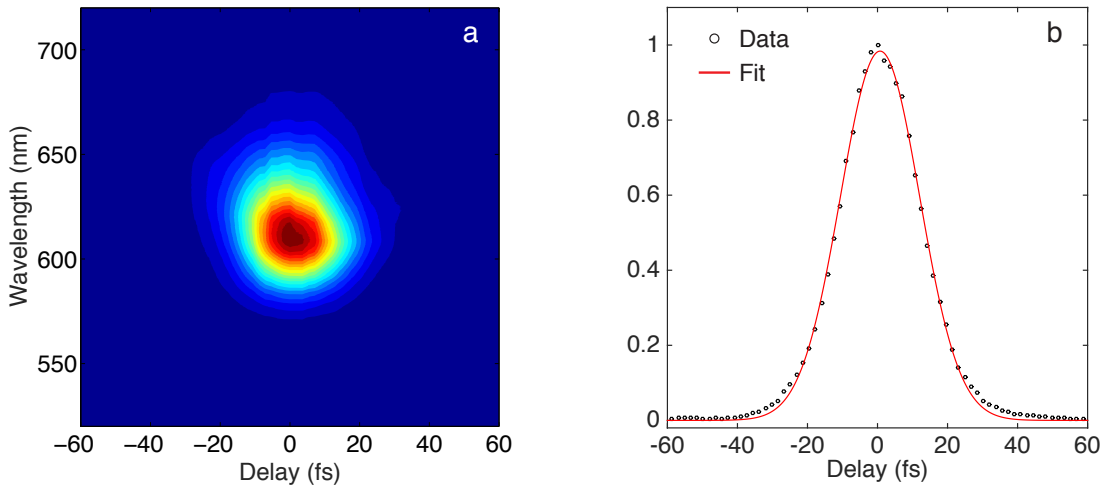

Figure A2. Representative (a) TG FROG spectrum and (b) fitted intensity autocorrelation used to calibrate timing of the excitation pulses.

An alternative timing procedure could be conducted using the pairwise field correlations at the replica focus position. Images were collected as a function of delay, binned, and saved (pulse overlap webcam Mightex.vi). The integrated

intensity provides a means of rough autocorrelation as well as relative timing of the excitation pulses.

Timing of the local oscillator reference beam (Z) was complicated for a couple reasons. First, attenuation with a neutral density filter was necessary to obtain an I_{LO}:I_{FWM} ratio of ~4:1. This intensity difference made for difficult detection at the replica focus position. As such, its timing was established by autocorrelation at the sample position. This was executed with either a two-photon photodiode (SiC) or second harmonic generation (BBO). Given the LO delay is, in principle, arbitrary for this experimentation, these methods were found to produce reasonably accurate results.

Phase Stabilization Scheme

Active phase stabilization is carried out by monitoring error signals generated from a copropagating 532 nm cw laser. Interference patterns from the top, bottom, and inter decks result from retroreflection of the cw light off the output dichroic mirror and are routed on a unique path to independent silicon photodetectors. Error signals are sent through loop filters driving a piezo-mounted mirror within each respective beam path. Subcycle phase corrections are conducted *in situ* by locking to a preestablished DC baseline.

E. Spectrally Resolved Signal Detection and CCD Calibration Procedures

Detection Scheme

The spectrally resolved detection scheme can be summarized as follows. The nonlinear signal field was coupled through free space into a spectrometer for

detection (Princeton Acton SpectraPro 2300i). In short, a 10 cm focal length PCX lens focused the light onto the entry slit. It was then dispersed with a 300 grv/mm diffraction grating blazed for 600 nm, collimated, and the first order component focused onto a liquid N_2-cooled 1024 x 256 pixel silicon CCD camera (Roper Scientific). For initial alignment, the axial position and rotation of the camera was adjusted to ensure the active element fell in the correct focal plane with the proper orientation.

CCD Calibration Procedure

Wavelength calibration of the CCD camera was carried out using the characteristic emission lines of a mercury-argon lamp (Oriel) together with the known output of our 532 nm reference laser (Coherent Verdi). For a typical measurement, lamp output was aligned into the spectrometer to produce sufficient signal above the dark count. Several emission lines were usually visible and no fewer than 4 spanning the spectral region of interest were fit versus pixel position assuming linear dependence. A small residual of the 532 nm reference laser is transmitted through the output dichroic of the JILA MONSTR. The local oscillator beam was aligned to the spectrometer and served as a secondary reference used for calibration.

F. Additional Experimental Considerations

Resolution of the Stimulated Emission Band

Acquisition of high quality SRTG data and subsequent interpretation of solvation dynamics requires simultaneous resolution of the Ground State Bleach (GSB) and Stimulated Emission (SE) responses within a finite excitation bandwidth

window. For fluorescent proteins, only species with a large Stokes shift (>50 nm) exhibited these two components without ambiguity, but is complicated by the presence of an overlapping Excited State Absorption (ESA) band. The steady state absorption and emission spectra of mPlum is overlaid with its SRTG response in Figure A3 below.

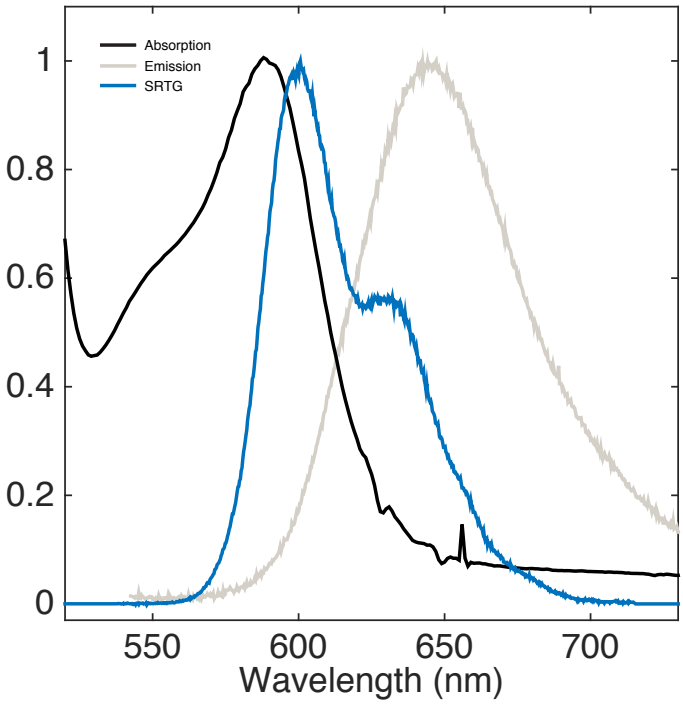

Figure A3. mPlum linear absorption and emission spectra overlaid with its SRTG response.

Another consideration to this end is the center position and width of the excitation source. Figure A4 presents SRTG spectra for mPlum E16Q under varying excitation conditions. It is clear that extraction of the excited state solvation dynamics is easiest with the reddest excitation, which provides clearest differentiation of the GSB and SE contributions. On the other hand, given a finite excitation bandwidth, we risk sacrificing resolving dynamics of subensembles at the

blue edge of our laser spectrum in cases of large inhomogeneous broadening. For these experiments, we assume roughly constant disorder among all point mutants given the minor structural perturbation and insensitivity of absorption spectrum width.

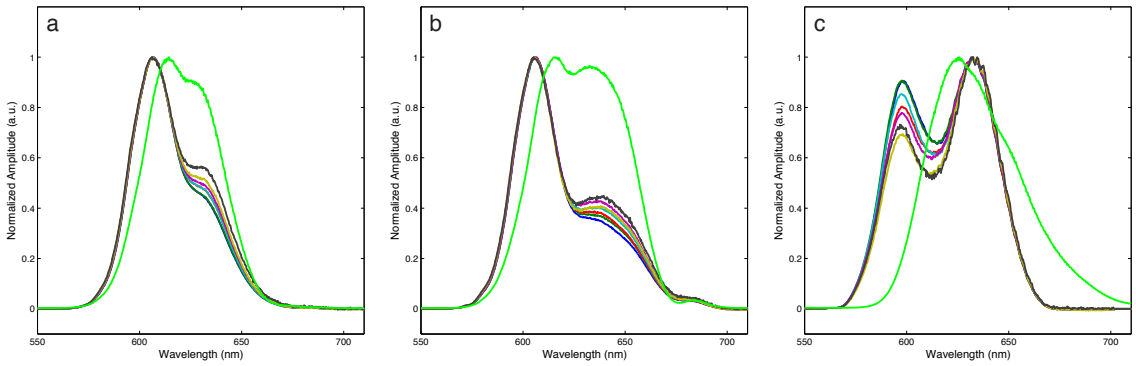

Figure A4. Excitation dependence of the SRTG response of mPlum E16Q.

Experimental Temporal Resolution

The length of excitation pulse and excited state lifetime of our excited probe dictate temporal resolution of SRTG data. For RFPs, lifetimes range from ~1-3 ns enabling adequate spectral range to resolve the range of intramolecular vibrations, solvent motion, and sidechain reorganization. However, this resolution is limited in both temporal extremes. Concerning fast timescales, experimental precision is limited by the excitation pulse duration (~20 fs) in principle. Examination of data at early delay reveals evidence of pulse overlap effects extending to ~150 fs largely due to imperfect compression. This slightly inhibits resolution of the fastest dynamics. Typical pulse overlap distortions at early delay are illustrated in Figure A5. In the case of mPlum, the interesting dynamics fall in the picosecond range and their measurement is uncompromised by these spectral artifacts. Conversely,

quantification of dynamics on long timescales is limited by the delay stage length (1.3 ns) and relaxation of excited state population. For variants with short lifetimes (~1 ns), signal intensity begins to approach background scatter and steady state fluorescence around 700 ps for a typical sample.

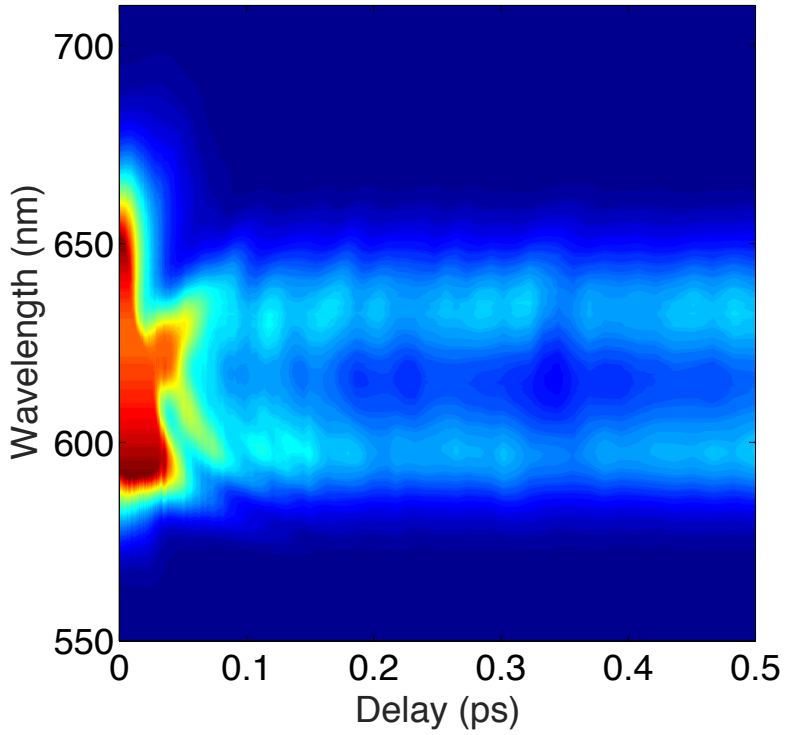

Figure A5. SRTG data for mPlum at early population time. Pulse overlap effects are evident within the first ~150 fs in most samples.

Detection

The nonlinear signal field can be detected using a homodyne or heterodyne scheme within the JILA MONSTR experimental platform. The latter provides a means of eliminating contributions from excitation scatter and steady state emission, however, it was observed that the spectral envelope of the signal was extremely sensitive to spectral filtering as demonstrated in Figure A6. For this reason, all reported SRTG data was collected utilizing a homodyne detection scheme.

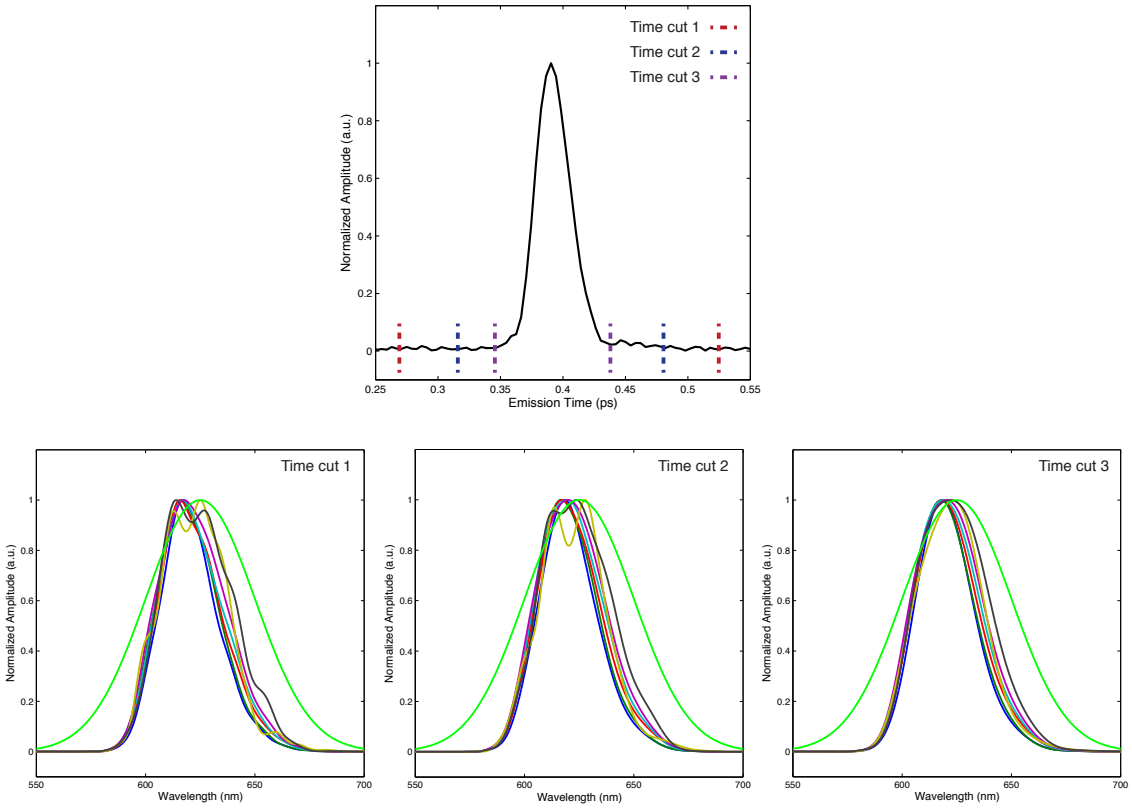

Figure A6. Examples of heterodyne-detected SRTG data of mPlum with various temporal filters. Varying the temporal window yields interference within the spectral envelope that complicates extraction of excited state dynamics.

Survey of other RFPs

The results of mPlum, presented in Chapter III, motivated a survey of the solvation dynamics across the mFruit family and related RFPs. A representative collection of data for several species is presented in Figure A7. It was discovered that quantification dynamics in these species was difficult for a few reasons. The primary obstacle to measurement of excited state solvation was lack of an obvious SE band in most cases. Resolution of this response might be due to either inadequate Stokes shift or presence of an overlapping ESA band as observed in transient absorption measurements. Given that the GSB component also shows little movement over the experimental time window, it is likely that chromophore

environment is rigid in these species compared to mPlum and their Stokes shift may originate in some other way. This further implicates the importance of the N-acylimine carbonyl-position 41 sidechain interaction as a primary mechanism of Stokes shift in red fluorescent proteins.

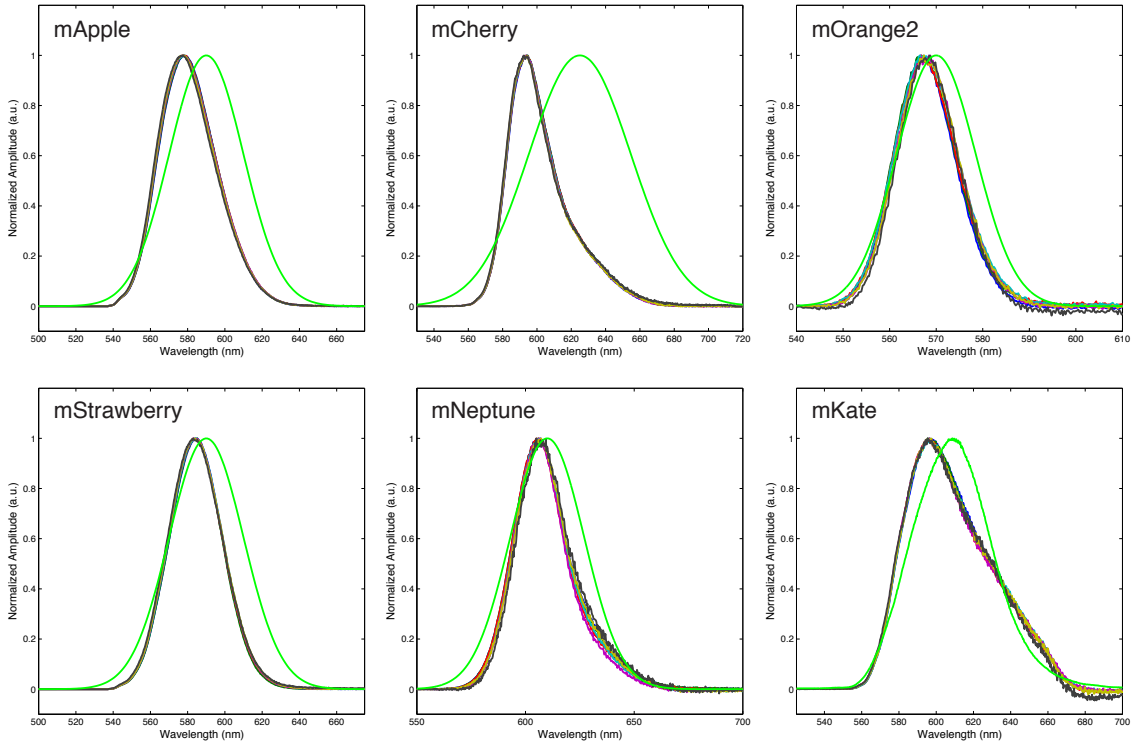

Figure A7. SRTG survey of several RFPs.